

5-2018

Hydration Shell Water Structure and Aggregation of Small Amphiphilic Solutes

Shannon R. Pattenaude
Purdue University

Follow this and additional works at: https://docs.lib.purdue.edu/open_access_dissertations

Recommended Citation

Pattenaude, Shannon R., "Hydration Shell Water Structure and Aggregation of Small Amphiphilic Solutes" (2018). *Open Access Dissertations*. 1799.
https://docs.lib.purdue.edu/open_access_dissertations/1799

This document has been made available through Purdue e-Pubs, a service of the Purdue University Libraries. Please contact epubs@purdue.edu for additional information.

**HYDRATION SHELL WATER STRUCTURE AND AGGREGATION OF
SMALL AMPHIPHILIC SOLUTES**

by

Shannon R. Pattenaude

A Dissertation

Submitted to the Faculty of Purdue University

In Partial Fulfillment of the Requirements for the degree of

Doctor of Philosophy



Department of Chemistry

West Lafayette, Indiana

May 2018

**THE PURDUE UNIVERSITY GRADUATE SCHOOL
STATEMENT OF COMMITTEE APPROVAL**

Dr. Dor Ben-Amotz, Chair

Department of Chemistry

Dr. Adam Wasserman

Department of Chemistry

Dr. Chittaranjan Das

Department of Chemistry

Dr. Suzanne Bart

Department of Chemistry

Approved by:

Dr. Christine Hrycyna

Head of the Graduate Program

To God, my husband Scott, father Herbert and mother Elaine, and eight siblings Jonathan, Sara, Dyan, Joshua, Jacob, Desa, Dana, and Jaisun, all of whom I love dearly.

ACKNOWLEDGMENTS

I would first like to acknowledge God for all His great blessings and grace. “With God all things are possible” - Matthew 19:26. I would also like to acknowledge my steadfast, supportive, and loving husband Scott. We have shared and endured this process together, and I am both thankful to and proud of him. I look forward to our next adventure together. I thank my family including in-laws and my siblings with their spouses and children for the continued support and misplaced awe of my intelligence and work.

I especially thank my graduate advisor Professor Dor Ben-Amotz for always creating scientific inspiration through his enthusiasm and setting a fantastic role model as a researcher, writer, supervisor, and teacher. In addition, I would like to acknowledge Professors Adam Wasserman, Chittaranjan Das, and Suzanne Bart for serving on my committee and providing attention, comments, queries, and answers throughout my graduate career.

I would also like to acknowledge the Ben-Amotz group: Dr. Blake Rankin for his never-ending patience and guidance, Dr. Owen Rehrauer for his role as my mentor, Dr. Sam Zukowski for his advice and support, and Dr. Josh Long and Dr. Sarah Matt for supporting me in my last year and for always being available to chat. Additionally, I would like to thank Dr. Bharat Mankani, Colby Raymond, Louis Streacker, Patrick Wise, and Aria Brecht for useful discussions and support.

Additionally, I would like to acknowledge the Chemistry Department staff including Betty H., Debbie P., and Lynn R. in the Main Office; Chris H., Stephen H., and Steve S. in Administration; Paul B. in Safety; Liz H. for guiding dissertation formatting and as Dor’s secretary; Beth C. and Tricia H. in the Business Office; Darci D. and Suzy G. in Procurement; Betty D. and Ned G. in the Chemistry Shop; Beatriz C. in the Resource Room; Marybeth M., Melissa R., and Susan L. in the General Chemistry Office; Jeanne M. in the Prep Lab; and Konrad K. in the Amy Facility. I would also like to thank all the custodians and anybody else that keeps the Chemistry Department running smoothly. Finally, I would like to acknowledge the National Science Foundation for financially supporting this research.

TABLE OF CONTENTS

LIST OF TABLES	viii
LIST OF FIGURES	ix
LIST OF ABBREVIATIONS AND SYMBOLS	xii
ABSTRACT.....	xiv
CHAPTER 1. RAMAN SPECTROSCOPY, INSTRUMENTATION, AND ANALYSIS.....	1
1.1 Raman Spectroscopy.....	1
1.2 514.5 nm Ar-Ion Laser Raman Instrument.....	2
1.3 Raman-MCR: Hydration Shell Spectroscopy.....	3
1.3.1 Hydration Shell Spectroscopy with Head-group or Counterion Subtraction	5
CHAPTER 2. WATER-MEDIATED AGGREGATION OF 2-BUTOXYETHANOL	6
2.1 Abstract.....	6
2.2 Introduction.....	6
2.3 Methods.....	9
2.3.1 Experimental.....	9
2.3.2 Random Mixing.....	9
2.3.3 Molecular Dynamics Simulations.....	10
2.4 Results and Discussion	11
2.4.1 Raman-MCR Hydration-Shell Spectroscopy	11
2.4.2 Quantification of Hydrophobic Contacts.....	14
2.4.3 Water-mediated Interaction Energy.....	17
2.5 Conclusions.....	19
2.6 Supplementary Information	20
2.6.1 Density-Based Unit Conversions.....	20
2.6.2 CH Peak Frequency Shifts for BE.....	21
2.6.3 Finite Lattice Predictions.....	22
2.6.4 MD Simulation Procedures.....	22
CHAPTER 3. HYDROPHOBIC HYDRATION SHELL WATER STRUCTURE.....	24
3.1 Abstract.....	24
3.2 Introduction.....	24

3.3	Methods.....	26
3.4	Results and Discussion	27
3.5	Conclusions.....	32
3.6	Supplementary Information	33
CHAPTER 4. HYDRATION AND INTERACTION OF IONIC COMPOUNDS		36
4.1	Abstract.....	36
4.2	Introduction.....	36
4.3	Methods.....	37
4.4	Results and Discussion	37
4.4.1	Sodium Halide Solutions	37
4.4.2	Alkali Metal Chloride Solutions.....	38
4.5	Conclusions.....	39
CHAPTER 5. HYDROPHILIC INTERACTIONS: POLARITY EFFECTS ON HYDRATION		41
5.1	Abstract.....	41
5.2	Introduction.....	41
5.3	Methods.....	42
5.3.1	Experimental.....	42
5.3.2	MD Simulations.....	42
5.4	Results and Discussion	42
5.5	Conclusions.....	48
CHAPTER 6. CHARGE EFFECTS ON HYDRATION AND AGGREGATION		49
6.1	Introduction.....	49
6.2	Methods.....	49
6.3	Results and Discussion	50
6.4	Conclusions.....	54
CHAPTER 7. INTRAMOLECULAR DEPENDENT HYDRATION SHELL SPECTRA OF BENZENEDIOLS.....		55
7.1	Abstract.....	55
7.2	Introduction.....	55
7.3	Methods.....	56

7.4 Results and Discussion	56
7.5 Conclusions.....	59
APPENDIX A. ADDITIONAL 2-BUTOXYETHANOL DATA	60
APPENDIX B. ALKALI METAL HALIDE SPECTRA	64
REFERENCES	70
VITA.....	76
PUBLICATION.....	77

LIST OF TABLES

Table 3.1 Peak positions of the low and high frequency features and frequency shift of each with respect to the peak position in the TBA hydration shell.....	32
---	----

LIST OF FIGURES

- Figure 1.1 Jablonski diagram illustrating Rayleigh, Stokes Raman, and anti-Stokes Raman scattering phenomena..... 1
- Figure 1.2 Typical raw Raman spectra of (A) neon (0.05 sec exposure time, 1 image, 300 accumulations) and (B) pure water at 20°C (0.4 sec exposure time, 1 image, 750 accumulations). The six neon peaks fitted for wavenumber calibration are indicated with black arrows. The HOH bend and OH stretch of water are indicated along with the helium peaks used to correct for frequency shifts. 3
- Figure 1.3 Illustration of Raman-MCR analysis where the solution spectrum contains 2-butoxyethanol (BE), the solvent spectrum is pure water, and the solute-correlated spectrum contains features from BE and any water that is perturbed by the BE..... 4
- Figure 1.4 Top: Molecular structures of TMAc and NaHCOOH. Bottom: Pure water and 1.0 M NaHCOOH solutions shown with SC spectra for 1.0 M NaHCOOH and 1.0 M TMAc with water as the reference and for 1.0 M TMAc with 1.0 M NaHCOOH as the reference..... 5
- Figure 2.1 (A) Raman spectra (normalized to unit area) of pure H₂O (dotted black) and aqueous BE solutions of different concentration (0.19, 0.29, 0.38, 0.46, 0.55, 0.64, 0.80, 0.94, 1.1, 1.3, 1.6, 1.9, 2.2, 2.4, and 2.7 M). (B) Minimum area SC spectra of BE obtained from the spectra shown in (A), each normalized to the same total CH band area (only the high frequency edge of the CH band is shown in (B)). 12
- Figure 2.2 Raman-MCR hydration shell depletion percentage for aqueous methanol (MeOH, red points), TBA (green points), and BE obtained either experimentally (solid blue points) or from CHARMM-AA/TIP3P MD simulations¹¹ (open blue points), plotted as a function of solute molarity (A) or volume fraction p (B). The black curves are WRM predictions obtained assuming several different solute-solute contact energies, where $\beta\epsilon = 0$ pertains to an idealized random mixture. 13
- Figure 2.3 (A) Monomer (blue) and aggregate (red) component spectra obtained from the second round of SMCR applied to the SC solution spectra in Figure 2.1B (A, inset) Relationship between non-contacting CH fraction f_{CH} and total BE concentration from Raman-MCR experiments (solid points), MD simulations (open points), and RM predictions (dashed regions). (B) Monomer concentrations and (C) aggregation concentrations obtained from Raman-MCR experiments (using the MD correlation between f_{CH} and the f_M , shown in Figure 2.4), MD simulations, and RM predictions for BE. The black dashed line corresponds to the total solute concentration..... 15
- Figure 2.4 Correlation between the number of non-aggregated monomer BE molecules and the number of non-contacting CH groups, obtained from MD simulations. The solid curve is a power-law fit. The inset image illustrates the relationship between f_{CH} and f_M for a particular configuration of four BE molecules, for which $f_{CH} = 44/52 = 0.85$ and $f_M = 2/4 = 0.5$ 16

Figure 2.5 Total potentials of mean force (solid black) between BE molecules are compared with the corresponding direct (dashed red) and water-mediated (solid blue) contributions calculated using two different force fields: (A) CHARMM-AA/TIP3P and (B) TraPPE/TIP4P-2005 with HH-alkane modifications. ³⁶	18
Figure 2.6 BE molality and molarity measured values (solid points) fit by a fourth-order polynomial (solid curve), $M = 0.97625m - 0.094847m^2 + 0.0043131m^4$	20
Figure 2.7 (A) SC spectra of aqueous BE solutions (0.1 M – 2.7 M) showing the CH peak region ($2500\text{ cm}^{-1} - 3050\text{ cm}^{-1}$) with the symmetric ($\nu_{\text{sym}} \sim 2880\text{ cm}^{-1}$, down triangles) and asymmetric ($\nu_{\text{asy}} \sim 2935\text{ cm}^{-1}$, up triangles) stretching modes shown in the inset panel. (B) The change in Raman shift frequency for each of the modes ($\Delta\nu_{\text{CH}}$) from their corresponding peak frequency determined at $[\text{BE}] = 0.1\text{ M}$	21
Figure 3.1 Aqueous THF phase diagram previously reported by Takasu et al. ⁵⁵	25
Figure 3.2 Hydration shell Raman-MCR spectra for (A) <i>d9</i> -TBA at low (2°C) and high (100°C) temperature (collected by Dr. Blake Rankin) and (B) THF at low (2°C) and high (40°C) temperature. Black dashed lines correspond to 177.85 cm^{-1} and 3229.7 cm^{-1}	28
Figure 3.3 Correlation between the low and high frequency peak intensities for methanol (MeOH), tetramethylammonium (TMeA), ethanol (EtOH), tetraethylammonium (TEtA), n-propanol (PrOH), TBA, trimethylamine N-oxide (TMAO), THF, and low temperature component derived from MCR analysis of pure water (see Figure 3.4).....	29
Figure 3.4 (A) Temperature dependent pure water raw Raman spectra. (B) Raman-MCR spectra (low temperature components) obtained from using the 100°C temperature spectrum (dashed red) as the reference. Black dashed lines correspond to 177.85 cm^{-1} and 3229.7 cm^{-1}	30
Figure 3.5 Correlation between the tetrahedral order parameter (q) of bulk water and the (A) low and (B) high frequency peak intensities from Figure 3.4B.....	31
Figure 3.6 These are the Raman spectrum of (A) ice at -2°C and (B) THF clathrate hydrate ($2.5\text{ M} \sim 100\% \text{ CH}$) at 2°C	32
Figure 3.7 Raman SC spectra low frequency regions for nine small amphiphilic molecules. Column one, TBA, and TMAO data taken by Dr. Blake Rankin. Column two data taken by Dr. Joel Davis.....	33
Figure 3.8 Raman SC spectra high frequency regions for nine small amphiphilic molecules.	34
Figure 3.9 Hydration shell spectra of (A) 0.5 M and 1 M THF taken at 0°C and (B) 1 M and 4 M TBA taken at 2°C . TBA data collected by Dr. Blake Rankin.	35
Figure 4.1 Hydration shell depletion of aqueous sodium halide salts as a function of salt concentration. The hydration shell depletion values are calculated with respect to the OH area calculation for the $\sim 0.1\text{ M}$ SC spectra for each species.	38
Figure 4.2 (A) Hydration shell depletion of aqueous alkali metal chloride salts as a function of salt concentration. The depletion values are calculated with respect to the OH area for the $\sim 0.1\text{ M}$ SC spectra for each species. (B) Change in the OH Raman shift with respect to the OH Raman shift observed for the $\sim 0.1\text{ M}$ SC spectra for each salt.	39

- Figure 5.1 (A) Raw Raman spectra of acetonitrile solutions and pure water (dashed blue). (B) SMCR SC background-subtracted component of acetonitrile solutions. (C) CN stretching region of (B). 43
- Figure 5.2 Acetonitrile (A) spectrum with CN stretch (left inset), CH stretch (right inset), and OH stretch. (B) CN and CH stretch change in frequency with respect to acetonitrile concentration (C) Hydration-shell dependence on acetonitrile concentration normalized per CH group. (C) Change in the OH area (ΔA_{OH}) of the hydration-shell with respect to acetonitrile concentration. 45
- Figure 5.3 DMSO (A) spectrum of CH stretch and OH stretch. Insets are the low (left) and high (right) frequency CH stretch peaks. (B) Low and high frequency CH stretch frequency shifts with respect to DMSO concentration. (C) Hydration shell per CH of DMSO. (D) Depletion percentage of the hydration shell with respect to DMSO concentration. 46
- Figure 5.4 (A) Acetonitrile-acetonitrile radial distribution functions shown for the gas phase (red) and solution phase (black). Shaded region indicates error. (B) PMF between acetonitrile molecules in the gas phase, solution phase, and water-mediated contribution to the total solution phase interaction. 47
- Figure 5.5 Hydration-shell temperature dependence for 1.0 M acetonitrile solution. Pure water (dashed) temperature dependence shown for reference. 48
- Figure 6.1 Raman spectra for (A) aqueous *tert*-butanol and water, (B) aqueous sodium trimethylacetate, aqueous sodium formate, and water; (C) aqueous *tert*-butylammonium chloride, aqueous ammonium chloride, and water. The right-side panel shows the structure of the solute and the structure of the head-group used in equimolar amounts for the SMCR reference solution. 51
- Figure 6.2 Hydration shell spectra for (A) TBA, (B) TMA_t, and (C) TBAm. For (A), (B), and (C) the dashed blue spectrum is pure water. (D) Hydration shell depletion percentage for TBA, TMA_t, and TBAm. Dashed lines are linear fits to the data. Frequency shifts with respect to concentration for the (E) low ($\sim 2930 \text{ cm}^{-1}$) and (F) high ($\sim 2980 \text{ cm}^{-1}$) frequency prominent CH-stretch modes. Black dashed lines are linear fits to the data. Red and blue dashed lines are fourth-order polynomial fits to the data. 53
- Figure 6.3 Hydration shell spectra OH stretch region for dilute (0.2 M) TBA, TMA_t, and TBAm. 54
- Figure 7.1 Raman spectra for water, benzene, phenol, hydroquinone, resorcinol, and catechol. 57
- Figure 7.2 Hydration shell spectra normalized to CH stretch intensity for (A) benzene, (B) phenol, (C) hydroquinone, (D) resorcinol, and (E) catechol. 58
- Figure 7.3 Hydration shell spectra for equimolar solutions of phenol, hydroquinone, resorcinol, and catechol. Benzene at 0.2 M is also shown. Spectra are normalized per solute. 59

LIST OF ABBREVIATIONS AND SYMBOLS

β	$1/RT$
$\beta\varepsilon$	Solute-solute contact energy
BE	2-butoxyethanol (C ₆ H ₁₄ O ₂)
χ	Mole fraction
$d\%$	Hydration shell depletion percentage
EB	1-ethoxybutane (C ₆ H ₁₄ O)
fs-IR	Femtosecond infrared
FL	Finite lattice
f_{CH}	Fraction of non-contacting CH groups
f_{M}	Fraction of monomers
$g(r)$	Radial distribution function
I	Intensity
$\langle k \rangle$	Average number of molecular contacts
k_B	Boltzmann constant = $1.381 \times 10^{-23} \text{ J} \cdot \text{K}^{-1}$
λ	Wavelength (nm)
LCW	Lum-Chandler-Weeks theory
m	Molality (mol solute/kg solution)
M	Molarity (mol solute/L solution)
MCR	Multivariate curve resolution
MD	Molecular dynamics
n	Number of molecules
N	Number of lattice sites or coordination number
ν	Raman shift or frequency (cm ⁻¹)
p	Volume fraction
PMF	Potential of mean force
r	Radius
R	Molar gas constant = $8.314 \text{ J} \cdot \text{K}^{-1} \cdot \text{mol}^{-1}$
RM	Random mixing
ρ	Density (mg/mL)

<i>RT</i>	Thermal energy at 298 K = 2.5 kJ·mol ⁻¹
SC	Solute-correlated
SMCR	Self-modeling curve resolution
TBA	<i>tert</i> -butyl alcohol (C ₄ H ₁₀ O)
THF	Tetrahydrofuran (C ₄ H ₈ O)
<i>wt%</i>	Mass (weight) percent
WRM	Weighted random mixing

ABSTRACT

Author: Pattenaude, Shannon, R. PhD

Institution: Purdue University

Degree Received: May 2018

Title: Hydration Shell Water Structure and Aggregation of Small Amphiphilic Solutes

Committee Chair: Dor Ben-Amotz

My research aims to address long-standing questions in physical chemistry about water-mediated hydrophobic and ionic interactions of biological relevance. For example, my research has provided some of the first experimental evidence of water driving hydrophobic groups apart rather than pushing them together in solution, thus damping rather than enhancing the contact free energy of oily molecules in water. I have also obtained some of the first experimental evidence concerning the structure of water structure around nonpolar groups in solution, thus demonstrating that hydrophobic hydration-shells have a clathrate hydrate-like structure. In addition, I am currently studying ionic interactions in water, which are important due to the ubiquity of solvated ions in living systems, along with three additional projects investigating solute polarity, charge, and substituent placement effects on solute aggregation and water structure. Finally, I have contributed to one project that probes aggregation of hydrophobic solutes in binary alcohol/water mixtures and to another, highly collaborative project that addresses the continued debate regarding the structure of hydrated protons in liquid water.

Here, the combined application of Raman spectroscopy and multivariate curve resolution (Raman-MCR) to aqueous solutions has been used to reveal solute-correlated (SC) spectra, which contain vibrational spectral features arising from the hydration shell around a dissolved solute, as well as the solute itself. Such spectra are used to obtain information about changes in water structure, as a function of solute identity, size, shape, polarity, and charge. Moreover, Raman-MCR is used to probe water-mediated interactions between solute molecules, by detecting interaction-induced changes in the SC spectra of variable solution concentrations.

CHAPTER 1. RAMAN SPECTROSCOPY, INSTRUMENTATION, AND ANALYSIS

1.1 Raman Spectroscopy

Raman spectroscopy is the primary analytical tool used in the following research. Raman scattering is an inelastic light scattering in which an incident photon excites the vibrational and rotational modes of the sample and after relaxation of these modes light is scattered with a different amount of energy than before it interacted with the sample. Stokes Raman scattering occurs if the scattered photon energy is less than the incident photon energy; whereas, anti-Stokes Raman scattering occurs if the scattered photon energy is more than the incident photon energy and Rayleigh scattering occurs if the scattered photon has the same energy as the incident photon. In this work, only Stokes Raman scattering is collected.

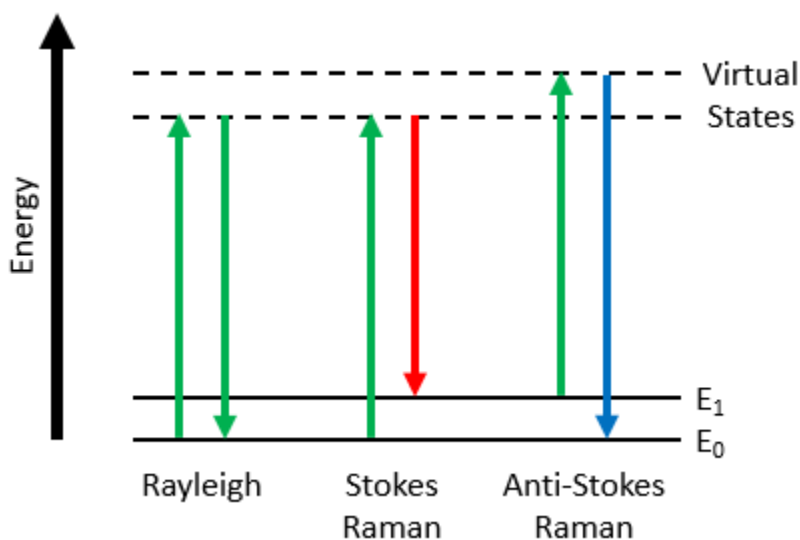


Figure 1.1 Jablonski diagram illustrating Rayleigh, Stokes Raman, and anti-Stokes Raman scattering phenomena.

The intensity of the scattered Raman light depends on the polarizability of the electrons in the sample. Raman spectroscopy is complementary to infrared spectroscopy in that infrared intensity depends on the net change in dipole of the vibrating or rotating sample molecules. Natural

Raman scattering is a very weak effect where only 1 in 10^6 incident photons are Raman scattered. Therefore, intense phenomena like fluorescence must be avoided as much as possible to observe the weak Raman effect. In addition, for the work reported here signal-to-noise ratios of more than 1000:1 are needed in order to perform reliable multivariate curve resolution analysis of the Raman spectra.

1.2 514.5 nm Ar-Ion Laser Raman Instrument

The set-up of the previously described home-built instrument includes a 514.5 nm argon-ion laser source directed through a combination of a monochromator, polarizer (optional), notch filter, mirrors, lenses, pinhole, and 20× long working distance microscope objective to the sample.¹⁻³ The scattered Raman signal is then collected along the same path as the incident laser light, and furthermore passed through a beam-splitter (optional), lens, pinhole, and fiber optic cable to an imaging spectrograph. The spectrograph grating used for these studies has 300 grooves/mm resulting in $\sim 6 \text{ cm}^{-1}$ /pixel resolution. Finally, the signal is recorded on a thermoelectrically cooled charge couple device (CCD) detector typically binned to 1340×1 . Our Raman set-up, especially the direct backscattered signal, fiber optic cable collection and CCD detection, allows for superior signal-to-noise of at least 1000:1 for traditional samples. Generally, the laser is operated at ~ 15 -25 mW before the objective. The sample holder accommodates up to six 1 cm cuvettes and is temperature controlled via a water bath for sample variability in the -10°C to 100°C range with 0.01°C accuracy.

A typical neon spectrum from a neon lamp, which is used daily as a standard for wavelength calibration, is shown in Figure 1.2. More specifically, six neon peaks are fitted with Gaussian functions and the pixel of maximum intensity for each of the six peaks are fitted to a cubic function of the CCD pixel position with respect to wavelength. These wavelengths are then converted to vibrational wavenumbers. In addition, a helium lamp is used when collecting spectra to correct for any frequency shifts due to changes in the barometric pressure throughout the day. In this manner, all spectra can be frequency shifted such that two helium peaks overlap to ensure that there are no arbitrary frequency shifts among spectra. Figure 1.2 shows a typical water spectrum at 20°C and highlights the two helium peaks used for frequency shift correction.

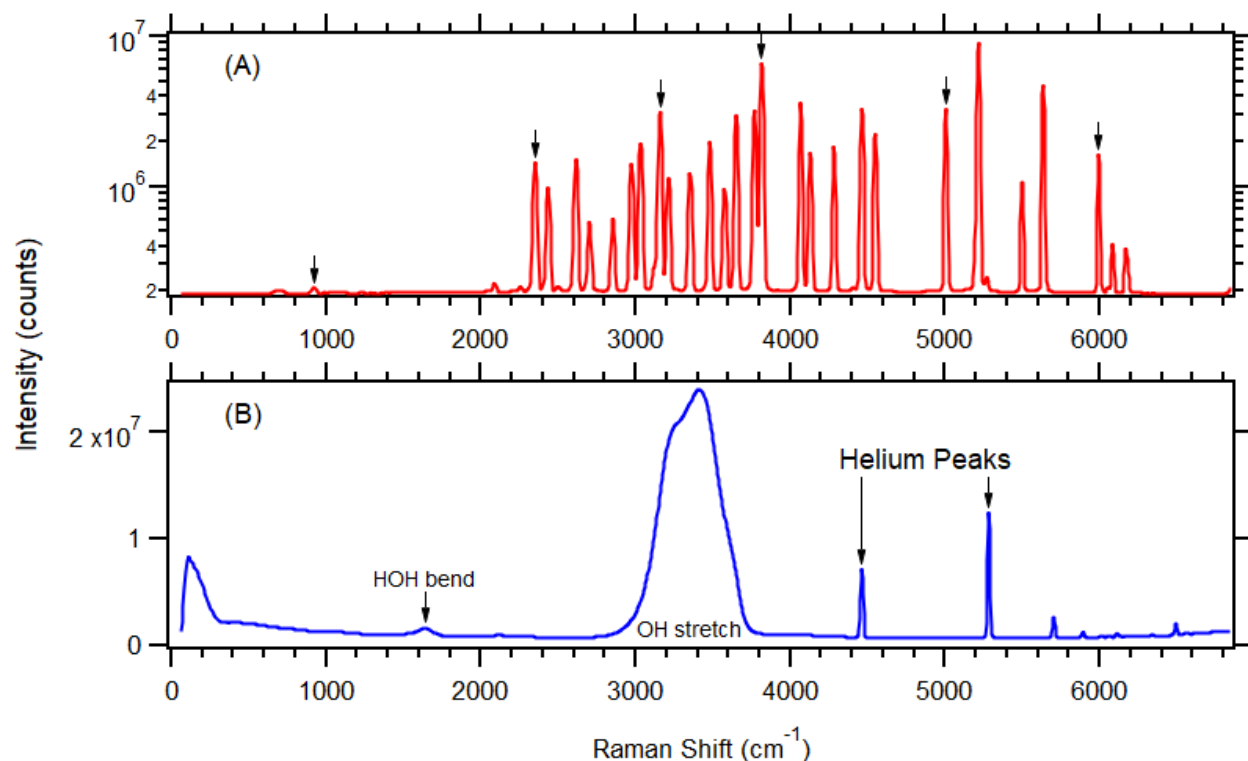


Figure 1.2 Typical raw Raman spectra of (A) neon (0.05 sec exposure time, 1 image, 300 accumulations) and (B) pure water at 20°C (0.4 sec exposure time, 1 image, 750 accumulations). The six neon peaks fitted for wavenumber calibration are indicated with black arrows. The HOH bend and OH stretch of water are indicated along with the helium peaks used to correct for frequency shifts.

1.3 Raman-MCR: Hydration Shell Spectroscopy

Contained within raw Raman spectra are very useful solute-correlated (SC) spectra commonly used in our group to observe otherwise hidden spectral information of aqueous solutions. The SC spectrum is obtained by using self-modeling curve resolution (SMCR) algorithms to essentially take the difference between the solution spectrum and the pure water spectrum at the same temperature yielding spectral features corresponding to any part of the solution that does not look like bulk water.⁴ For example, in the OH region of 3000-3800 cm^{-1} , the SC spectrum contains information about solute hydration shell water molecules that differ spectroscopically from bulk water molecules.

Self-modeling curve resolution (SMCR) is a type of multivariate curve resolution (MCR) that is applied to the raw Raman spectra collected for this research. SMCR decomposes a known

mixture spectrum into two components: a known solvent (reference) spectrum and a solute-correlated spectrum that includes everything else. Unlike direct subtraction of spectra, a solute-correlated spectrum is constrained by non-negativity in regions of the spectrum where the reference spectrum has intensity. In addition, the solute-correlated spectra here are minimum area spectra. Minimum area means that the solute-correlated intensity is zero in a region that the reference has intensity. This is achieved by removing as much of the reference spectrum from the mixture spectrum as possible without achieving negative intensity. The mixture spectrum is a linear combination of the reference and solute-correlated spectrum.

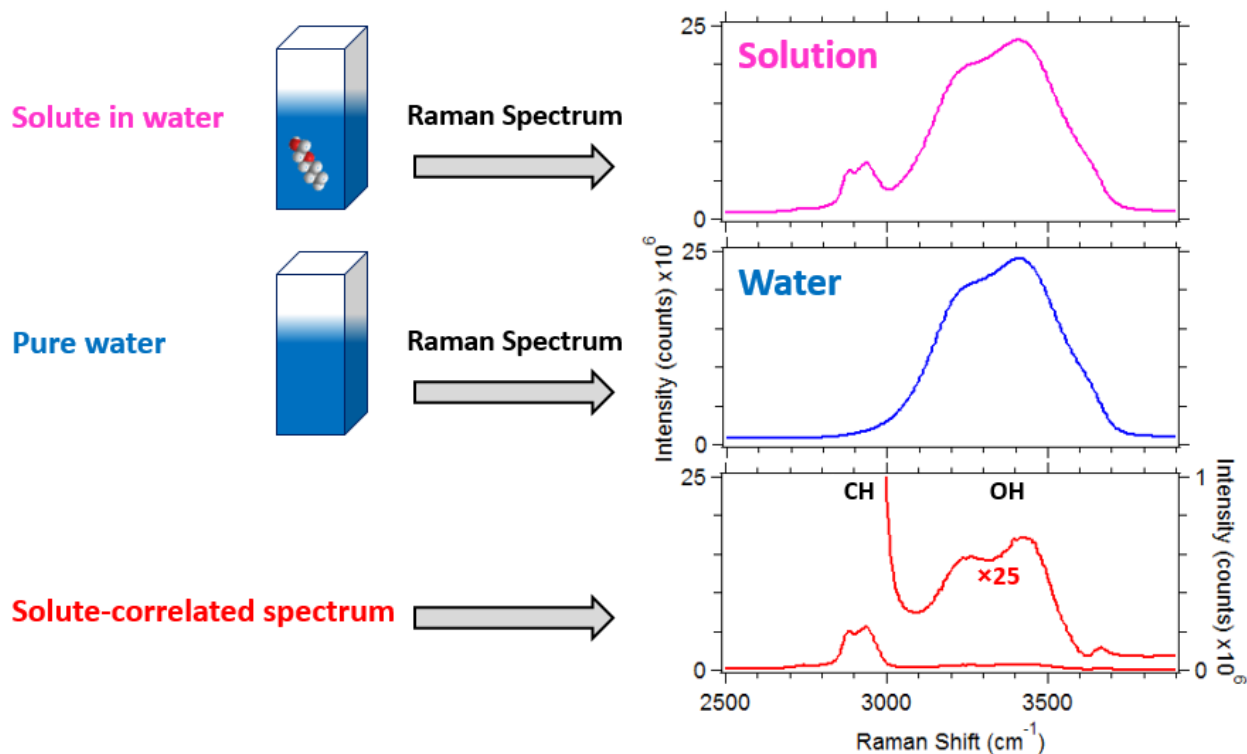


Figure 1.3 Illustration of Raman-MCR analysis where the solution spectrum contains 2-butoxyethanol (BE), the solvent spectrum is pure water, and the solute-correlated spectrum contains features from BE and any water that is perturbed by the BE.

1.3.1 Hydration Shell Spectroscopy with Head-group or Counterion Subtraction

Solutions of solute molecules with head-groups (e.g. ionic head-groups) or counterions that contribute significantly to the solute-correlated spectrum, but are not the focus of interest can be analyzed using Raman-MCR with head-group/counterion subtraction. In this method, instead of pure water as the reference spectrum, a spectrum of the head-group or counterion in solution is used as a reference. For example, solutions of sodium trimethylacetate (TMAc) can be analyzed using water as a reference or using an equimolar solution of sodium formate (NaHCOO). The NaHCOO head-group has a significant hydration shell spectrum as shown in Figure 1.4 by the gray spectrum. Therefore, to observe the hydration shell of the isobutyl group of TMAc shown in red in Figure 1.4, it is necessary to remove any contribution from its NaHCOO head-group.

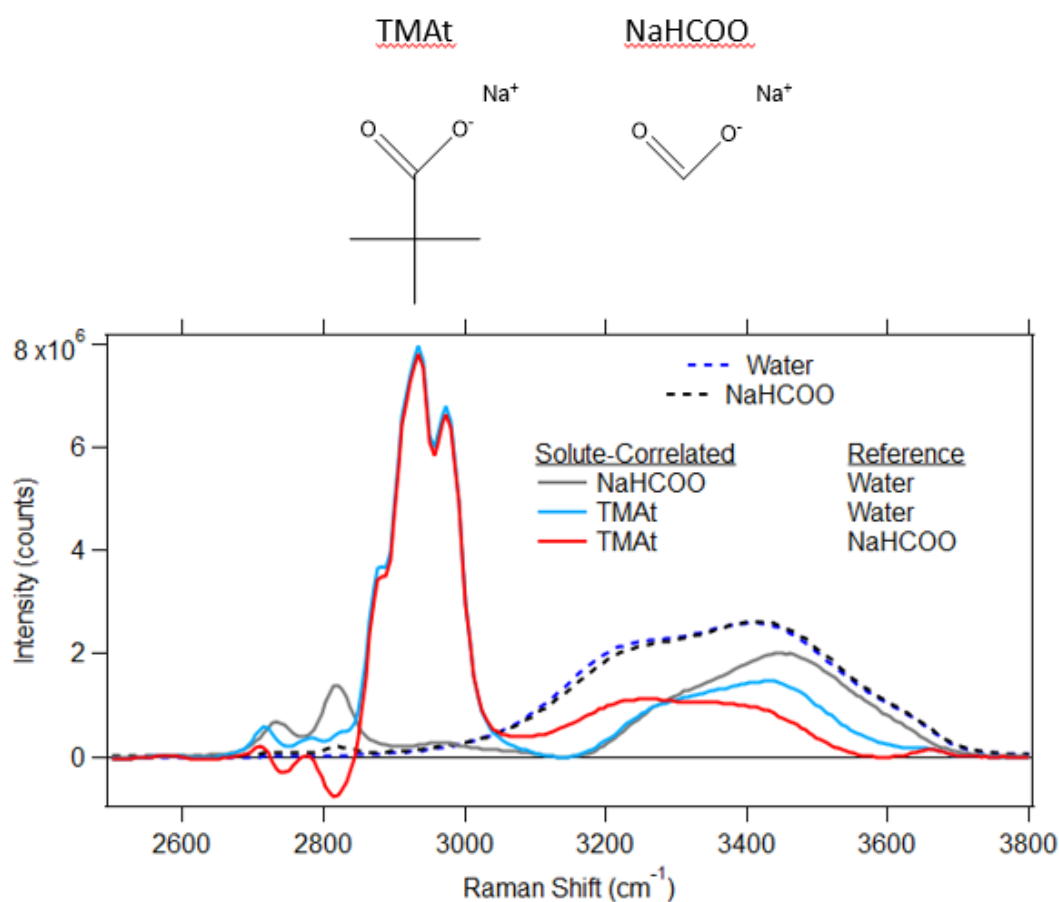


Figure 1.4 Top: Molecular structures of TMAc and NaHCOOH. Bottom: Pure water and 1.0 M NaHCOOH solutions shown with SC spectra for 1.0 M NaHCOOH and 1.0 M TMAc with water as the reference and for 1.0 M TMAc with 1.0 M NaHCOOH as the reference.

CHAPTER 2. WATER-MEDIATED AGGREGATION OF 2-BUTOXYETHANOL

Reproduced from S. R. Pattenaude, B. M. Rankin, K. Mochizuki and D. Ben-Amotz, *Phys. Chem. Chem. Phys.*, 2016, **18**, 24937 DOI:10.1039/C6CP04379H - Reproduced by permission of the PCCP Owner Societies

2.1 Abstract

Water plays an important role in mediating hydrophobic interactions, and yet open questions remain regarding the magnitude, and even the sign, of water-mediated contributions to the potential of mean force between a pair of oily molecules dissolved in water. Here, the water-mediated interaction between 2-butoxyethanol (BE) molecules dissolved in water is quantified using Raman multivariate curve resolution (Raman-MCR), molecular dynamics (MD) simulations, and random mixing (RM) predictions. Our results indicate that the number of contacts between BE molecules at concentrations between 0.2 M and 1 M exceeds RM predictions, but is less than some MD predictions. Moreover, the potential of mean force between BE molecules in water has a well depth that is shallower than the direct interaction between 1-ethoxybutane chains in the gas phase, and thus the water-mediated contribution to BE aggregation is repulsive, as it pulls BE molecules apart rather than pushing them together.

2.2 Introduction

Hydrophobic interactions are considered to play a key role in self-assembly processes ranging from micelle and membrane formation to protein folding and ligand binding.⁵⁻⁶ However, recent studies of aqueous solutions containing small alcohol molecules (ranging from methanol to butanol isomers) found that the number of hydrophobic contacts in such solutions is similar to that expected in a random mixture of non-interacting solute molecules,⁷ thus implying that hydrophobic interactions between small hydrophobic groups are too weak to compete with random thermal energy fluctuations (of magnitude $RT \sim 2.5 \text{ kJ mol}^{-1}$).⁷⁻⁹ Here, we investigate the aggregation of aqueous 2-butoxyethanol (BE, $n\text{-C}_4\text{H}_9\text{OC}_2\text{H}_4\text{OH}$)¹⁰⁻¹¹ in an effort to establish the solute size at which hydrophobic interactions begin to exceed thermal fluctuations. Our results reveal that the

magnitude of the BE contact free energy in water slightly exceeds RT , and thus is clearly more attractive than that for smaller alcohol solutes. However, our results also indicate that the contact free energy of BE is smaller (less attractive) than the direct van der Waals interaction energy between the corresponding oily tails, as modeled using the interaction of two isolated (gas phase) 1-ethoxybutane (EB) molecules. The latter results imply that the water-mediated hydrophobic interaction between BE molecules is repulsive, thus favoring solvent-separated over direct contact configurations.

The notion that hydrophobicity may be influenced by a solute size dependent crossover was first proposed by Kauzmann,⁶ who noted that while molecular hydrophobic hydration has a negative enthalpy and entropy (under ambient conditions), macroscopic oil-water interfacial tension implies that these thermodynamic signatures should change sign as solute size increases. The fact that purely repulsive (hard-sphere) hydrophobic solutes must undergo a size dependent crossover was first demonstrated by Stillinger,¹² and motivated the subsequent development of Lum-Chandler-Weeks (LCW) theory.¹³⁻¹⁴ Although numerous simulations,¹⁵⁻¹⁸ and some experiments,^{3, 19-21} have obtained evidence of a size dependent crossover,^{17, 22} some recent simulations²³ and experiments⁷ imply that solute attractive interactions can give rise to a competing crossover that weakens rather than strengthens hydrophobic interactions.⁸⁻⁹ In other words, while entropic depletion forces and the associated size dependent dewetting crossover give rise to strongly attractive water-mediated hydrophobic interactions, oil-water cohesive (van der Waals) interactions stabilize the hydrophobic hydration-shell around separated (non-contacting) oily molecules, and thus drive oily molecules apart. The present results confirm that BE is sufficiently large that its cohesive attraction to water overcomes the competing entropic depletion force, and thus BE is above the crossover at which oil-water cohesion dictates the positive (repulsive) sign of the associated water-mediated hydrophobic interactions.

Our experimental results are obtained using Raman multivariate curve resolution (Raman-MCR) spectroscopy,^{3-4, 24} which we use to quantify aggregation induced changes in the hydration-shell spectra of BE. The inferred BE contact probabilities are compared with random mixing (RM) simulation predictions to estimate the BE contact free energy in water, which is subsequently compared with molecular dynamics (MD) simulation predictions obtained using two different potential functions. The present results extend our recent Raman-MCR studies of the aggregation of *tert*-butyl alcohol (TBA)^{7, 25} which quantified the depletion of the first hydration-shell water

molecules resulting from hydrophobic contacts between TBA molecules. However, the mathematical “rotational ambiguity” associated with MCR spectral decomposition^{4, 25-26} resulted in relatively large uncertainties in the concentrations of the monomeric (non-aggregated and aggregated TBA molecules. This rotational ambiguity essentially amounts to an uncertainty regarding the number of water molecules that are removed from the first hydration-shell of a solute as the result of solute-solute contacts. In our initial Raman-MCR studies of TBA²⁵ we assumed that bringing a pair of TBA molecules into direct contact produced an average depletion of 12.6%, while in our subsequent study, which combined Raman-MCR with femtosecond infrared (fs-IR) anisotropy measurements,⁷ it was concluded that TBA contacts produced between 25.5% and 71.3% depletion, thus leading to qualitatively similar, but quantitatively different conclusions regarding the concentration of monomeric and aggregated TBA molecules.

Here we describe an alternative analysis strategy that is more appropriate for quantifying contacts between flexible BE chains. This strategy quantifies the local hydration-shell depletion induced by contacts between CH groups on different BE molecules, each of which are expected to produce a substantial ($\sim 65\% \pm 15\%$) local depletion in the number of water molecules in the first hydration-shell surrounding each individual contacted CH group. Moreover, we use MD simulations to correlate the probability of such CH contacts with the probability that a solute will have either no contacts (and so is classified as a monomer) or at least one contact (and so is classified as aggregated). The primary benefit of this new analysis strategy derives from the fact that each CH contact must necessarily produce a significant depletion in the local number of hydration-shell water molecules, while the total experimentally measured depletion arises from the sum of the individual contact depletions, and thus is expected to depend on solute concentration. Furthermore, we have used MD simulation results to correlate the number of CH contacts with BE aggregate concentrations, and thus obtain experimentally derived BE contact free energy.

The remainder of this manuscript is organized as follows. Section 2.3 describes the experimental and simulation methods used to obtain the present results. Section 2.4 quantifies experimentally-derived estimates of BE aggregate concentrations and the corresponding water-mediated contact free energy, as well as compares the experimental results with both MD and RM simulation predictions. The conclusions and the implications of our results are summarized in Section 2.5.

2.3 Methods

2.3.1 Experimental

Aqueous solutions of BE (ethylene glycol butyl ether $\geq 99.0\%$, Sigma-Aldrich) were prepared by weight using ultrapure water (Milli-Q UF plus, Millipore), with an electrical resistance of $18.2 \text{ M}\Omega \text{ cm}$. The molar concentrations of BE solutions were determined from density measurements obtained using an Anton Paar DSA 5000 Density and Sound Velocity Analyzer (as described in Section 2.6.1). Moreover, we have previously shown that molar concentrations estimated using infinite dilution partial molar volumes are essentially the same as those obtained using density measurements (up to 4 M),⁷ and thus our concentrations are consistent with a BE partial molar volume of 0.12 M^{-1} (in a dilute aqueous solution, $0 < [\text{BE}] < 1.1 \text{ M}$, at 293 K). Duplicate Raman spectra were collected for each sample at $20 \text{ }^\circ\text{C}$ using an Ar-ion excitation laser ($\lambda = 514.5 \text{ nm}$) with a power of $\sim 15 \text{ mW}$ at the sample, and an integration time of 5 minutes per spectrum. Other details pertaining to the home-built Raman spectrometer, and MCR analysis procedures, are the same as those previously reported,³ unless noted otherwise in Section 2.4.1.

2.3.2 Random Mixing

Random mixing simulations were performed by generating non-overlapping configurations of solute molecules with random orientations and conformations, and concentrations between 0.25 M and 1.0 M. More specifically, one thousand statistically independent configurations were generated by inserting 10 solute molecules at random positions with random orientations in cubic boxes of volumes ranging from 17 nm^3 to 66 nm^3 , with periodic boundary conditions. For BE, 10 solute conformations were randomly selected from a database of conformations (generated from MD simulations of a single non-rigid solute molecule in water).¹¹ Note, however, that over the selected concentration range (0.25-1.0 M), our RM results indicate that the number of solute-solute direct contacts are approximately independent of whether the RM simulations were performed using random conformations or all trans conformations.²⁷ In obtaining the RM configurations, we rejected all configurations that contained any core-overlaps between solute molecules, where a core-overlap is defined as one in which any of the heavy atoms on different molecules were separated by a distance of less than $r_l = 3.74 \text{ \AA}$, which is consistent with

the location of the leading edge in the carbon-carbon radial distribution function $g(r)$ obtained from MD simulations of aqueous solutions of BE¹¹ and is approximately the same as the Lennard-Jones diameter of a methyl group (~ 3.73 Å).²⁸

A direct (as opposed to water-separated) hydrophobic contact was defined as a configuration for which any of the CH hydrogen atoms on any methyl or methylene group in a BE molecule is in contact with a CH group on a different BE molecule. Two different upper-bound H \cdots H distance cut-offs of either $r_2 = 2.4$ Å or $r_2 = 3.4$ Å were used to identify a contact. These two cut-off distances were obtained from the first maximum and first minimum in the BE hydrogen-hydrogen radial distribution function. The resulting number of direct hydrophobic contacts between BE molecules was then used to calculate the probability that a given BE has no contacts with any other BE (and thus is classified as a monomer). The RM monomer concentrations were obtained by multiplying each of the latter monomer probabilities by the total BE concentration. The concentration of aggregated BE molecules (defined as BE molecules that are in contact with at least one other BE) is obtained by subtracting each of the monomer concentrations from the total solute concentration. Note that approximately the same results are obtained when a hydrophobic contact is defined in terms of the carbon-carbon rather than hydrogen-hydrogen separation, with a carbon-carbon contact (upper-bound) distance of 4.9 Å.⁷

2.3.3 Molecular Dynamics Simulations

In addition to performing new MD simulations (described below), Prof. Gren Patey provided configuration files obtained using large-scale MD simulations of aqueous BE performed using CHARMM-AA/TIP3P,¹¹ at solute mole fractions below 0.04 (<2 M). We analyzed these configurations to obtain the number of contacts between BE molecules using the same procedure used to identify contacts in the RM simulations (as described above, in Section 2.3.2), and thus obtained MD predictions of the BE monomer and aggregate concentrations.

Additionally, new MD simulations were performed using GROMACS 5.1.2²⁹ to compute potentials of mean force (PMFs) between two BE molecules dissolved in water (as well as in the gas phase), using two different force fields: CHARMM-AA³⁰⁻³³/TIP3P³⁴ and TraPPE-UA/TIP4P-2005³⁵ with the HH-alkane model for the alkyl-water interactions.³⁶ Note that the TraPPE-UA/TIP4P-2005 force field is parameterized to accurately predict the phase diagrams of pure

alkanes,^{28,37} as well as the solvation thermodynamics of alkanes.³⁶ The ether and hydroxyl groups were represented using TraPPE³⁸⁻³⁹ and their interactions with water were represented using the Lorentz-Berthelot combining rules implemented in GROMACS. See Section 2.6.4 for further details.

2.4 Results and Discussion

2.4.1 Raman-MCR Hydration-Shell Spectroscopy

Figure 2.1 shows (A) raw Raman spectra and (B) Raman-MCR solute-correlated (SC) spectra obtained from aqueous BE solutions at 20 °C. More specifically, the minimum area SC spectra were obtained using self-modeling curve resolution (SMCR)⁴⁰ to analyze individual pairs of spectra, one obtained from pure water and the other from a BE solution. The resulting SC spectra were each normalized to the BE CH stretch band area, so that the corresponding hydration-shell features pertain to the average hydration-shell of an individual BE molecule at a particular concentration. The resulting hydration-shell OH stretch feature, between ~ 3000 and 3800 cm^{-1} in Figure 2.1B, arise primarily from water molecules whose OH stretch band is perturbed by BE, so it differs from that of bulk water. Previous comparisons of the Raman-MCR spectra of 1,2-hexanediol and 1-hexanol,⁴¹ as well as phenol and benzene² have demonstrated that hydroxyl groups on solute molecules do not significantly contribute to Raman-MCR hydration-shell spectra.

Comparisons of Raman-MCR and fs-IR anisotropy measurements of aqueous TBA solutions have confirmed that the hydration-shell OH stretch band areas appearing in CH normalized SC spectra, such as those shown in Figure 2.1B, are proportional to the average number of perturbed first hydration-shell water molecules around each solute.⁷ In other words, contacts between solute molecules lead to a reduction in the number of first hydration-shell water molecules, as quantified using the observed decrease in the Raman-MCR SC OH band area. Thus, we infer that the decrease in the hydration-shell OH band area in Figure 2.1B is proportional to the decrease in the number of perturbed water molecules in the hydration-shell of each BE molecule, and that this decrease is proportional to the decrease in the total number of first hydration-shell water molecules per BE. Note that the decrease in the number of hydration-shell water molecules must arise from BE aggregation since no such decrease would be expected if all BE molecules retained complete (non-overlapping) hydration-shells.

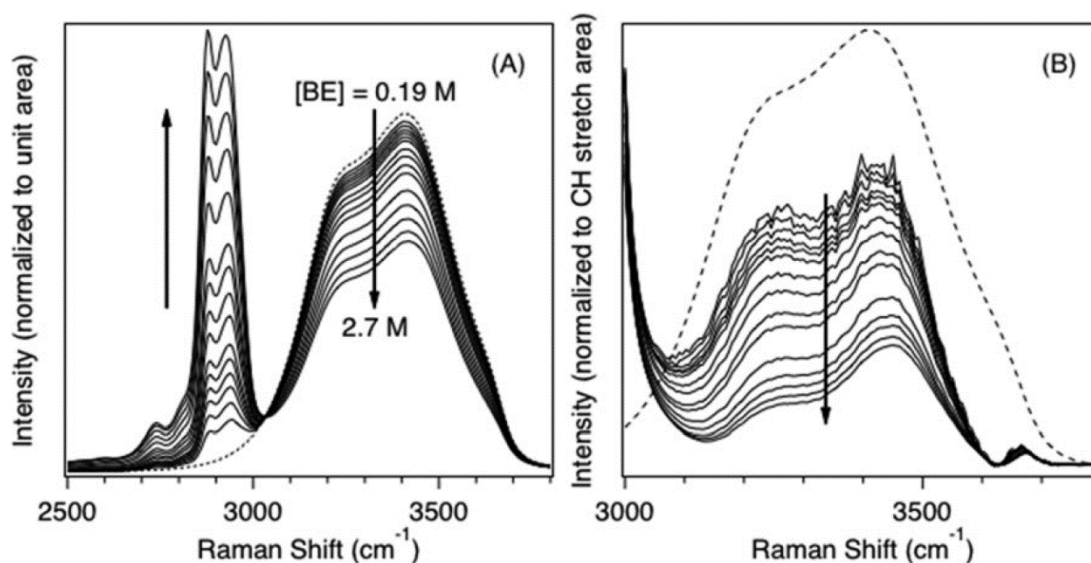


Figure 2.1 (A) Raman spectra (normalized to unit area) of pure H₂O (dotted black) and aqueous BE solutions of different concentration (0.19, 0.29, 0.38, 0.46, 0.55, 0.64, 0.80, 0.94, 1.1, 1.3, 1.6, 1.9, 2.2, 2.4, and 2.7 M). (B) Minimum area SC spectra of BE obtained from the spectra shown in (A), each normalized to the same total CH band area (only the high frequency edge of the CH band is shown in (B)).

More specifically, we use the hydration shell depletion percentage $d\%$, defined as follows, to quantify the decrease in the SC (CH normalized) OH integrated band area I , relative to its area I_0 in a dilute (0.2 M BE) solution.

$$d\% = 100 \left(\frac{I - I_0}{I_0} \right) = 100 \left(\frac{n - n_0}{n_0} \right) \quad 2.1$$

The second equality follows from our assumption that hydration-shell OH band area is proportional to the corresponding number of water molecules (n) in the first hydration-shell of BE in a given solution compared to the number of water molecules (n_0) in the first hydration-shell of a fully hydrated BE molecule.

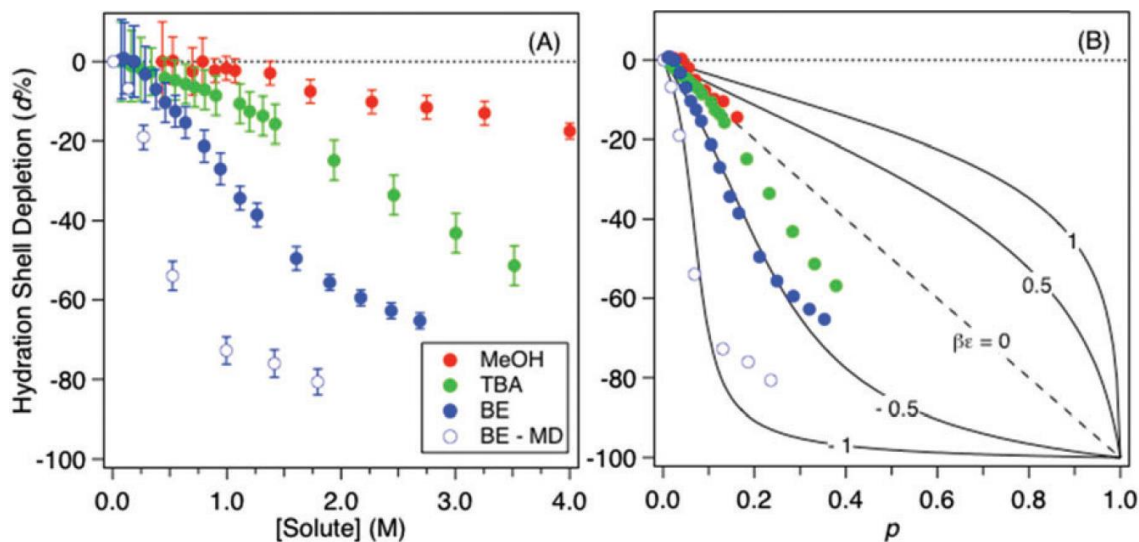


Figure 2.2 Raman-MCR hydration shell depletion percentage for aqueous methanol (MeOH, red points), TBA (green points), and BE obtained either experimentally (solid blue points) or from CHARMM-AA/TIP3P MD simulations¹¹ (open blue points), plotted as a function of solute molarity (A) or volume fraction p (B). The black curves are WRM predictions obtained assuming several different solute-solute contact energies, where $\beta\epsilon = 0$ pertains to an idealized random mixture.

The solid points in Figure 2.2A show how the resulting depletion percentages depend on molar concentration for BE, along with previously published results for methanol and TBA,⁷ and the open points correspond to MD predictions for aqueous BE (obtained using CHARMM-AA/TIP3P).¹¹ Thus, in the dilute limit (*i.e.* ≤ 0.2 M) all of these solutes are essentially fully hydrated (as $d\% \sim 0$). The results in Figure 2.2A show how the magnitude of the depletion percentage increases with increasing solute concentration, as well as with solute size. For example, at a solute concentration of ~ 1 M, the hydration shell depletion of methanol, TBA, and BE are $<2\%$, $\sim 10\%$, and $\sim 30\%$, respectively.

The MD simulation points in Figure 2.2A were obtained using Equation 2.1, where n_0 and n were determined by counting the number of water molecules within r_2 of any of the six carbon atoms of BE. The value of r_2 was taken to be equal to either the first ($r_2 = 3.8$ Å) or second ($r_2 = 4.9$ Å) maximum in the corresponding carbon-oxygen radial distribution function, and the error bars on the MD points reflect the range of $d\%$ values obtained when varying r_2 . Note that the MD percent depletion results are relatively insensitive to the precise r_2 cut-off value chosen for analysis, as well as to whether all the carbons or only the four outermost (butyl group) carbons are used to

obtain n_0 and n . The magnitudes of the MD $d\%$ values are invariably larger than the experimental $d\%$ values, indicating that the MD simulations predict more aggregation than experimentally observed (as further described in Sections 2.4.2 and 2.4.3).

As a first pass in interpreting the experimental results shown in Figure 2.2A we have compared them with depletion predictions obtained using a finite-lattice weighted random mixing (WRM) model,⁴² which was used to produce the curves in Figure 2.2B. The dashed line represents finite lattice random mixing (FL-RM) predictions and the solid curves represent WRM predictions obtained assuming various assume values of the BE contact energy ε (with $\varepsilon < 0$ pertaining to an attractive contact energy, and $\beta\varepsilon = \varepsilon/RT$, when ε is expressed in molar units). Thus, the fact that the methanol points are consistent with the $\beta\varepsilon = 0$ predictions implies that methanol contacts are consistent with FL-RM predictions, while TBA contacts only deviate slightly from FL-RM predictions. On the other hand, the experimental and MD simulation results for BE are consistent with larger negative values of $\beta\varepsilon$, indicating a more substantial net attractive interaction between BE molecules. Further details regarding how the WRM predictions were obtained are provided in Section 2.6.3. The free energy associated with such contacts may be more accurately estimated as described in Section 2.4.3.

2.4.2 Quantification of Hydrophobic Contacts

In order to obtain a quantitative estimate of the number of monomeric and aggregated solute molecules, a second round of SMCR was used to decompose the SC spectra shown in Figure 2.1B into monomer and aggregate components.⁷ More specifically, the 0.2 M BE CH-normalized SC spectrum in Figure 2.1B is attributed to monomeric BE molecules (with essentially no solute-solute contacts). The latter assignment is supported by our observation that both the normalized SC OH area and the BE CH peak frequency of BE remain approximately constant below 0.2 M (shown in Figure 2.2 and Section 2.6.2, respectively). We performed a second round of SMCR to decompose the SC spectra shown in Figure 2.1B into a linear combination of two spectra, one of which pertains to the BE monomer, and the other to the minimum area Raman-MCR component arising from contacting (aggregated) BE molecules.

Figure 2.3A shows the resulting monomer (blue) and aggregate (red) spectral component spectra. These results indicate that the aggregate spectral component has an OH band area that is

depleted by ~65% relative to the monomer spectral component. We attribute this to the local depletion of the hydration-shell in the immediate neighborhood of a contact between CH hydrogen atoms on two different BE molecules. The shaded region in Figure 2.3A spans the upper and lower bound estimates of the minimum area aggregate component spectra obtained by performing the second round of SMCR either using SC spectra obtained from BE concentrations below 0.55 M or using all the SC spectra obtained from BE concentrations up to 2.7 M.

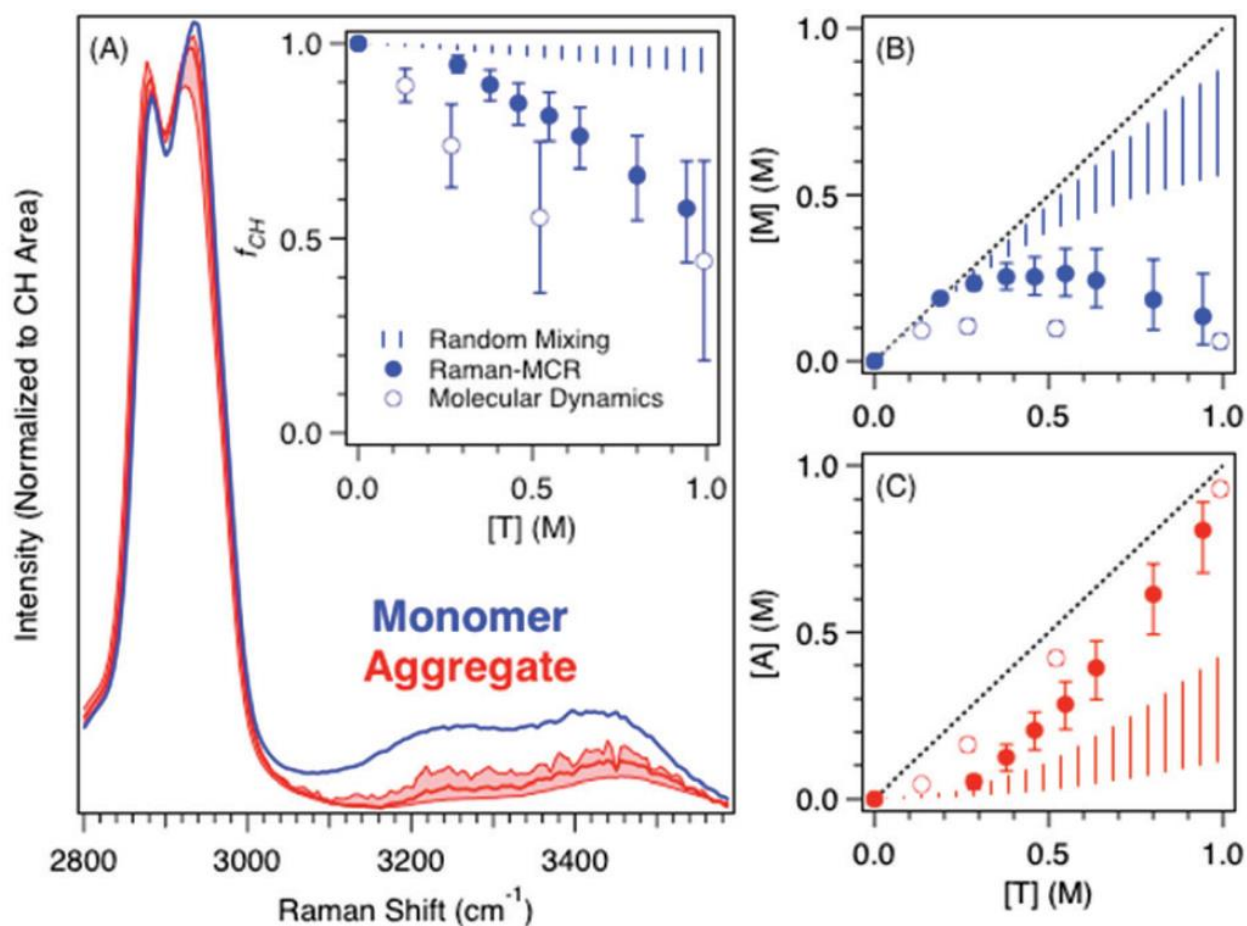


Figure 2.3 (A) Monomer (blue) and aggregate (red) component spectra obtained from the second round of SMCR applied to the SC solution spectra in Figure 2.1B (A, inset) Relationship between non-contacting CH fraction f_{CH} and total BE concentration from Raman-MCR experiments (solid points), MD simulations (open points), and RM predictions (dashed regions). (B) Monomer concentrations and (C) aggregation concentrations obtained from Raman-MCR experiments (using the MD correlation between f_{CH} and the f_M , shown in Figure 2.4), MD simulations, and RM predictions for BE. The black dashed line corresponds to the total solute concentration.

The solid points in the inset panel in Figure 2.3A represent the fractional contribution (f_{CH}) of the monomer spectral component to each of the spectra shown in Figure 2.1B. The monomer fractions were obtained from the ratio of the CH area of the monomer component to the total CH area (as obtained from the second round of SMCR decomposition), and the corresponding error bars indicate the range of results obtained when varying the assumed aggregate spectra from the upper to the lower bounds shown in Figure 2.3A. The shaded region in Figure 2.3 represents RM predictions (obtained as described in Section 2.3.2). The results in Figure 2.3A indicate that the non-aggregated CH fraction f_{CH} decreases approximately linearly with solute concentration. Furthermore, the MD simulation results for aqueous BE, which were obtained as described in Section 2.3.3, predict that there are slightly fewer non-aggregated CH groups (and thus more aggregation) than determined from the Raman-MCR experimental results.

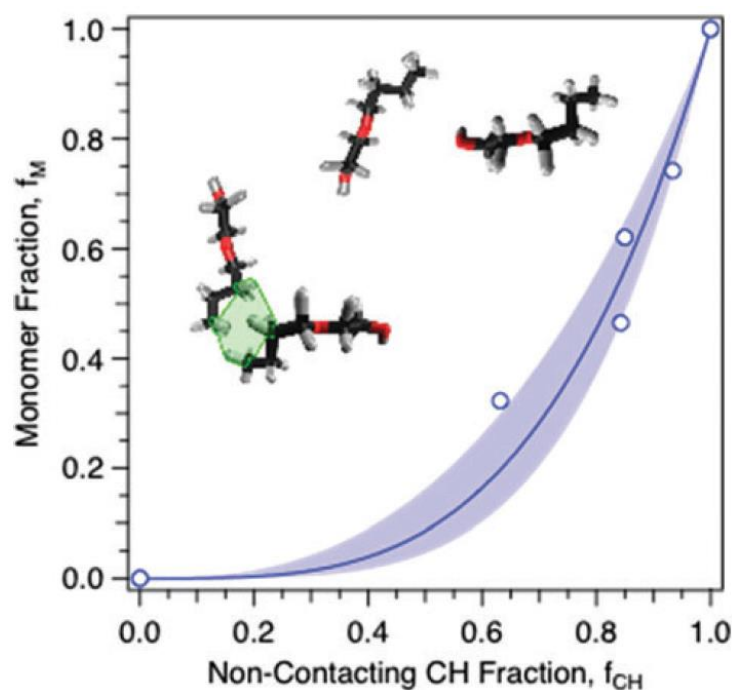


Figure 2.4 Correlation between the number of non-aggregated monomer BE molecules and the number of non-contacting CH groups, obtained from MD simulations. The solid curve is a power-law fit. The inset image illustrates the relationship between f_{CH} and f_{M} for a particular configuration of four BE molecules, for which $f_{\text{CH}} = 44/52 = 0.85$ and $f_{\text{M}} = 2/4 = 0.5$.

Figure 2.3B compares the resulting experimental BE monomer concentration estimates (solid points) with the corresponding MD (open points) and RM (dashed region) predictions. The experimental monomer concentrations were obtained from the non-contacting CH fractions (f_{CH}) shown in Figure 2.3A by using the MD results to infer the correlation between CH contacts and monomer concentration (as shown in Figure 2.4, and further described below). Note that the latter correlation is expected to be relatively insensitive to variations in the simulation potential functions and the amount of aggregation in the simulations. The fact that the experiments predict fewer monomers (and thus more aggregates) than RM predictions implies that the aggregation potential of mean force has a favorable (attractive) contact free energy (as further discussed and quantified in the next sub-section).

2.4.3 Water-mediated Interaction Energy

The results in Figure 2.3, combined with the following procedure, were used to estimate the BE contact free energy (ΔG), in excess of a random mixture. More specifically, the experimentally obtained concentration of aggregated (non-monomeric) BE molecules can be expressed as $[A] = [T] - [M]$, where $[T]$ and $[M]$ are the total and monomer BE concentrations. The corresponding RM prediction for the concentration of aggregated BE molecules is $[A]_{\text{RM}}$. The ratio of the experimental and RM concentrations is used to estimate the free energy difference between the experimental and random contacts.

$$\Delta G \cong -RT \ln \left(\frac{[A]}{[A]_{\text{RM}}} \right) \quad 2.2$$

In other words, this free energy reflects the excess probability of observing a contact in the experimental and randomly mixed system. Thus, this ΔG represents an experimental estimate of the minimum value of the potential of mean force associated with bringing two solute molecules into contact with each other.

To compute that latter contact free energy, we performed MD simulations (described in Section 2.6.4) to obtain the total $[w(\tau)]$ and direct $[u(\tau)]$ potentials of mean force using two different force fields: CHARMM-AA/TIP3P and TraPPE-UA/TIP4P-2005/HH-alkane.

$$w(\tau) = u(\tau) + \Delta w(\tau) \quad 2.3$$

τ represents the distance between the center of mass of the two BE molecules.⁸ The water-mediated contribution $\Delta w(\tau)$ to the mean force potential between BE molecules in water is equivalent to the difference between $w(\tau)$ and $u(\tau)$.

Figure 2.5 shows the resulting total, direct, and water-mediated interaction free energies for BE. The total $w(\tau)$ is calculated for two BE molecules in water while the direct interaction energy $u(\tau)$, which is equivalent to the potential of mean force between the two isolated BE molecules, is obtained from simulations containing two isolated (gas phase) EB molecules (representative of the hydrophobic part of BE). In other words, we assume that $w(\tau)$ is not significantly influenced by the hydroxyl group of BE (as the hydroxyl group is likely to be H-bonded to water in both the monomer and aggregate configurations). Thus the direct interaction between two BE molecules is expected to closely resemble the interaction between EB molecules in the gas phase.

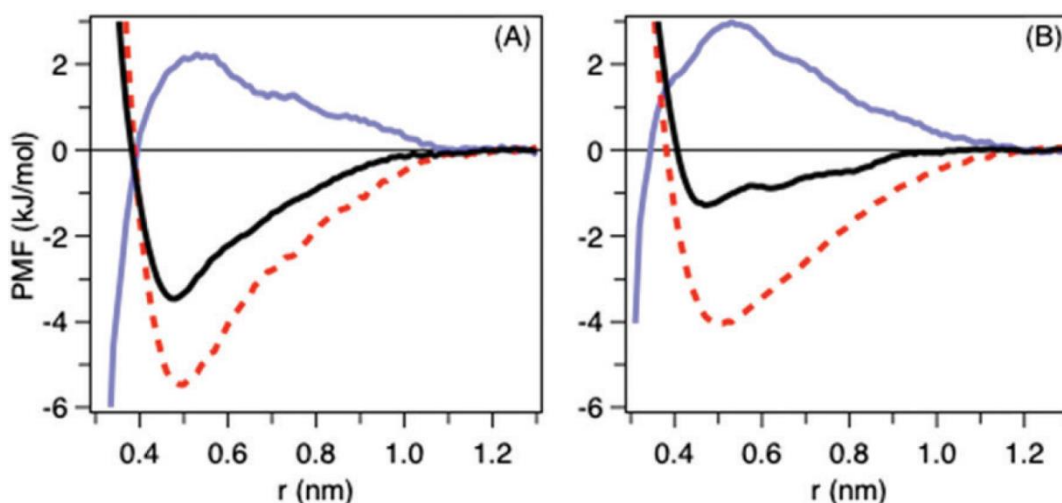


Figure 2.5 Total potentials of mean force (solid black) between BE molecules are compared with the corresponding direct (dashed red) and water-mediated (solid blue) contributions calculated using two different force fields: (A) CHARMM-AA/TIP3P and (B) TraPPE/TIP4P-2005 with HH-alkane modifications.³⁶

The results shown in Figure 2.5A and B demonstrate that there is a quite substantial difference between the potentials of mean force minima predictions obtained using the two classical force fields. More specifically, the predicted contact minima in solution (solid black curves) range from $w(\tau) = -3.5 \pm 0.2 \text{ kJ mol}^{-1}$ to $-1.3 \pm 0.3 \text{ kJ mol}^{-1}$, both of which are of the same magnitude as the experimentally obtained contact free energy of $\Delta G \approx -3.0 \pm 0.4 \text{ kJ mol}^{-1}$ (Equation 2.2). Additionally, the predicted contact minima in the gas phase (dashed red curves) range from $u(\tau) = -5.5 \text{ kJ mol}^{-1}$ to -4.0 kJ mol^{-1} . Moreover, the two simulations agree in predicting a water-mediated contact free energy of $\Delta w \approx +2.5 \pm 1 \text{ kJ mol}^{-1}$. This predicted water-mediated contact free energy is remarkably close to the corresponding experimentally derived estimate of $\Delta w = +1.5 \pm 0.6 \text{ kJ mol}^{-1}$, which was calculated by averaging the difference between the experimental contact free energy ($\Delta G \sim w(\tau)$) and the direct interaction energy obtained from both force fields.

2.5 Conclusions

We have used Raman-MCR, RM predictions, and MD simulations to quantify both the total and water-mediated free energy associated with bring two BE molecules into contact with each other in water. Both our experimental results and MD predictions imply that Δw is positive, and thus water drives BE molecules apart, rather than pushing them together. However, the direct interaction energy u between the BE chains is sufficiently large and attractive that the net contact potential of mean force w remains slightly attractive, although less attractive than it would have been in the absence of water, and just barely large enough to effectively compete with thermal energy fluctuations of the order of $RT \sim 2.5 \text{ kJ mol}^{-1}$.

Our experimentally estimated contact free energies are in reasonable agreement with the contact potentials of mean force obtained from using MD simulations (with two different force fields). However, the large scale aqueous BE simulations performed using the CHARMM-AA/TIP3P force field predict somewhat more BE aggregation than we observe experimentally. The TraPPE/TIP4P-2005 force field, on the other hand, predicts a smaller (less attractive) contact potential of mean force, and thus is expected to produce significantly less BE aggregation. Previous MD simulations of the potentials of mean force between alkanes, as well as fullerenes, dissolved in water predict a size dependent crossover in the sign of the water-mediated interaction free energy, as Δw is predicted to be negative for solutes smaller than neopentane (which has five carbons) and positive for solutes larger than neopentane.²³ Our BE results confirm that Δw is

positive for BE (which has six carbons). However, previous Raman-MCR results have implied that Δw is also positive for solutes as small as methanol. It is not yet clear whether experiments are consistent with the MD prediction that Δw becomes increasingly positive with increasing solute size.⁸⁻⁹

2.6 Supplementary Information

Here we provide additional experimental and simulation details and results. These include density-based aqueous BE solution concentration unit conversion (molality to molarity) and vibrational frequency shifts observed for the CH stretching region of concentration-dependent BE spectra. Furthermore, a description of the WRM predictions and MD simulation parameters and analysis details are given below.

2.6.1 Density-Based Unit Conversions

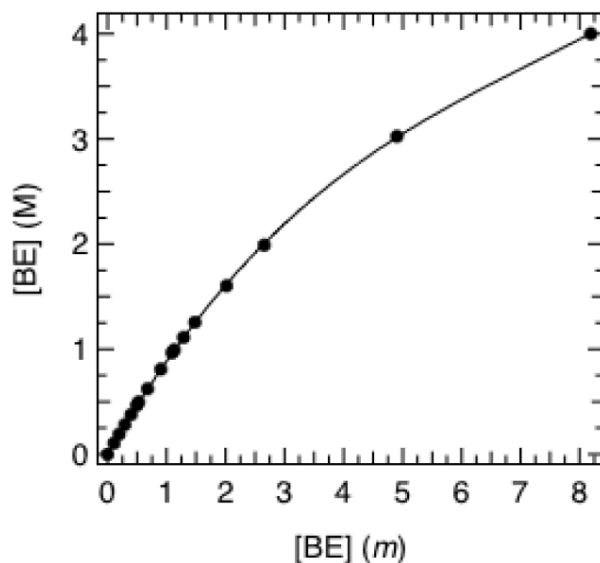


Figure 2.6 BE molality and molarity measured values (solid points) fit by a fourth-order polynomial (solid curve), $M = 0.97625m - 0.094847m^2 + 0.0043131m^4$.

Density measurements for aqueous BE solutions of varying known molality (m) concentration were collected at 20°C using an Anton Paar DSA 5000 Density and Sound Velocity Analyzer. Using these density values, BE molality was converted to molarity (M). Thus, additional BE molality values were converted to molarity values using the fourth order polynomial relationship between the two, shown in Figure 2.6.

2.6.2 CH Peak Frequency Shifts for BE

CH frequency shifts were calculated by fitting the symmetric and asymmetric CH stretches of BE to high order polynomial functions. The results for both CH peak shifts from a starting location of $\sim 2884 \text{ cm}^{-1}$ and $\sim 2936 \text{ cm}^{-1}$ (at a concentration of 0.1 M) for the symmetric and asymmetric peaks, respectively, are shown in Figure 2.7. As with the OH area depletion, there is a relatively concentration independent CH frequency up to 0.2 M BE, suggesting that BE is fully hydrated up to 0.2 M. The total change in CH peak location for 0.08-2.7 M BE for the symmetric peak ($\nu_{\text{sym}} \sim 5 \text{ cm}^{-1}$) is almost half of that observed for the asymmetric peak ($\nu_{\text{asy}} \sim 9 \text{ cm}^{-1}$).

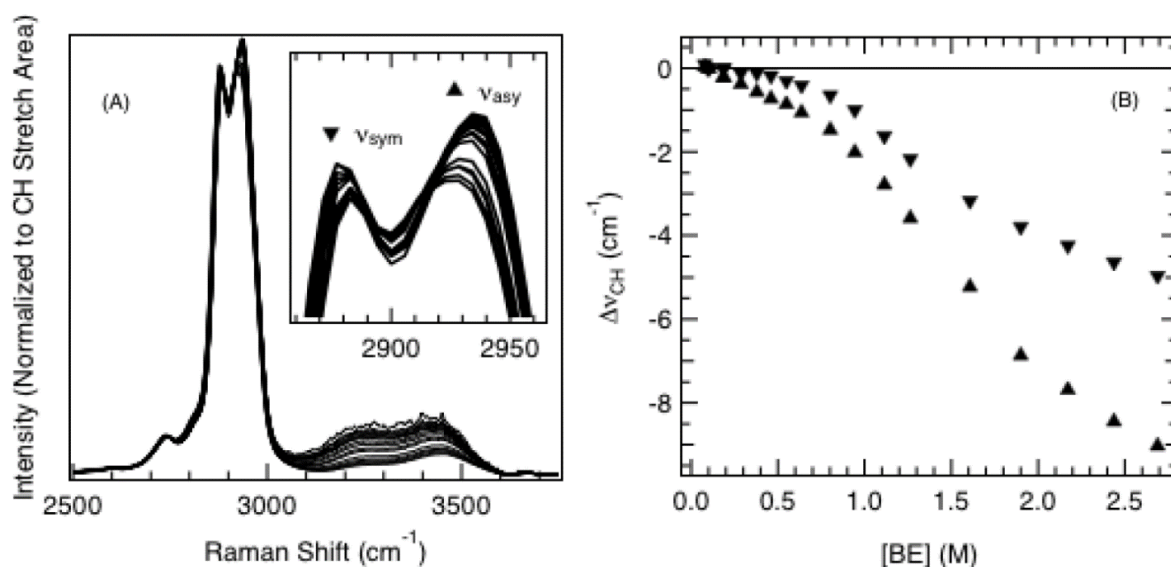


Figure 2.7 (A) SC spectra of aqueous BE solutions (0.1 M – 2.7 M) showing the CH peak region ($2500 \text{ cm}^{-1} - 3050 \text{ cm}^{-1}$) with the symmetric ($\nu_{\text{sym}} \sim 2880 \text{ cm}^{-1}$, down triangles) and asymmetric ($\nu_{\text{asy}} \sim 2935 \text{ cm}^{-1}$, up triangles) stretching modes shown in the inset panel. (B) The change in Raman shift frequency for each of the modes ($\Delta\nu_{\text{CH}}$) from their corresponding peak frequency determined at $[\text{BE}] = 0.1 \text{ M}$.

2.6.3 Finite Lattice Predictions

The WRM predictions shown in Figure 2.2B are obtained by converting the solute concentrations to a dimensionless cell occupancy probability $p = [c]/[c]_{liq}$ where $[c]$ is the solute concentration and $[c]_{liq}$ is the solute concentration in the pure solute liquid. The WRM $d\%$ predictions in Figure 2.2B were obtained assuming that each solute-solute contact removes water from one of the $N = 12$ hydration-shell lattice sites, such that $d\% = -100\langle k\rangle/N$, where $\langle k\rangle$ is the average number of other solute molecules that are in contact with a given solute molecule (and therefore a system composed entirely of non-aggregated monomers would have $\langle k\rangle = 0$). Note that $N = 12$ corresponds to the assumed coordination number in the pure solute liquid, and thus is also the maximum possible value of $\langle k\rangle$. The WRM predictions are quite insensitive to the precise values of N , particularly in relatively dilute solutions in which the number of solute contacts is invariably small compared to N . Note that defining p and $d\%$ in this way ensures that the depletion predictions approach physically reasonable limits at infinite dilution ($p = 0$, $d\% = 0$) and in the pure liquid ($p = 1$, $d\% = -100\%$).

2.6.4 MD Simulation Procedures

Computational results were obtained using GROMACS 5.1.2. We estimated potentials of mean force (PMFs) using umbrella sampling and weighted histogram analysis as a function of the distance (τ) between the centers of mass for a pair of BE molecules that were either isolated or dissolved in 1000 water molecules. Simulations *in vacuo* were carried out in the canonical ensemble using a leap-frog stochastic dynamics integrator for 1 ns with a time step of 1 fs, with center of mass translation removed, Coulombic and van der Waals interactions cut-off at 0.9 nm, V-rescale temperature coupling to 300 K, cubic box length of 4.5 nm, and all-bonds constrained using the LINCS algorithm. Simulations in water were carried out in the isothermal-isobaric ensemble using a leap-frog molecular dynamics integrator for 10 ns with a time step of 2 fs, with center of mass translation removed, Coulombic (calculated using Particle Mesh Ewald summation) and van der Waals interactions cut-off at 0.9 nm, Berendsen temperature and pressure coupling to 300 K and 1 bar, and all-bonds constrained using the LINCS algorithm. All umbrella sampling involved center of mass pulling of the two BE molecules in a series of 21 MD simulation windows using harmonic-restraint potentials with a force constant of 836.8 kJ/(mol·nm²) and varying BE-

BE equilibrium distance (0.35, 0.40, ..., 1.35 nm). The resulting distributions were corrected for entropic contribution $k_B T \ln(4\pi r^2)$, where k_B is Boltzmann's factor. Additionally, the baseline was corrected by subtracting the average entropy corrected PMF values between 1.15 and 1.35 nm, where BE-BE interactions are negligible.

We considered two different combinations of force fields: (A) CHARMM-AA for BE and TIP3P for water and (B) TraPPE-UA for BE, TIP4P-2005 for water, and HH-Alkane modifications for the alkyl-water cross interactions. Force field set "A" was chosen because it is the same force field that Patey's group used to obtain previously reported aqueous BE MD simulations, which were further analyzed for this article as seen in Figure 2.2, Figure 2.3, and Figure 2.4. Additionally, force field set "B" was chosen because TraPPE-UA accurately represents fluid hydrocarbon phase behavior, TIP4P-2005 excellently represents water densities, and the HH-Alkane modifications capture temperature hydrophobic hydration thermodynamic energy, enthalpy, and entropy values.

CHAPTER 3. HYDROPHOBIC HYDRATION SHELL WATER STRUCTURE

3.1 Abstract

The debate regarding whether hydrophobic hydration shells are “clathrate-like,” “ice-like,” or neither has continued for over 50 years. More recently, Raman multivariate curve resolution (Raman-MCR) studies of the OH stretch band of water in hydrophobic hydration-shells have found evidence of both hydrogen bond strengthening and the formation of broken hydrogen bonds (dangling OH groups).^{3, 43} Here we use Raman-MCR to show that the enhanced tetrahedral order in cold liquid water, as well as in solid clathrate hydrates and ice, gives rise to the emergence of a peak near 200 cm^{-1} whose intensity is correlated with the OH stretch shoulder near 3200 cm^{-1} . Moreover, we observe the same two correlated bands in the hydration-shells of oily molecules, thus providing clear experimental evidence of enhanced tetrahedral order in hydrophobic hydration-shells.

3.2 Introduction

The influence of oily molecules on water structure has long been a subject of speculation. Early thermodynamic evidence was interpreted as indicating the formation of "icebergs" around oily molecules.⁴⁴⁻⁴⁵ While more recent simulations⁴⁶⁻⁴⁹ and spectroscopy⁵⁰⁻⁵¹ studies agree with enhanced water structure in nonpolar hydration shells, there are also spectroscopy⁵² and neutron scattering⁵³ studies that found no evidence of such structures. Here, two characteristic features in Raman-MCR spectra of aqueous solutions, clathrate hydrates, ice, and water are studied. More specifically, upon clathrate hydrate formation, two strong Raman frequency bands appear, one near 200 cm^{-1} (OH \cdots O vibration between water molecules) and the other near 3200 cm^{-1} (O-H stretch of hydrogen bonded water). Additionally, pure ice and pure water Raman spectra also contain these two bands. In pure water the bands are much weaker than in either ice or clathrate hydrates and most clearly emerge when performing Raman-MCR to extract those spectral features that emerge as water is cooled from 100°C to 0°C . Previously (yet unreported), we noticed that hydration shell spectra of amphiphilic molecules also contained weak bands near these two Raman shift frequencies. Therefore, the goal is to determine if any of the bands that are seen upon either

clathrate hydrate formation, ice formation, or water cooling correspond to similar modes in the hydration shell of amphiphilic molecules.

Aqueous tetrahydrofuran (THF) solutions are known to form clathrate hydrates at ambient pressure and low temperature ($< 4^{\circ}\text{C}$, see Figure 3.1).⁵⁴⁻⁵⁶ Thus, I have performed Raman-MCR analysis of aqueous THF (0.5 M) versus temperature (0°C to 100°C) approaching the liquid to clathrate hydrate transition ($\sim -1^{\circ}\text{C}$ at $[\text{THF}] = 0.5 \text{ M}$). Even though extensive low frequency Raman results for aqueous THF have been reported,⁵⁴⁻⁵⁷ they have not shown how the 200 cm^{-1} band emerges in the liquid hydration shell before the solid clathrate hydrate phase begins to form (Figure 3.2B). Using Raman-MCR, as a function of both THF concentration and temperature, I have shown that the low frequency band appears in the solution prior to phase transition to the clathrate hydrate phase. Evidence of a low frequency ($\sim 200 \text{ cm}^{-1}$) vibrational mode in aqueous THF spectra suggests a connection between the more intense 200 cm^{-1} band seen in the Raman spectrum of the THF clathrate hydrate phase and the weak 200 cm^{-1} band observed in low temperature ($< 20^{\circ}\text{C}$) Raman-MCR hydrophobic hydration shell spectra. These results provide some of the first experimental evidence of clathrate-like hydration shells around molecular hydrophobic groups.

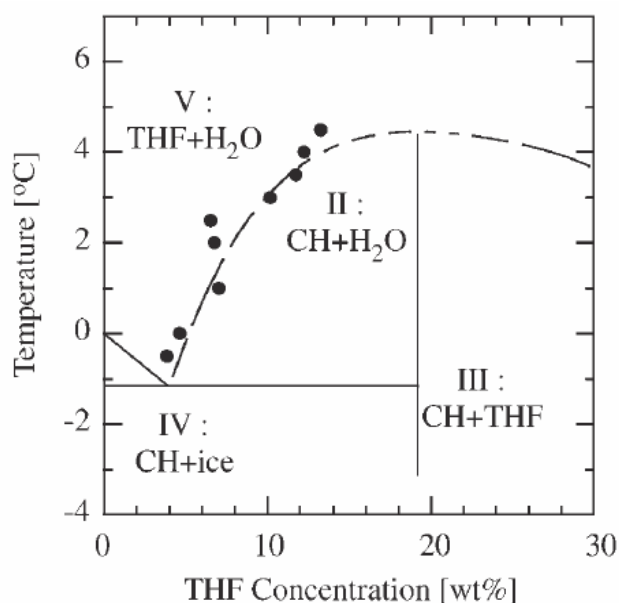


Figure 3.1 Aqueous THF phase diagram previously reported by Takasu et al.⁵⁵

3.3 Methods

Tetrahydrofuran (Fisher Chemical, 0.025% butylated hydroxytoluene as preservative), *d9-tert*-butyl alcohol (CDN Isotopes), *tert*-butyl alcohol (Sigma-Aldrich, $\geq 99.7\%$), methanol (Honeywell Burdick and Jackson, anhydrous), ethanol (Decon Laboratories, Inc., 200 proof), *n*-propyl alcohol (Mallinckrodt Chemicals, 99.8%), tetramethylammonium bromide (Sigma-Aldrich, 98+%), tetraethylammonium bromide (Aldrich Chemistry, 99%), tetrapropylammonium bromide (Aldrich Chemistry, 98%), and *d9*-trimethylamine N-oxide (Cambridge Isotope Laboratories, Inc., 98%) were used without further purification. Ultrapure filtered water (Milli-Q UF Plus, 18.2 M Ω ·cm, Millipore) was used to prepare all samples.

Each spectrum was collected for five minutes using the 514.5 nm Raman system described in Section 1.2. At temperatures below the dew point (usually 10°C and below), a steady, slow flow of room temperature argon or nitrogen gas was used to prevent condensation on the outside of the sample cuvettes. Duplicate aqueous solution spectra were analyzed using SMCR (Section 1.3) implemented in Igor Pro (WaveMetrics, Inc.) with pure water spectra taken at the same temperature as the reference. The SMCR analysis of temperature dependent pure water spectra shown in Figure 3.4 was achieved by simultaneously evaluating all six temperature dependent water spectra using the SMCR algorithm with the 100°C water spectrum as the reference. Pure ice and THF clathrate hydrate spectra (Figure 3.6) are reported as collected. Because of high scattering in crystalline solid samples, which leads to decreases in collected Raman signal, ice and THF clathrate hydrate samples were frozen in plastic (rather than glass) cuvettes that had a small (diameter ~2 mm) hole drilled in the front face of the cuvette. The small hole allowed direct interaction of the laser with the solid face of the sample and greatly reduced signal loss and spurious background that was observed when no hole was present. Care was taken when adding the liquid samples to these plastic cuvettes with holes so that the liquid did not leak out. The surface tension of the liquid and careful technique allowed for these samples to be successfully prepared.

The THF clathrate hydrate sample whose spectrum is shown in Figure 3.6B was made by preparing an aqueous 2.5 M (~19 wt%) THF solution. According to the aqueous THF phase diagram (Figure 3.1), 19 wt% corresponds to 100% THF clathrate hydrate. The 2.5 M solution was then placed in a freezer at -22°C overnight. The next day the sample was transferred from the freezer to the sample holder set to 2°C and allowed to equilibrate for about one hour.

3.4 Results and Discussion

Figure 3.2 shows the CH stretch (or CD stretch) normalized hydration shell spectra for *d9*-TBA and THF as a function of temperature obtained by decomposing the Raman spectra of the aqueous solutions into water and solute-correlated (SC) components. The latter SC component contains features arising from the vibrational modes of the solute, such as the CH stretching bands at $\sim 2900\text{ cm}^{-1}$ for THF, as well as features arising from hydration shell water molecules whose vibrational structure is perturbed by the solute, and thus, differ from bulk water. In other words, if the structure of the water molecules in the hydration shell was the same as the surrounding bulk water, then the features between ~ 3100 and 3700 cm^{-1} would not appear in the SC spectra. The lower frequency SC OH stretch (centered at $\sim 3200\text{ cm}^{-1}$) is more highly polarized than the remaining (higher frequency) SC OH features, and thus, has been assigned to tetrahedrally ordered water molecules.^{3, 58} The increasing intensity of this band with decreasing temperature is consistent with a cold water, ice-like, or clathrate-like structure, as this peak is significantly enhanced in the Raman spectrum of pure ice or pure clathrate hydrate (Figure 3.6). Note that this intensity increase is more notable for TBA than for THF for both the low ($\sim 200\text{ cm}^{-1}$) and high ($\sim 3200\text{ cm}^{-1}$) frequency modes.

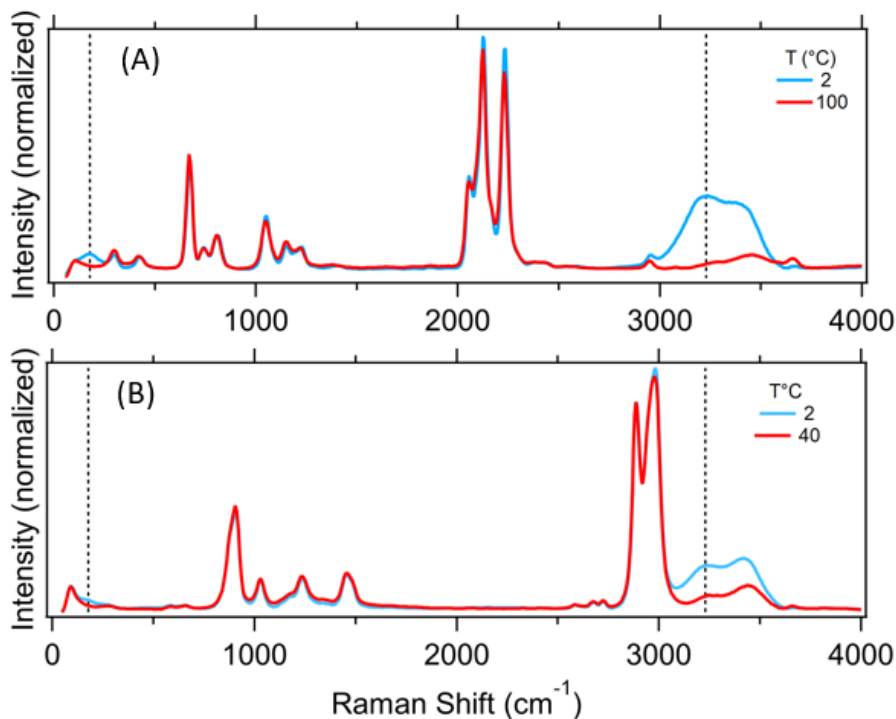


Figure 3.2 Hydration shell Raman-MCR spectra for (A) *d9*-TBA at low (2°C) and high (100°C) temperature (collected by Dr. Blake Rankin) and (B) THF at low (2°C) and high (40°C) temperature. Black dashed lines correspond to 177.85 cm⁻¹ and 3229.7 cm⁻¹.

Even though full spectra were only shown for TBA and THF in Figure 3.2, hydration shell spectra were obtained and analyzed for several small amphiphilic molecules. From these hydration shell spectra (summarized in Figure 3.7 and Figure 3.8), a correlation between the intensity of the low frequency peak (~ 200 cm⁻¹) and the high frequency peak (~ 3200 cm⁻¹) was derived and shown in Figure 3.3. Surprisingly, among eight small amphiphilic molecules along with the low temperature component of pure water (discussed in the next paragraph), this intensity correlation is quite similar and follows an approximately linear trend.

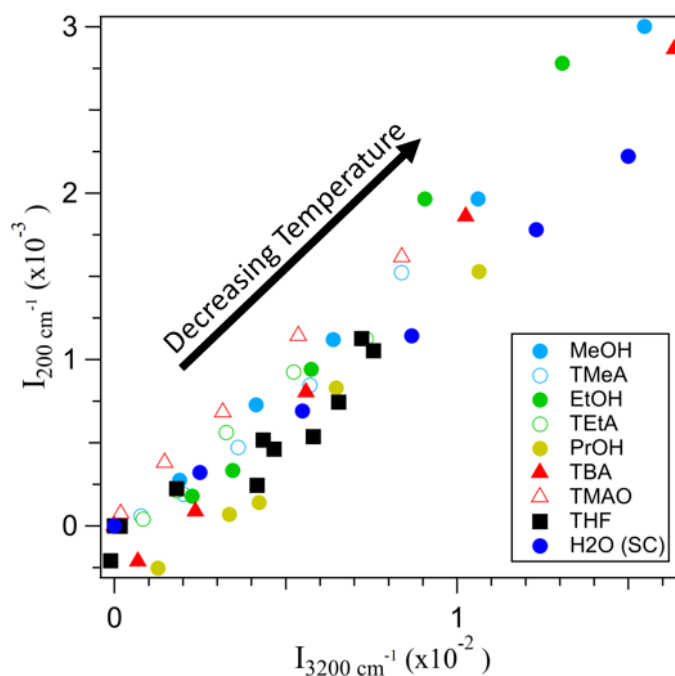


Figure 3.3 Correlation between the low and high frequency peak intensities for methanol (MeOH), tetramethylammonium (TMeA), ethanol (EtOH), tetraethylammonium (TEtA), n-propanol (PrOH), TBA, trimethylamine N-oxide (TMAO), THF, and low temperature component derived from MCR analysis of pure water (see Figure 3.4).

Figure 3.4A shows raw Raman spectra of pure water with respect to temperature. Upon MCR analysis of all six temperature-dependent spectra, where the 100°C pure water spectrum is used as the reference, a second component is isolated. As shown in Figure 3.4B, when temperature is decreased the second component increases intensity in namely two regions: a low frequency region ($\nu_{\max} = 186.57 \text{ cm}^{-1}$ at 2°C) and a high frequency region ($\nu_{\max} = 3209.4 \text{ cm}^{-1}$ at 2°C). The frequency of maximum intensity for these two regions are similar, but the low frequency is blue-shifted and the high frequency is red-shifted from those in the low temperature hydration shell spectra of TBA and THF.

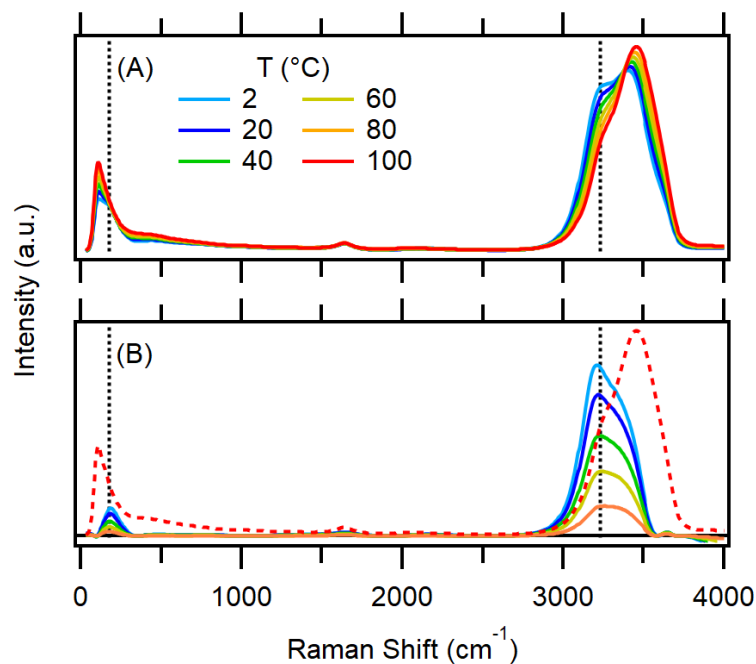


Figure 3.4 (A) Temperature dependent pure water raw Raman spectra. (B) Raman-MCR spectra (low temperature components) obtained from using the 100°C temperature spectrum (dashed red) as the reference. Black dashed lines correspond to 177.85 cm⁻¹ and 3229.7 cm⁻¹.

Additionally, Prof. Kenji Mochizuki computed the tetrahedral order parameter (q)^{46, 59-60} for bulk TIP4P/2005 water as a function of temperature. Figure 3.5 shows the relationship between q and the peak height at 186.6 cm⁻¹ or at 3200 cm⁻¹ for the low temperature component (shown in Figure 3.4B) of each temperature dependent pure water spectrum. There is a direct linear relationship between the intensity of both the low and high frequency modes found at decreasing temperatures in our experiments and the tetrahedrality of bulk water derived from simulations.

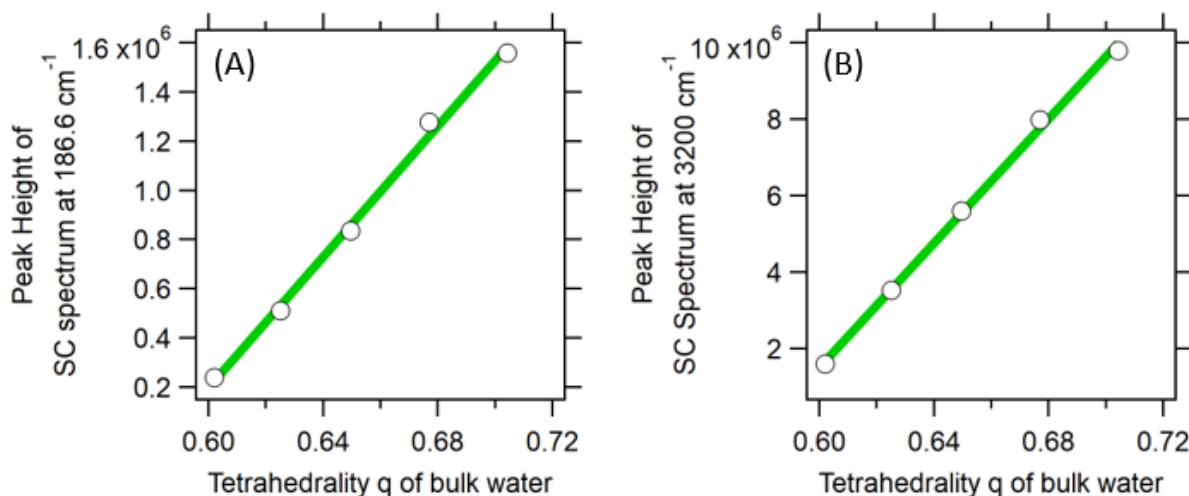


Figure 3.5 Correlation between the tetrahedral order parameter (q) of bulk water and the (A) low and (B) high frequency peak intensities from Figure 3.4B.

Figure 3.6A shows the raw Raman spectrum of pure ice at -2°C and Figure 3.6B shows the raw Raman spectrum of pure THF clathrate hydrate at 2°C . In both ice and THF clathrate hydrate spectra there is sharp intensity in both the low and high frequency regions reminiscent of the intensity increase in these two regions for the hydration shell of TBA and THF with decreasing temperature. Again, like in pure water the low frequency peak is blue-shifted and the high frequency peak is red-shifted with respect to the hydration shell peak positions for TBA and THF. The peak positions and frequency shifts compared to the TBA hydration shell peak positions are summarized in Table 3.1. The increasingly blue-shifted low frequency peak and red-shifted high frequency peak from hydrophobic hydration shell to clathrate hydrate to ice indicates that the enhanced water structure in hydrophobic hydration shells is still only a very small fraction of that seen in clathrate hydrates or ice. This is consistent with recent MD simulation results found by Galamba.⁴⁶ Additionally, preliminary MD simulations performed by Prof. Hank Ashbaugh's group at Tulane University show only a 1% increase in tetrahedrality for the hydration shell of ethanol with respect to bulk water at 0°C .

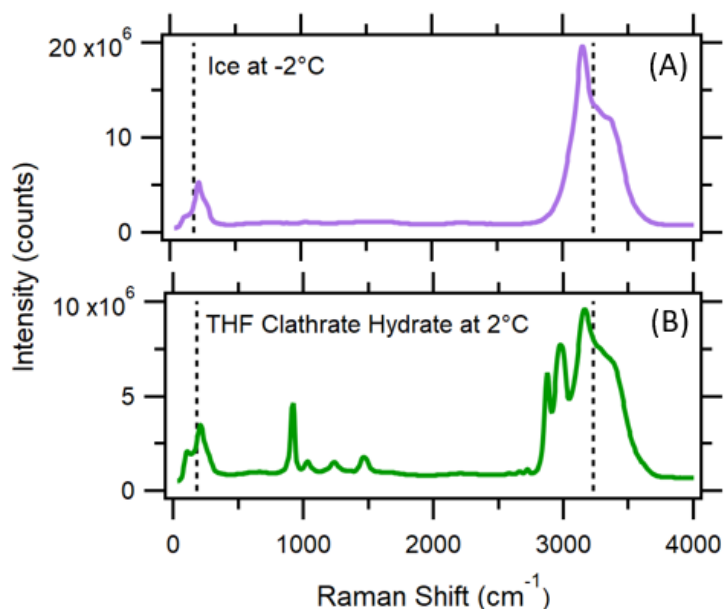


Figure 3.6 These are the Raman spectrum of (A) ice at -2°C and (B) THF clathrate hydrate (2.5 M \sim 100% CH) at 2°C .

Table 3.1 Peak positions of the low and high frequency features and frequency shift of each with respect to the peak position in the TBA hydration shell.

	ν_{200} (cm^{-1})	ν_{3200} (cm^{-1})	$\Delta\nu_{200}$ (cm^{-1})	$\Delta\nu_{3200}$ (cm^{-1})
TBA hydration shell	177.85	3229.7	---	---
THF hydration shell	180.27	3233.2	2.42	3.5
Water	186.57	3209.4	8.72	-20.3
THF clathrate hydrate	211.78	3160.7	33.93	-69.0
Ice	219.53	3149.7	41.68	-80.0

3.5 Conclusions

Raman spectra for several small amphiphilic molecules were collected and analyzed to produce hydration shell spectra with respect to temperature. As temperature decreases, two regions of the spectra, one near 200 cm^{-1} and the other near 3200 cm^{-1} , increase in intensity. By comparing these hydration shell spectra with water structure found in pure water, ice, and THF clathrate

hydrates, we provide clear experimental evidence of enhanced tetrahedral order in hydrophobic hydration-shells. Although we cannot discern whether the enhanced tetrahedral order is “clathrate-like” or “ice-like” at this time.

3.6 Supplementary Information

Figure 3.7 shows the SC spectra for nine aqueous small amphiphilic molecules (all 0.5 M except for methanol which is 1 M) in the low frequency region (100-300 cm^{-1}) of the spectra. For all nine molecules there seems to be an increase in intensity at $\sim 200 \text{ cm}^{-1}$ with decreasing temperature. The solute with the most intensity increase is *d9*-TBA, whereas tetrapropylammonium (C_3) $_4\text{N}^+$ shows very little increase in intensity. These intensity increases suggests that each of these molecules has enhanced tetrahedral water structure with respect to bulk water structure at low temperatures.

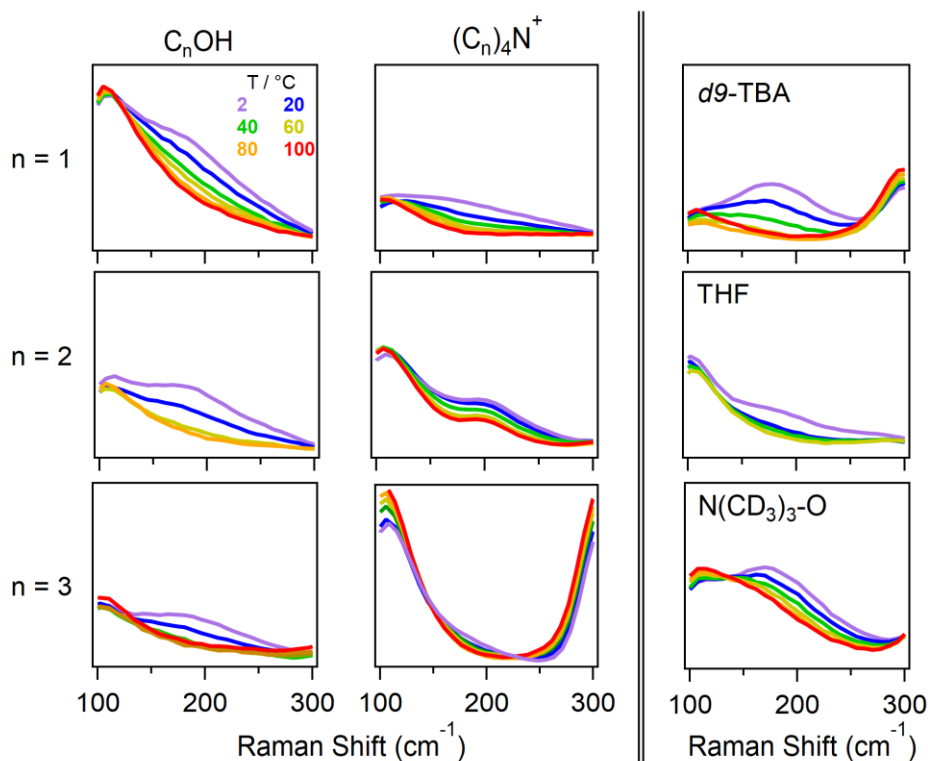


Figure 3.7 Raman SC spectra low frequency regions for nine small amphiphilic molecules. Column one, TBA, and TMAO data taken by Dr. Blake Rankin. Column two data taken by Dr. Joel Davis.

Figure 3.8 shows the SC spectra for the same nine small amphiphilic molecules in the high frequency region (3000-3750 cm^{-1}) of the spectra. For all nine molecules there is an increase in intensity at $\sim 3200 \text{ cm}^{-1}$ with decreasing temperature. The intensity ratio between $\sim 3200 \text{ cm}^{-1}$ and $\sim 3450 \text{ cm}^{-1}$ OH stretch shoulders also increases with decreasing temperature.

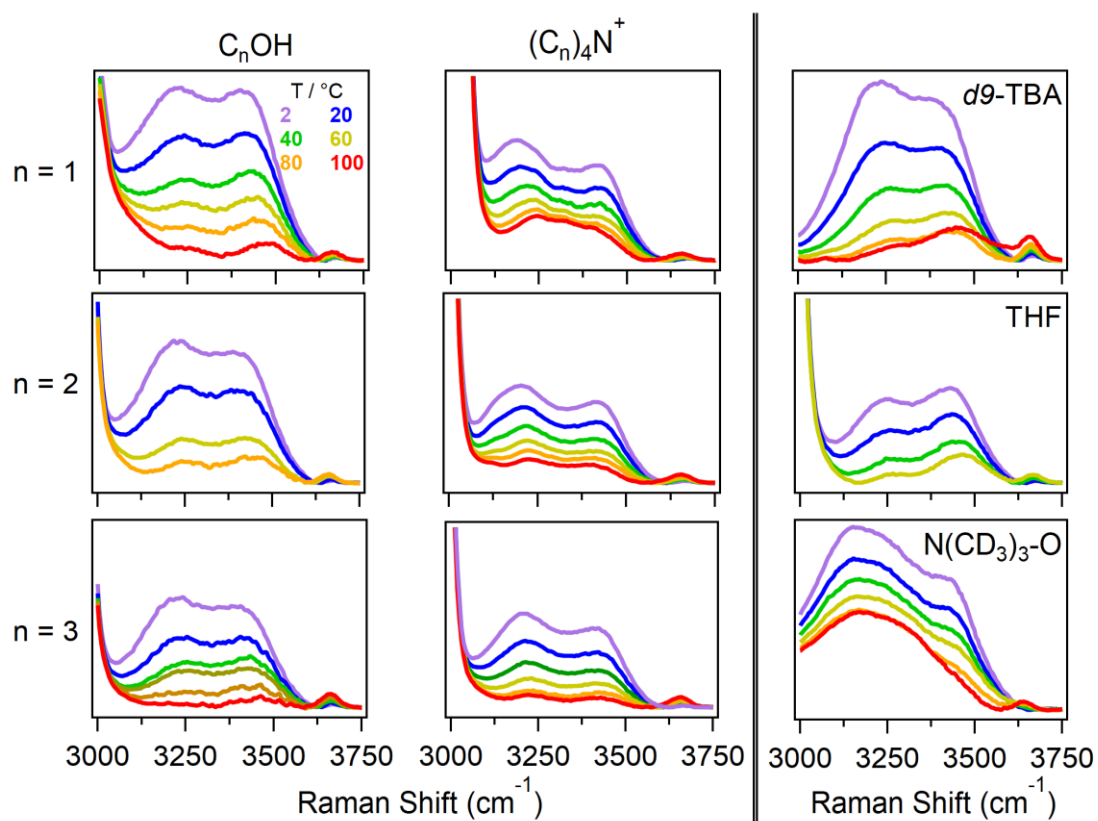


Figure 3.8 Raman SC spectra high frequency regions for nine small amphiphilic molecules.

The enhanced tetrahedral water structure in hydrophobic hydration shells is also dependent on solute concentration in addition to sample temperature. For example, Figure 3.9 shows the low and high concentration dependent hydration shell spectra of THF and TBA. As can be seen from the inset, there is no significant evidence of a 200 cm^{-1} mode in aqueous 1 M THF at 0°C and 4 M TBA at 2°C . Note that the intensity at 200 cm^{-1} is much more prominent in TBA at low concentrations than in THF. Also, this intensity is observed at higher concentrations in TBA than

in THF, which is somewhat surprising because THF is known to form clathrate hydrate compounds at these concentrations, but at lower temperature.

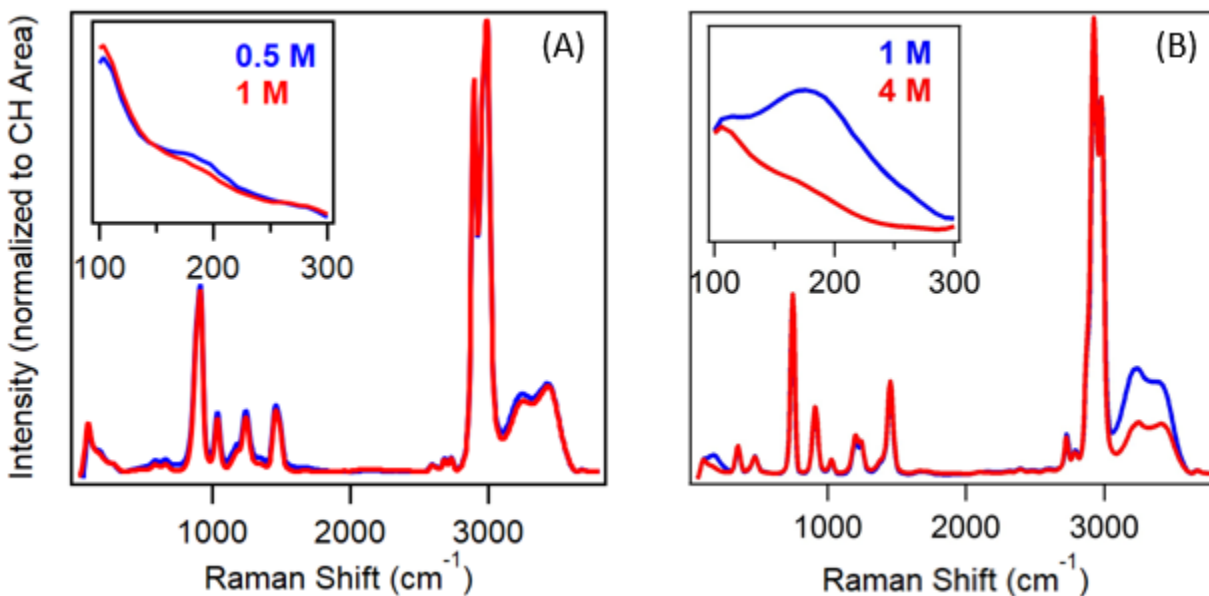


Figure 3.9 Hydration shell spectra of (A) 0.5 M and 1 M THF taken at 0°C and (B) 1 M and 4 M TBA taken at 2°C. TBA data collected by Dr. Blake Rankin.

CHAPTER 4. HYDRATION AND INTERACTION OF IONIC COMPOUNDS

4.1 Abstract

Ionic interactions are studied to determine the applicability of Raman-MCR techniques to test Collins' Law of Matching Water Affinities⁶¹ and quantify ion-pairing equilibria between cations and anions of different size, shape, charge density, and hydration free energies.⁶² Here aqueous sodium halide and alkali metal chloride salt (NaF, NaCl, NaBr, NaI, LiCl, KCl, and CsCl) solutions were investigated using Raman-MCR to characterize the ion-induced vibrational spectral changes of water molecules found in the hydration shell of ions. It is our hope that changes observed in the SC spectra may be used to quantify the effect of the ions on the structure of water and the extent of ion pairing. In an effort to do so, I have performed an initial series of concentration dependent studies to detect trends in the area and peak position of the OH stretch.

4.2 Introduction

Ionic interactions (ion-ion, ion-solvent, and ion-molecule) play an interesting role in the solubility of proteins and are essential for electrochemical processes, such as those of lithium-ion batteries.⁶³ Early observations of ionic effects were reported by Hofmeister, who characterized the so-called Hofmeister series of salts based on his studies of the ability of particular salts to solubilize or precipitate chicken egg white protein.⁶⁴ Since then, numerous simulation and experimental studies, such as MD⁶⁵⁻⁷⁰, ab initio⁶⁵, column chromatography⁷¹, neutron and X-ray diffraction⁷², Jones-Dole viscosity B coefficients⁷², dielectric spectroscopy⁷³⁻⁷⁴, THz spectroscopy⁷⁵, femto-second infrared spectroscopy⁷⁴, and Raman spectroscopy⁷⁶ have been conducted to describe the specific ionic properties (such as ion size, shape, charge density, and hydration free energy) responsible for the observed and biochemically useful trends. Additionally, Collins has established the Law of Matching Water Affinities, which describes the propensity of oppositely charge ions to form inner sphere ion pairs based on their water affinities.⁷² Therefore, it is of interest to investigate ion-ion, ion-water, and ion-molecule association and their influence on aqueous chemical aggregation processes.

Here the aqueous sodium halide and alkali metal chloride solutions (NaF, NaCl, NaBr, and NaI; LiCl, NaCl, KCl, and CsCl) are preliminarily investigated to further understand the extent of ion pairing as a function of cation to anion size ratio and charge distribution. In addition, cationic and anionic effects on the structure of water are hoped to be observed in series where the anion or cation species, respectively, is held constant. The aim of this study is to gain evidence either supporting or not supporting the trends in ion pairing consistent with Collins Law of Matching Water Affinities.^{71, 77-78}

4.3 Methods

Lithium chloride (Mallinckrodt Chemicals, 99%), sodium chloride (Mallinckrodt Chemicals, 99.0%), potassium chloride (Mallinckrodt Chemicals, 99.6%), rubidium chloride (Aldrich Chemistry, 99.8%), cesium chloride (Sigma-Aldrich, 99.9%), sodium fluoride (Sigma-Aldrich, $\geq 99\%$), sodium bromide (J.T. Baker, 99.52%), sodium iodide (Sigma-Aldrich, $\geq 99.5\%$), lithium iodide (Aldrich Chemistry, 99.9%), and cesium fluoride (Aldrich Chemistry, 99%) were used without further purification. Ultrapure filtered water (Milli-Q UF Plus, 18.2 M Ω ·cm, Millipore) was used to prepare all samples.

Each spectrum was collected for five minutes using the 514.5 nm Raman system described in Section 1.2. Duplicate aqueous solution spectra were analyzed using SMCR (Section 1.3) implemented in Igor Pro (WaveMetrics, Inc.) with pure water spectra.

4.4 Results and Discussion

4.4.1 Sodium Halide Solutions

In Figure 4.1, percent depletion of the OH area per solute molecule (SC spectra normalized by dividing each SC spectra by the corresponding molar salt concentration) was observed for all four alkali metal chloride salts with increasing concentration. The decrease in OH area is consistent with the expulsion of water to the bulk from fully hydrated ions when forming ion pairs. The least depletion is seen for NaI, and depletion is increased for NaF and NaBr, and finally the most hydration shell depletion is seen for NaCl. One possible conclusion is that the ion pairing of NaCl is the greatest among these four salts resulting in the greatest depletion of hydration shell water as

a function of salt concentration. The trend in hydration shell depletion is not easily assigned to any one trend (i.e. anion size or charge density); however, initial comparison with standard heat of solution data presented by Collins⁷² is promising.

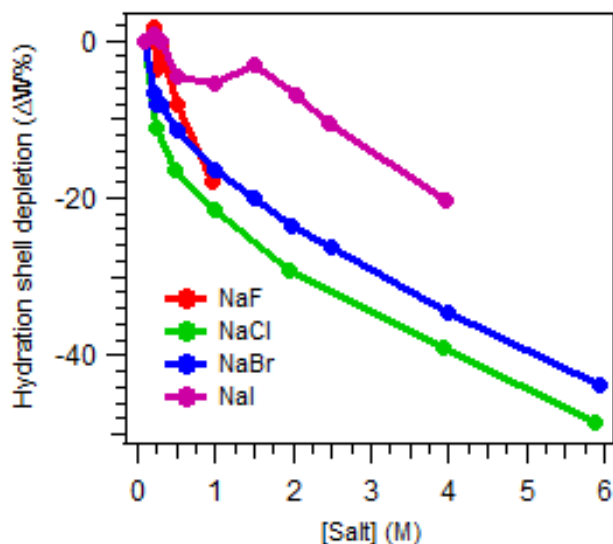


Figure 4.1 Hydration shell depletion of aqueous sodium halide salts as a function of salt concentration. The hydration shell depletion values are calculated with respect to the OH area calculation for the ~ 0.1 M SC spectra for each species.

4.4.2 Alkali Metal Chloride Solutions

In Figure 4.2A, a percent depletion (described in the Hydrophobic interactions section) in OH area per solute molecule (obtained by dividing each SC spectra by the corresponding molar salt concentration) was observed for all four alkali metal chloride salts with increasing salt concentration. The decrease is consistent with the expulsion of water to the bulk from fully hydrated ions when forming ion pairs. Also, a similar decrease in area with respect to the OH area of the lowest concentration (~ 0.1 M) was observed for NaCl and KCl; whereas, a smaller decrease was observed for LiCl, and a noisier depletion, which initially appears consistent with LiCl hydration shell depletion and becomes like NaCl and KCl depletion at higher concentrations for CsCl solutions. An initial conclusion, that needs further investigation and explanation, may be that NaCl and KCl form more ion pairs than LiCl and CsCl.

Results shown in Figure 4.2B revealed that with respect to dilute salt concentrations (~ 1 M) where there should be little or no ion-pairing, there is approximately no shift in the OH peak frequency as a function of salt concentration for LiCl, a blue shift in the OH peak frequency as a function of salt concentration for NaCl and KCl, and a red shift in the OH peak frequency as a function of salt concentration for CsCl. The red shift seen for CsCl might be indicative of water structure stabilization; whereas, the blue shifts seen for NaCl and KCl might be indicative of water destabilization by the presence of these ions in solution.

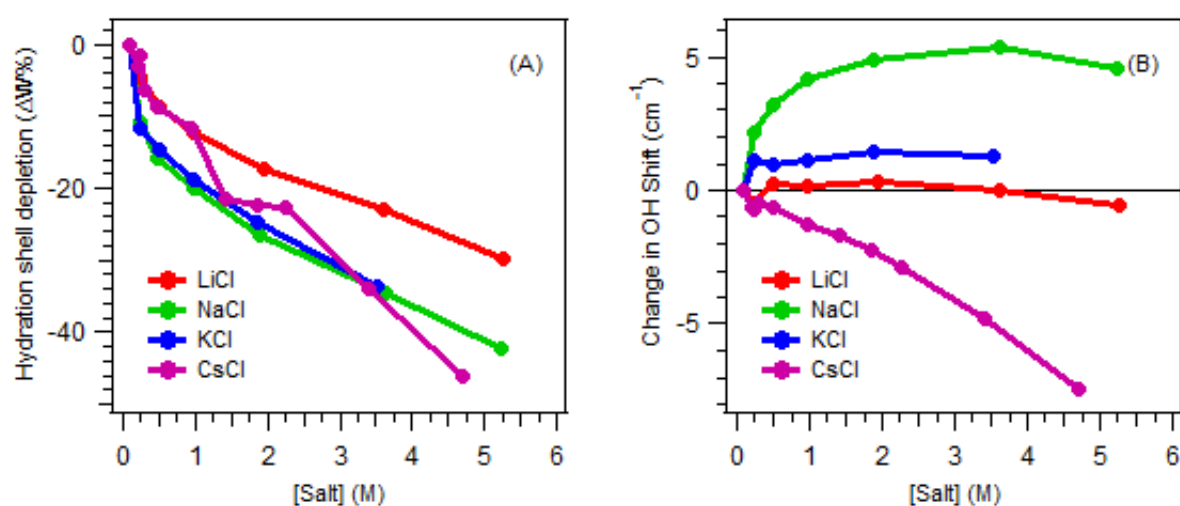


Figure 4.2 (A) Hydration shell depletion of aqueous alkali metal chloride salts as a function of salt concentration. The depletion values are calculated with respect to the OH area for the ~ 0.1 M SC spectra for each species. (B) Change in the OH Raman shift with respect to the OH Raman shift observed for the ~ 0.1 M SC spectra for each salt.

4.5 Conclusions

The ionic interactions section is currently incomplete; however, preliminary results suggest that differences in the SC spectra of different salt species and concentrations can be observed, quantified, and compared with Collins' Law of Matching Water Affinities in the near future. Future paths of investigation include application of Raman-MCR techniques to additional alkali metal halide salts, with the goal of determining a better trend in cation and anion effects on the SC spectral features (OH area and Raman shift frequencies). In addition, molecular salts such as

sulfates and nitrates could be investigated. Molecular salts would contain additional information in the Raman-MCR spectra, for example intramolecular solute vibrational features. Also, expanding the variety of salt identities and properties (size, charge distribution, etc.) studied via Raman-MCR results also makes their properties available to compare with Collins' Law. Also, MD simulations and RM predictions could lead to a better understanding of the experimental results (i.e. hydration shell water depletion values).

CHAPTER 5. HYDROPHILIC INTERACTIONS: POLARITY EFFECTS ON HYDRATION

5.1 Abstract

Hydrophilic interactions are important in aqueous solutions including processes such as self-assembly. Considering that most polar compounds are hydrophilic and highly water soluble, this chapter investigates the effects of polarity on water structure and solute aggregation. Prof. Adam Willard at MIT suggested that we look at polar molecules to study polar hydration thermodynamics. More specifically, we can study the influence of solute-water attractive interactions on water-mediated interactions using both Raman-MCR and MD simulations. Here Raman-MCR is used to assess acetonitrile (CH_3CN) and dimethyl sulfoxide (DMSO), which are two highly polar molecules with dipole moments of 3.92 D and 3.96 D respectively. In addition, preliminary MD simulations are used to calculate PMFs for two isolated acetonitrile molecules and two solvated acetonitrile molecules.

5.2 Introduction

The structural properties and thermodynamics of acetonitrile-water solutions have been extensively studied.⁷⁹⁻⁸⁰ Previous experimental, theoretical, and computational studies report contradictory conclusions regarding microheterogeneity in these solutions and enhancement of water structure by the acetonitrile molecules.^{79, 81-83} Here, Raman-MCR is used to obtain the concentration dependent hydration shell spectra of aqueous acetonitrile. These hydration shell results are compared with those of another aqueous highly polar molecule DMSO. Finally, MD simulations are implemented to obtain the contact free energies of both an isolated and aqueous pair of acetonitrile molecules from which the water-mediated contribution to the total (aqueous) contact free energy is obtained. Results suggest that acetonitrile molecules remain water-separated up to ~ 2.5 M, water effectively shields the dipolar interactions between acetonitrile molecules, and that the hydration shell water structure is more weakly hydrogen bonded than in the bulk and contains water OH groups hydrogen bonded to acetonitrile molecules.

5.3 Methods

5.3.1 Experimental

Acetonitrile (Mallinckrodt ChromAR®HPLC, 100.0%) and dimethyl sulfoxide (J.T. Baker, 0.003% water content) were used without further purification. Ultrapure filtered water (Milli-Q UF Plus, 18.2 M Ω ·cm, Millipore) was used to prepare all samples. Each spectrum was collected for five minutes using the 514.5 nm Raman system described in Section 1.2. Duplicate aqueous solution spectra were analyzed using SMCR (Section 1.3) implemented in Igor Pro (WaveMetrics, Inc.) with pure water spectra taken at the same temperature as the reference.

5.3.2 MD Simulations

A leap-frog stochastic dynamics integrator algorithm was used to perform MD simulations in GROMACS using the OPLS-AA force field for acetonitrile and TIP4P force field for water. Twenty-four, 1 ns umbrella sampling gas phase simulations (radius, r , range 0.2 nm to 1.35 nm acetonitrile separation with 0.05 nm increments) were run using two acetonitrile molecules under NVT conditions with a 1 fs time-step. Twin range cut-offs were used for both Coulombic and van der Waals interactions, and the Berendsen thermocouple was used. Additionally, 24, 10 ns aqueous phase simulations ($r = 0.2$ -1.35 nm, $\Delta r = 0.05$ nm) were run using two acetonitrile molecules and 1000 water molecules under NPT conditions with a 2 fs time-step. Fast smooth Particle-Mesh Ewald (PME) electrostatics were used for Coulombic interactions, twin range cut-offs for van der Waals interactions, and the Berendsen thermo- and pressure-couple was used.

5.4 Results and Discussion

Figure 5.1 shows the raw Raman spectra of acetonitrile solutions with concentrations between 0.1 M and 5.0 M. Additionally, the SMCR SC background-subtracted component (SCcompback) is shown in panel (B) with a close-up of the CN stretching region in panel (C). The different intensities of the CN stretching region is directly proportional to the different concentrations of the acetonitrile solutions.

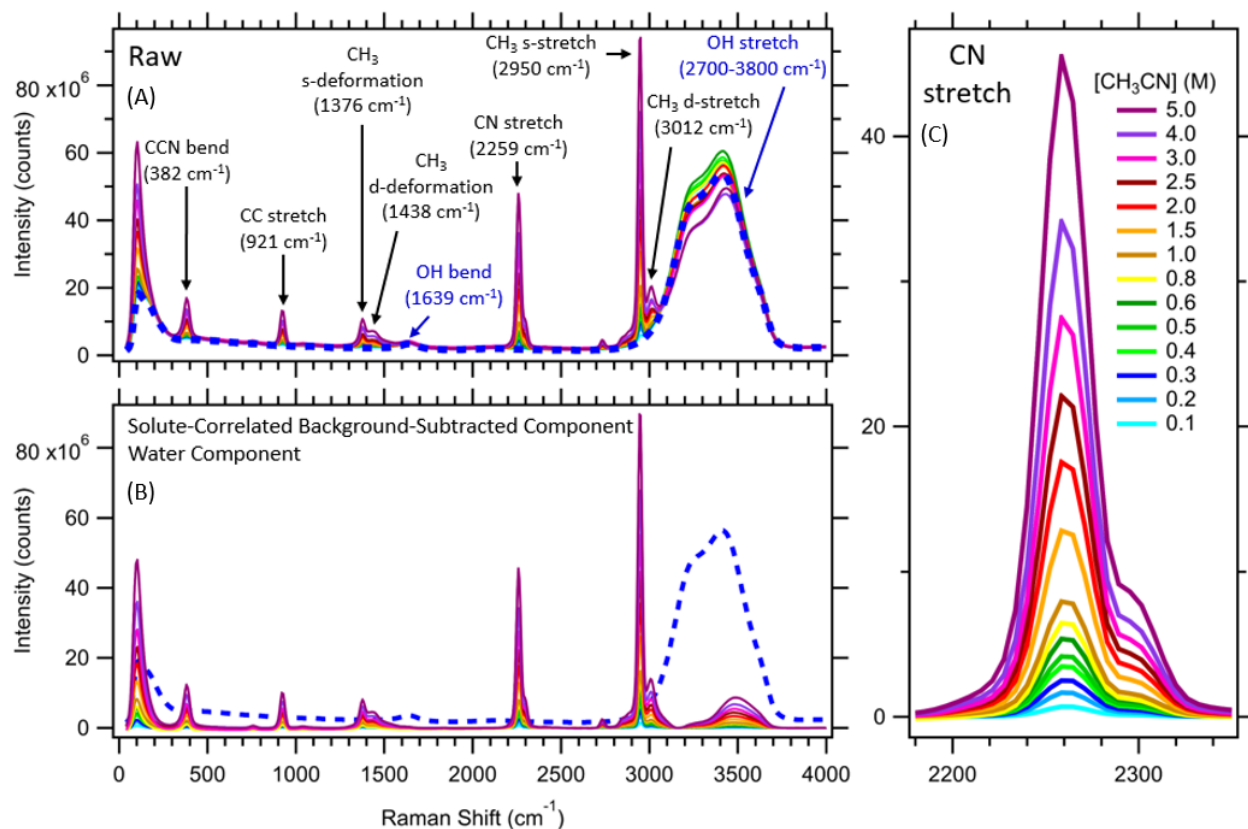


Figure 5.1 (A) Raw Raman spectra of acetonitrile solutions and pure water (dashed blue). (B) SMCR SC background-subtracted component of acetonitrile solutions. (C) CN stretching region of (B).

Shown in Figure 5.2B is the acetonitrile hydration shell normalized to the solute CH stretch band area. The hydration shell grows as the solute concentration increases, which suggests that the interaction between more than two acetonitrile molecules cooperatively enhances water structure. More specifically, as more acetonitrile is added to the solution, more water molecules per acetonitrile molecule are perturbed or the same number of water molecules per acetonitrile molecule are perturbed more. These results also indicate that water shields the dipole-dipole interactions between acetonitrile molecules causing very few direct acetonitrile contacts below ~ 2.5 M. Thus, strongly dipolar acetonitrile molecules (dipole moment, $\mu = 3.92$ D) evidently influence water structure in a qualitatively different way than other molecules, including alcohols and DMSO ($\mu = 3.96$ D) whose CH normalized hydration-shell areas invariably decrease with increasing solute concentration (Figure 5.3).

The shape of the acetonitrile hydration shell compared to pure water suggests that there is a higher ratio of weakly hydrogen bonded OH groups to strongly bonded OH groups in the hydration shell of acetonitrile. More specifically, the ratio between the intensity at $\sim 3310\text{-}3550\text{ cm}^{-1}$ (weakly hydrogen bonded OH groups) to the intensity at $\sim 3150\text{-}3310\text{ cm}^{-1}$ (strongly hydrogen bonded OH groups) is larger in the acetonitrile hydration shell than in pure water. Also, the acetonitrile hydration shell shows significant signal above 3600 cm^{-1} , which may represent water OH groups that are hydrogen bonded to acetonitrile molecules. This assignment is supported by previous results for aqueous ethanol, carbon dioxide, and benzene (Figure 7.3) that reveal dangling OH groups, weakly hydrogen bonded groups to CO_2 , and π -hydrogen bonded OH groups at $\sim 3667\text{ cm}^{-1}$, $\sim 3654\text{ cm}^{-1}$, and $\sim 3610\text{ cm}^{-1}$ respectively.⁸⁴

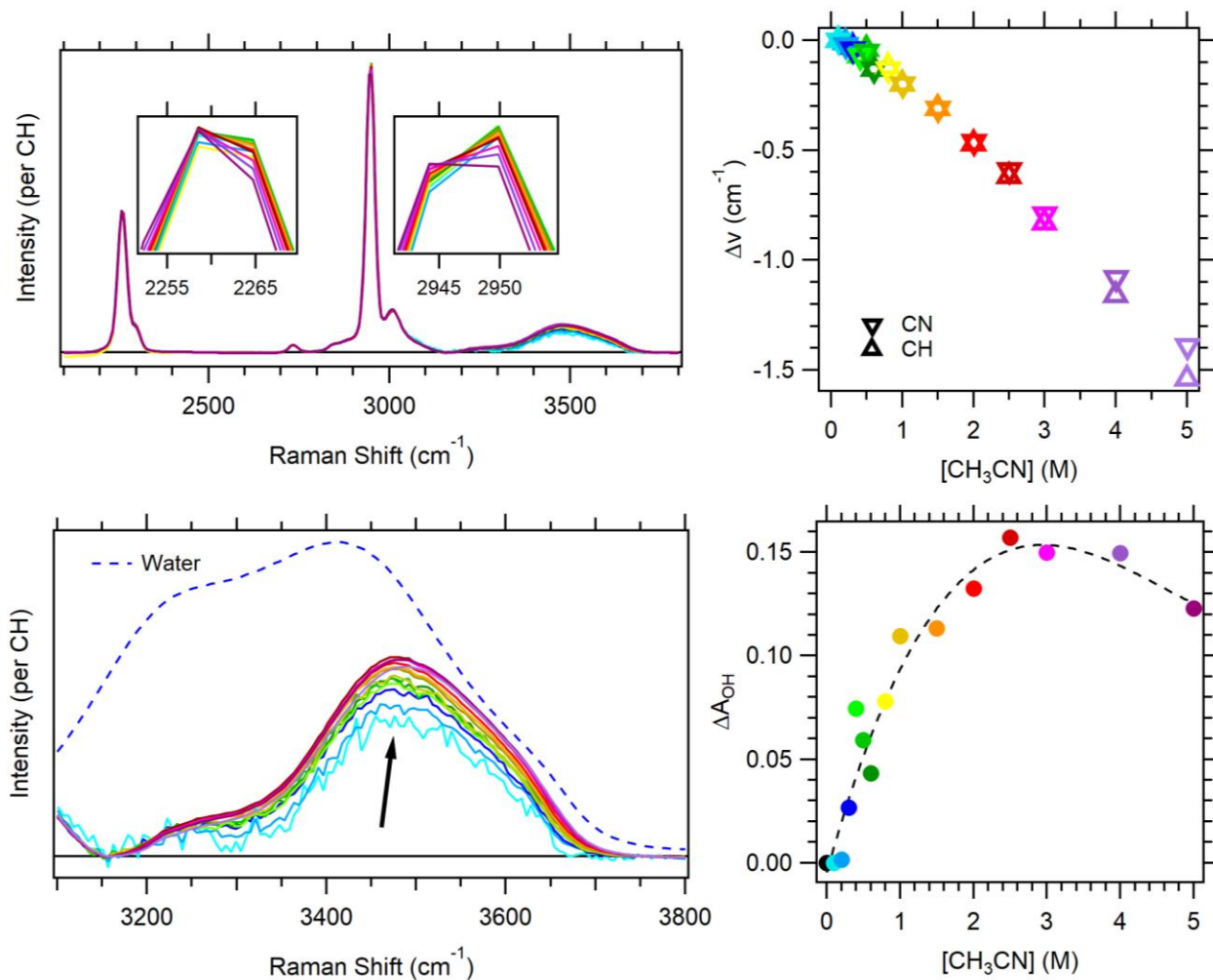


Figure 5.2 Acetonitrile (A) spectrum with CN stretch (left inset), CH stretch (right inset), and OH stretch. (B) CN and CH stretch change in frequency with respect to acetonitrile concentration (C) Hydration-shell dependence on acetonitrile concentration normalized per CH group. (D) Change in the OH area (ΔA_{OH}) of the hydration-shell with respect to acetonitrile concentration.

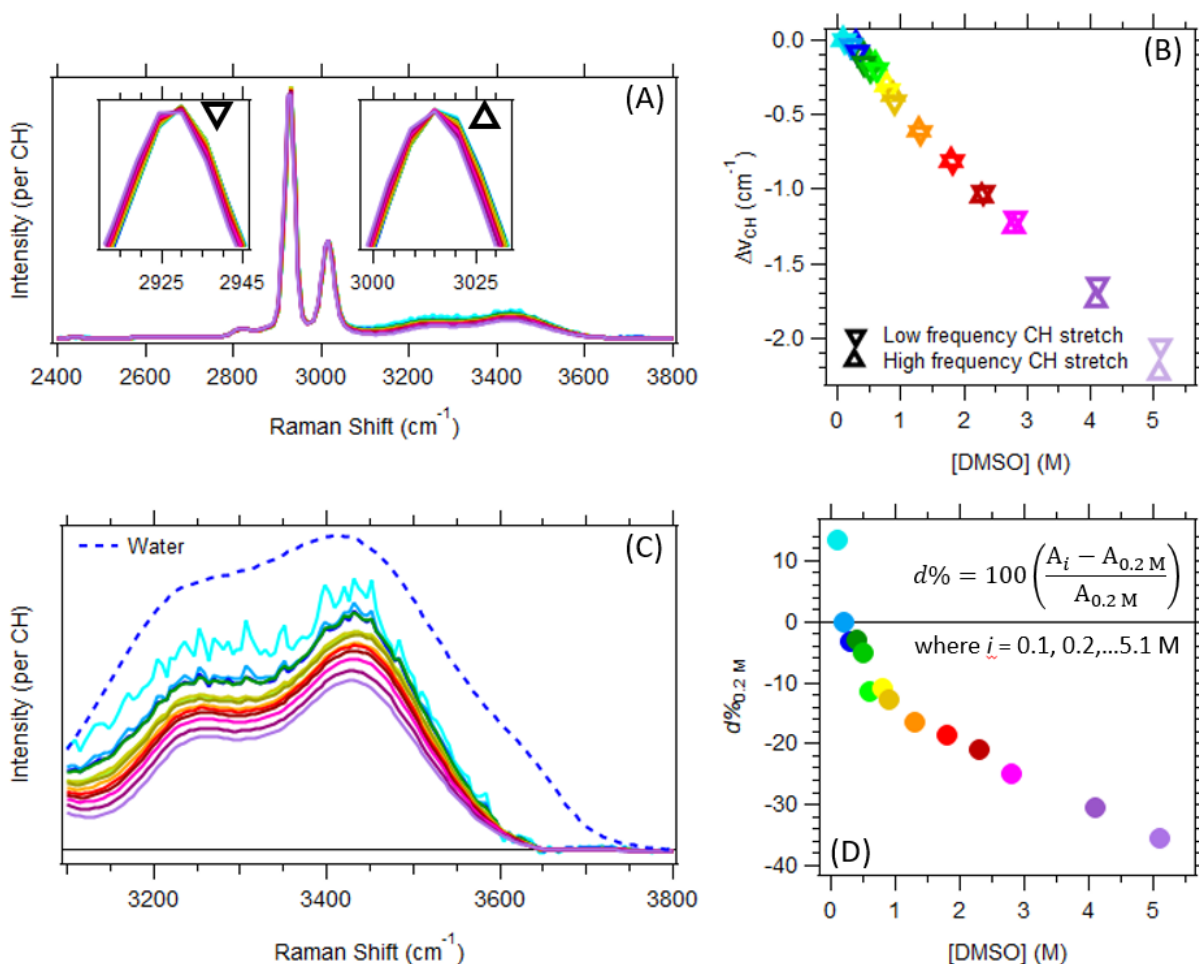


Figure 5.3 DMSO (A) spectrum of CH stretch and OH stretch. Insets are the low (left) and high (right) frequency CH stretch peaks. (B) Low and high frequency CH stretch frequency shifts with respect to DMSO concentration. (C) Hydration shell per CH of DMSO. (D) Depletion percentage of the hydration shell with respect to DMSO concentration.

Furthermore, the Raman-MCR results are supported by preliminary MD simulations that calculate the potential of mean force (PMF) between two acetonitrile molecules in water and in vacuum (shown in Figure 5.4B). The difference between the latter two PMFs is a measure of the water-mediated interaction free energy (Equation 2.3), which was found to be substantially repulsive at +11.2 kJ/mol. On the other hand, the interaction energy between solvated acetonitrile molecules was very weakly attractive at -1.0 kJ/mol, which is less than RT . These two energy values indicate that water molecules are driving the aqueous acetonitrile molecules apart such that the acetonitrile molecules are barely (if at all) attracted to each other, unlike their direct interaction

energy indicates for an isolated pair of acetonitrile molecules. This, combined with our spectroscopic results, implies that the water-mediated repulsion is associated with enhanced ordering of water between neighboring acetonitrile molecules.

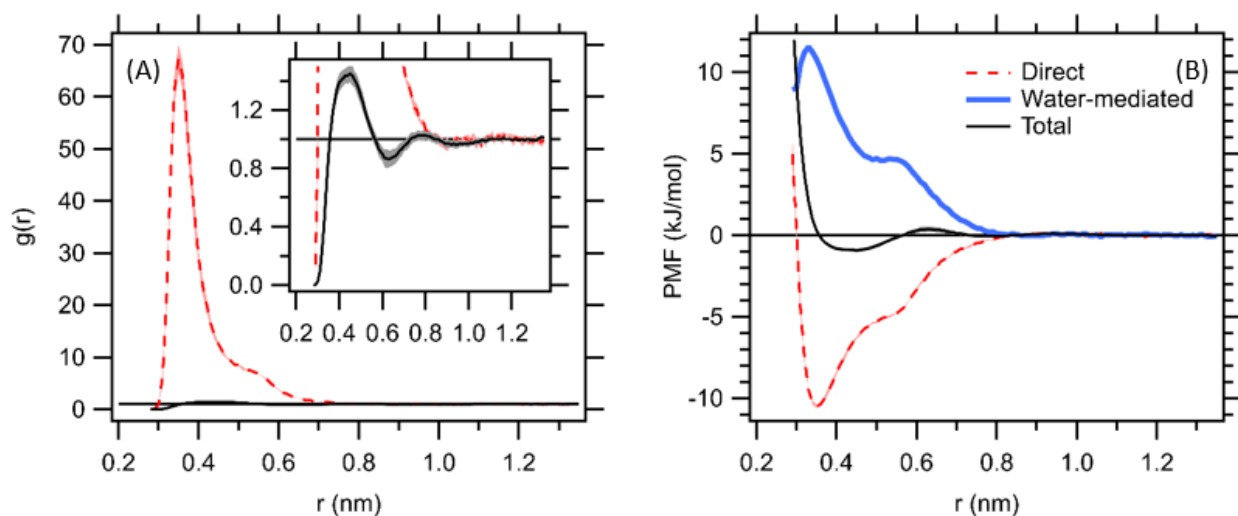


Figure 5.4 (A) Acetonitrile-acetonitrile radial distribution functions shown for the gas phase (red) and solution phase (black). Shaded region indicates error. (B) PMF between acetonitrile molecules in the gas phase, solution phase, and water-mediated contribution to the total solution phase interaction.

Finally, Figure 5.5 shows the hydration-shell temperature dependence of a 1.0 M acetonitrile solution. Interestingly, the OH intensity increases from 0°C to 80°C. Previous work has only shown increases in the hydration shell over 0°C to 100°C of ≤ 0.5 M amphiphilic solute molecules that are sufficiently large (~ 1 nm; n-butanol and larger).³ Acetonitrile is much smaller than n-butanol, so it is surprising that such behavior exists for acetonitrile based on its size.

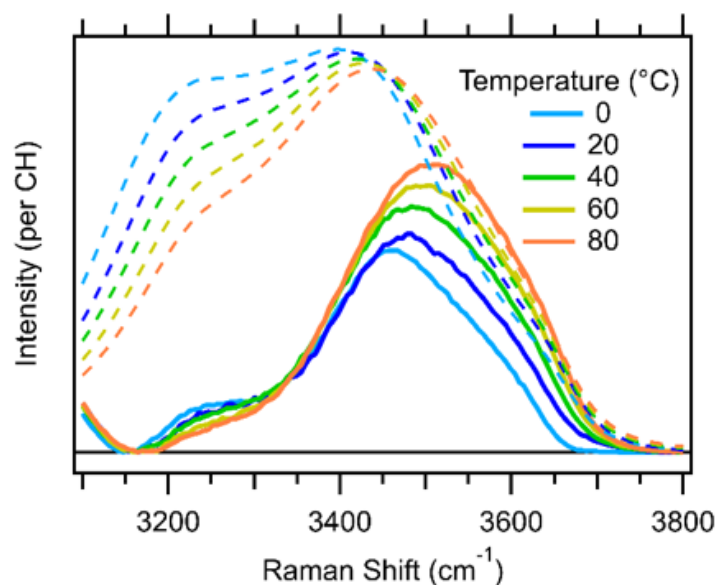


Figure 5.5 Hydration-shell temperature dependence for 1.0 M acetonitrile solution. Pure water (dashed) temperature dependence shown for reference.

5.5 Conclusions

The hydration shell of the highly polar molecules acetonitrile and DMSO were investigated with respect to solute concentration. Qualitatively, the hydration shell of DMSO is like that of hydrophobic solutes (e.g. TBA), whereas the hydration shell of acetonitrile is different than that of hydrophobic solutes. The increase in the hydration shell of acetonitrile along with preliminary MD simulation PMFs indicate that water molecules effectively shield the interactions between acetonitrile molecules such that very few acetonitrile molecules are in direct contact below ~ 2.5 M. More experiments and simulations can be done, including the use of other highly polar solute molecules (N-methylpyrrolidone, nitromethane, etc.) and collaborative efforts with the simulation research group of Professor Adam Willard at MIT.

CHAPTER 6. CHARGE EFFECTS ON HYDRATION AND AGGREGATION

6.1 Introduction

Charged molecular species and domains influence the solubility and molecular interactions in water, of importance to biology, surface science, and detergents. Some examples include enzyme-substrate complexes, protein channels, self-assembly processes, stern layer formation, and micelle formation. Here, charged solute effects are studied using *tert*-butanol (neutral) and its charged analogues sodium trimethylacetate (negative) and *tert*-butylammonium (positive) chloride to quantify the influence of charge on the aggregation and hydration shell structure of amphiphilic solutes. In addition, by comparing the results among neutral, positive, and negative charged solutes with head-group subtraction we will better understand the applicability and reach of head-group subtraction methods for other systems.

Recall from Section 1.3.1 that head-group subtraction is used to prevent spectral features related to specified solute functional groups (e.g. amine, carboxylic acid) from appearing in SMCR solute-correlated spectra. For example, instead of using pure water as the solvent component when applying SMCR to a solution spectrum of sodium trimethylacetate, an equimolar sodium formate solution can be used as the solvent component to account for signal arising from solute sodium carboxylate head-groups and their interactions with water and other solute sodium carboxylate head groups. Under the assumption that the sodium formate solution closely represents the sodium carboxylate head-group and its interactions in the sodium trimethylacetate solution, the resulting solute-correlated spectrum contains only water and solute features primarily affected and caused by the hydrophobic *tert*-butyl group of sodium trimethylacetate.

6.2 Methods

Tert-butyl alcohol (Sigma-Aldrich, $\geq 99.7\%$), sodium trimethylacetate (Aldrich, 99%), sodium formate (Sigma-Aldrich, $\geq 99.0\%$), *tert*-butylamine hydrochloride (Sigma-Aldrich, $\geq 98.0\%$), and ammonium chloride (Aldrich Chemistry, 99.99%) were used without further purification. Ultrapure filtered water (Milli-Q UF Plus, 18.2 M Ω ·cm, Millipore) was used to prepare volumetric 1 M aqueous solutions for all solutes. Using the 1 M stock solution, 0.8, 0.6,

0.4, and 0.2 M solutions were prepared by serial dilution. Each spectrum was collected at 20°C for five minutes using the 514.5 nm Raman system described in Section 1.2. Duplicate aqueous solution spectra were analyzed using SMCR (Section 1.3) implemented in Igor Pro (WaveMetrics, Inc.) with either pure water spectra or equimolar head-group solutions taken at the same temperature as the reference. The process of head-group subtraction implemented in SMCR is described in Section 1.3.1.

6.3 Results and Discussion

Figure 6.1 shows the raw Raman spectra for *tert*-butanol (TBA), sodium trimethylacetate (NaTMA_t), sodium formate (NaF_t), *tert*-butylammonium chloride (TBAmCl), and ammonium chloride (AmCl). The molecular structure of the solutes as well as those of the molecule used as the reference for SMCR head-group subtraction are also shown in Figure 6.1. The NaTMA_t solutions had a large fluorescent background as shown in Figure 6.1B, however, this background did not significantly affect the SMCR analysis of these solutions because the region of interest was ~2400 cm⁻¹ to 4000 cm⁻¹ where there is much less background signal.

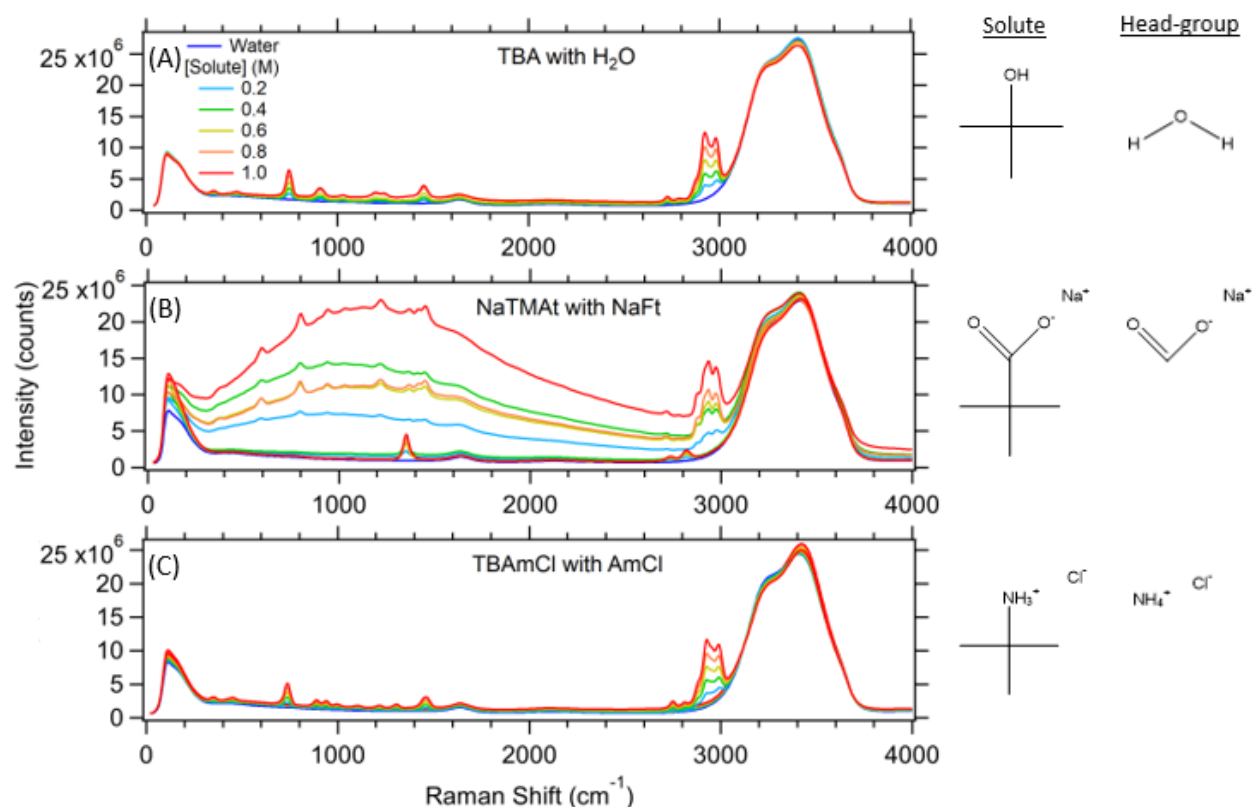


Figure 6.1 Raman spectra for (A) aqueous *tert*-butanol and water, (B) aqueous sodium trimethylacetate, aqueous sodium formate, and water; (C) aqueous *tert*-butylammonium chloride, aqueous ammonium chloride, and water. The right-side panel shows the structure of the solute and the structure of the head-group used in equimolar amounts for the SMCR reference solution.

The hydration shell spectra (normalized to CH stretch area) for TBA, TMAc, and TBAm are shown in Figure 6.2A-C. The TMAc and TBAm hydration shell spectra were obtained via head-group subtraction with equimolar solutions of NaFt and AmCl respectively. Pure water was used as the reference solution to obtain the TBA hydration shell spectra. At first glance the hydration shell for each of the three molecules is similar, but important differences are present. For example, each hydration shell has a slightly different shape of the hydrogen bonded OH region (3100-3600 cm^{-1}) and dangling OH ($\sim 3670 \text{ cm}^{-1}$) intensity also shown in Figure 6.3. TBAm has two distinct intensity regions in the hydrogen bonded OH region: one at $\sim 3200 \text{ cm}^{-1}$ and the other at $\sim 3450 \text{ cm}^{-1}$. TBA also has two shoulders in this region although less distinct than TBAm. However, TMAc does not have two distinct intensity regions instead the intensity at $\sim 3200 \text{ cm}^{-1}$ monotonically decreases to the intensity found at $\sim 3450 \text{ cm}^{-1}$. The high frequency edge of the hydrogen bonded

OH region and the dangling OH peak is also significantly red-shifted ($\sim 13 \text{ cm}^{-1}$) in TMAc with respect to both TBA and TBAm. Also, the dangling OH intensity is noticeably smaller in TBA and TBAm than it is in TMAc.

These differences in the hydration shell spectra of TBA, TMAc, and TBAm provide valuable information about how differently charged head-groups affect the self-interaction of the solute molecules and their interaction with water. The *tert*-butyl oily group present in these molecules is quite small, and therefore it is not surprising that differences in the head-group attached to the *tert*-butyl group affect the shape and intensity of each hydration shell. However, it is surprising that according to the hydration shell depletion and CH stretch frequency shifts shown in Figure 6.2D-F that TMAc, which has a negatively charged head-group, shows the most hydration shell depletion and CH stretch frequency shifts from 0.2 M to 1.0 M solutions. These results suggest that the TMAc oily *tert*-butyl group aggregates more so than TBAm and even more so than TBA.

On the other hand, these differences provide insight into the assumptions made when performing SMCR head-group subtraction. One of the past uses of head-group subtraction is to account for contributions from a head-group attached to a long oily chain necessary to achieve solute solubility within the detection limits of the Raman instrument when only interested in the hydration of the long oily chain (not the head-group).⁸⁵ With this use of head-group subtraction, one assumption is that the resulting hydration shell spectra are representative of only the oily chain, which on its own is not soluble enough to study with Raman-MCR. The results shown in this chapter are consistent with those reported by Davis, et al.⁸⁵ and suggest that the hydration shell of the oily *tert*-butyl group of the TBA analogues differs from neutral to negatively to positively charged head-group containing solutes. However, these three molecules studied here are quite small and as stated previously it is not surprising that the hydration shells are noticeably affected by the different head-groups. It might be expected that this effect is much less effective in long chain oily molecules where the head-group is further removed and much smaller than the oily tail, but similar changes in hydration shell shape with respect to solute charge among carboxylic acids, carboxylates, and tetraalkylammonium solutes has been observed.⁸⁵

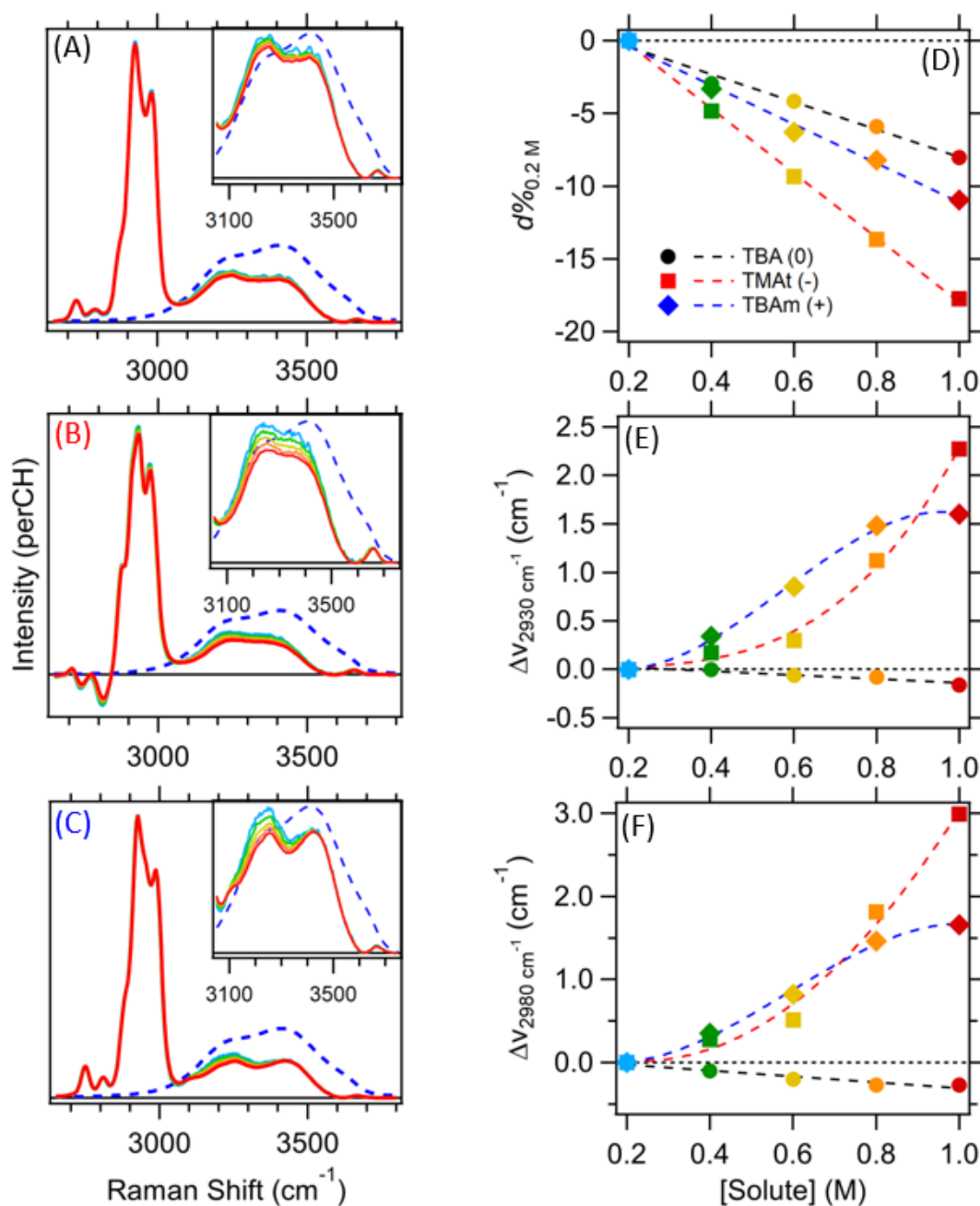


Figure 6.2 Hydration shell spectra for (A) TBA, (B) TMAc, and (C) TBAm. For (A), (B), and (C) the dashed blue spectrum is pure water. (D) Hydration shell depletion percentage for TBA, TMAc, and TBAm. Dashed lines are linear fits to the data. Frequency shifts with respect to concentration for the (E) low ($\sim 2930 \text{ cm}^{-1}$) and (F) high ($\sim 2980 \text{ cm}^{-1}$) frequency prominent CH-stretch modes. Black dashed lines are linear fits to the data. Red and blue dashed lines are fourth-order polynomial fits to the data.

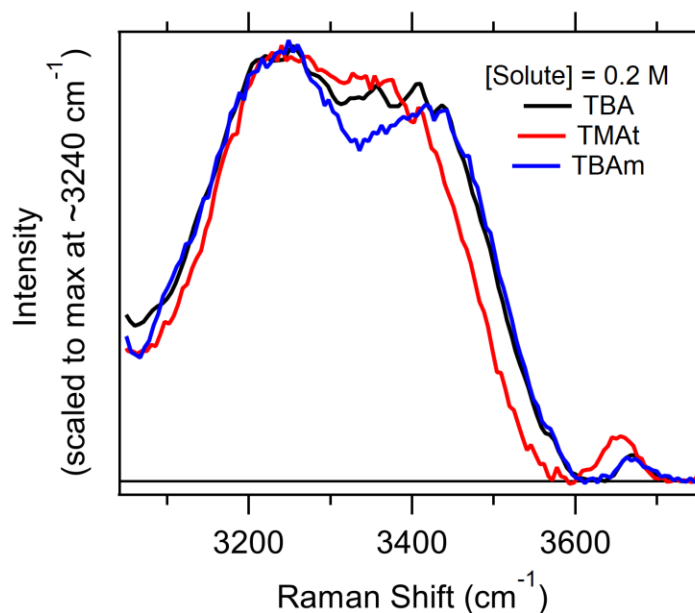


Figure 6.3 Hydration shell spectra OH stretch region for dilute (0.2 M) TBA, TMAc, and TBAm.

6.4 Conclusions

The hydration and aggregation of TBA (neutral), TMAc (negative), and TBAm (positive) molecules was investigated using Raman-MCR techniques. It is shown that even though SMCR head-group subtraction has been used to extract the hydration shell of the *tert*-butyl group for TMAc and TBAm, the hydration and aggregation of these *tert*-butyl groups is affected by the different charges found in TBA, TMAc, and TBAm. Surprisingly, it is also found that the negatively charged head group of TMAc causes the oily *tert*-butyl groups to aggregate more than those of the positively charged TBAm molecules and the neutral TBA molecules.

CHAPTER 7. INTRAMOLECULAR DEPENDENT HYDRATION SHELL SPECTRA OF BENZENEDIOLS

7.1 Abstract

Professor A. Ben-Naim has previously analyzed experimental solvation energies of xylene and benzenediol isomers resulting in quantitative and qualitative differences between the water-mediated energies of methyl and hydroxyl substituents associated with moving the groups between the *para*, *meta*, and *ortho* positions.⁸⁶⁻⁸⁷ Inspired by Ben-Naim's work, here the solutes *o*-benzenediol (catechol), *m*-benzenediol (resorcinol), and *p*-benzenediol (hydroquinone) are studied to observe changes in Raman -OH features as a function of the different hydroxyl positions on benzenediol.

7.2 Introduction

Over the past 50 years, several models have been created to describe the hydrophobic effect that is the affinity for nonpolar solutes to aggregate in aqueous solution.^{6, 86} More specifically, these models try to pinpoint energetic and entropic processes that result in the overall negative contact free energy of oily solutes in water. The original goal for these models was the ability to predict the contribution of hydrophobic interactions (solute-solute and solute-solvent) in protein folding and unfolding. One such model proposed by Prof. Arieh Ben-Naim describes monitoring the free energy of two non-polar solutes attached to a backbone originally at infinite distance being brought close together in water, which would result in the total contact free energy of the solvated solutes.⁸⁶⁻⁸⁸ Experimentally, the water-mediated contribution to the total contact free energy of methyl side groups can be approximated by considering the difference between the solvation free energies of *p*-xylene and *o*-xylene. In this case, it is assumed that *p*-xylene has two "infinitely" separated methyl groups and the *o*-xylene has negligibly separated methyl groups.

Similarly, the water-mediated contribution to the total contact free energy of different side groups could be obtained. For example, using hydration shell spectroscopy to investigate the water structure around benzenediols with different hydroxyl positions should reveal any differences caused by the *ortho*-, *meta*-, and *para*- hydroxyl groups. More specifically, special bridging water molecules between the hydroxyl groups may be observed in the concentration dependent hydration

shell of these benzenediol solutes when compared with hydration shell spectra of benzene and phenol. Any significant changes in the concentration dependent hydration shell spectra of these benzenediol solutes might suggest

7.3 Methods

Benzene (OmniSolv, 99.98%), phenol (Sigma-Aldrich, 99+%), hydroquinone (Oakwood Chemical), resorcinol (Oakwood Chemical), and catechol (Oakwood Chemical) were used without further purification. Ultrapure filtered water (Milli-Q UF Plus, 18.2 M Ω ·cm, Millipore) was used to prepare all samples. Benzene, phenol, and hydroquinone solution concentrations were limited by the solubility of the solute: ~0.2 M, 0.7 M, and 0.9 M respectively. Each spectrum was collected for five minutes at 20°C using the 514.5 nm Raman system described in Section 1.2. Duplicate aqueous solution spectra were analyzed using SMCR (Section 1.3) implemented in Igor Pro (WaveMetrics, Inc.) with pure water spectra as the reference.

7.4 Results and Discussion

Upon visual inspection of the aqueous solutions it was found that benzene and phenol solutions were clear and colorless, however, catechol was initially a clear, light peach-orange color that became darker over a few hours; resorcinol was initially clear and colorless, but over the course of about a week the solution turned a clear, light yellow color; and hydroquinone was initially clear and colorless, but over a few hours turned to a light brown-orange that became darker over about a week. The phenol and three benzenediol solutions showed broad fluorescent backgrounds shown in Figure 7.1.

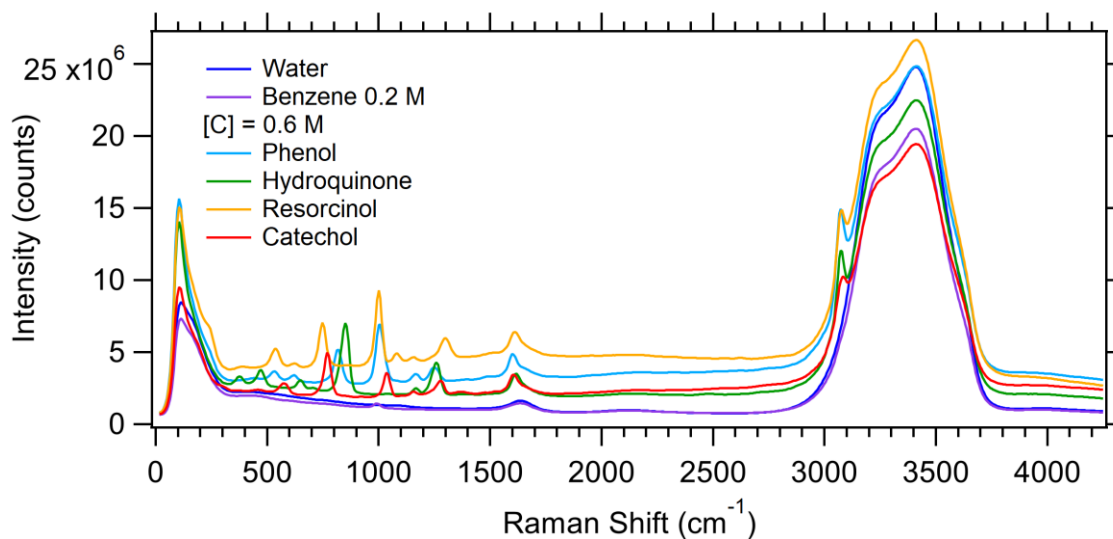


Figure 7.1 Raman spectra for water, benzene, phenol, hydroquinone, resorcinol, and catechol.

The concentration dependent SMCR hydration spectra results for benzene, phenol, hydroquinone, resorcinol, and catechol are shown in Figure 7.2. Surprisingly, all five molecules have similar shapes and intensities of the OH stretch in their hydration shells. Like benzene, each molecule has a prominent π -hydrogen bond peak at $\sim 3600 \text{ cm}^{-1}$ because of the benzene ring present in all five molecules. Also, even though there seems to be slightly more OH intensity in the three benzenediol molecules than phenol, the shapes are very similar among these four molecules. Finally, the depletion seen among phenol and the three benzenediol molecules is remarkably the same in that there is little to no depletion over the concentration ranges studied.

Figure 7.3 shows the hydration shell spectra normalized per solute for 0.2 M benzene and equimolar 0.6 M phenol, hydroquinone, resorcinol, and catechol. The normalization of these spectra was performed by considering the number of CH groups on each of the molecules. From these spectra, two small, but noteworthy differences are apparent. The first is that the hydration shell is more intense starting from benzene to phenol and then the benzenediol molecules in order of increasing polarity: hydroquinone, resorcinol, and then catechol. In the same order, the π -hydrogen bond peak red-shifts $\sim 20 \text{ cm}^{-1}$ from $\sim 3608 \text{ cm}^{-1}$ in benzene to $\sim 3588 \text{ cm}^{-1}$ in catechol. This intensity increase and red-shift implies that there are more π -hydrogen bonds that are on average the strongest for catechol when compared with the other four solutes.

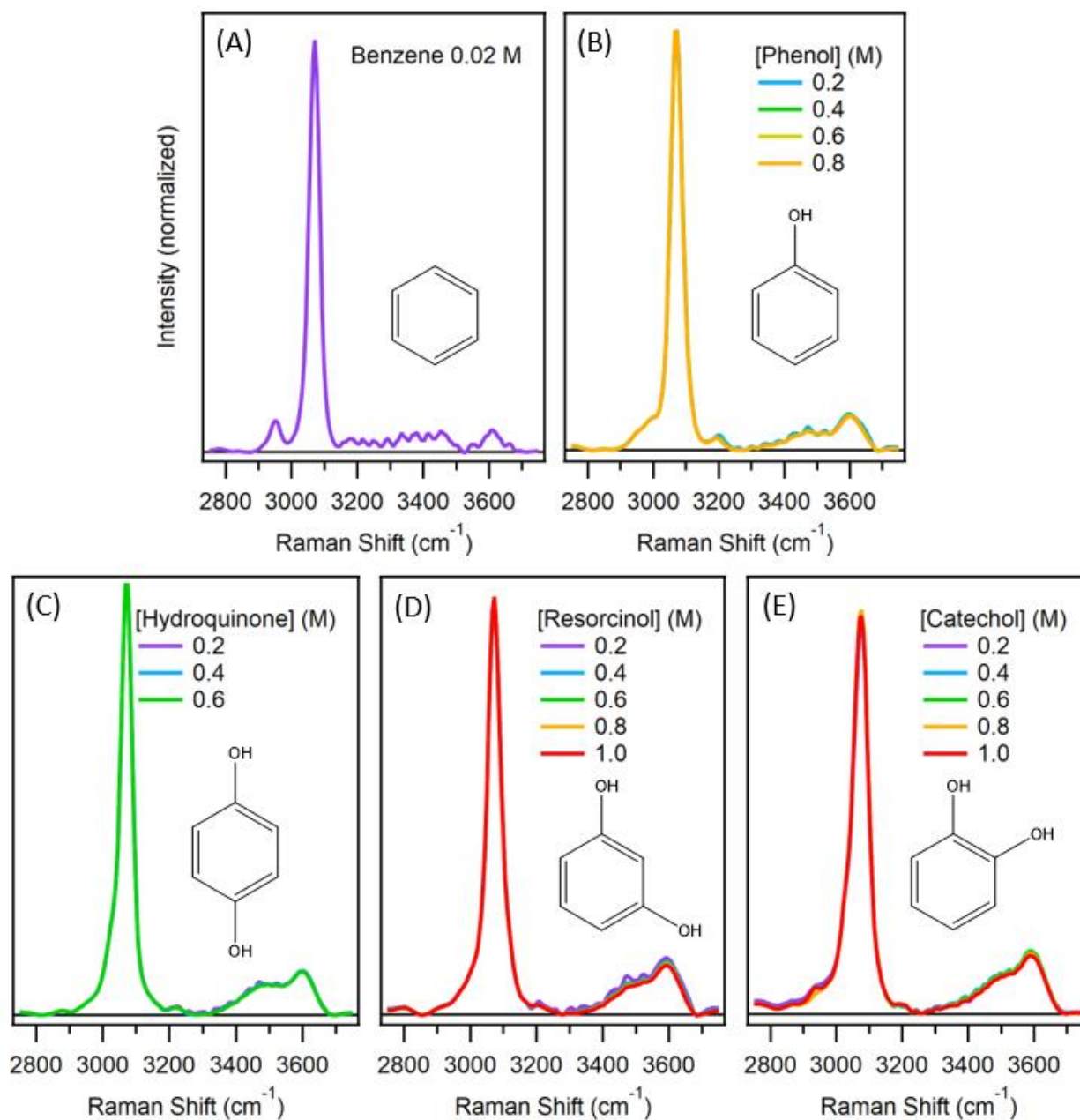


Figure 7.2 Hydration shell spectra normalized to CH stretch intensity for (A) benzene, (B) phenol, (C) hydroquinone, (D) resorcinol, and (E) catechol.

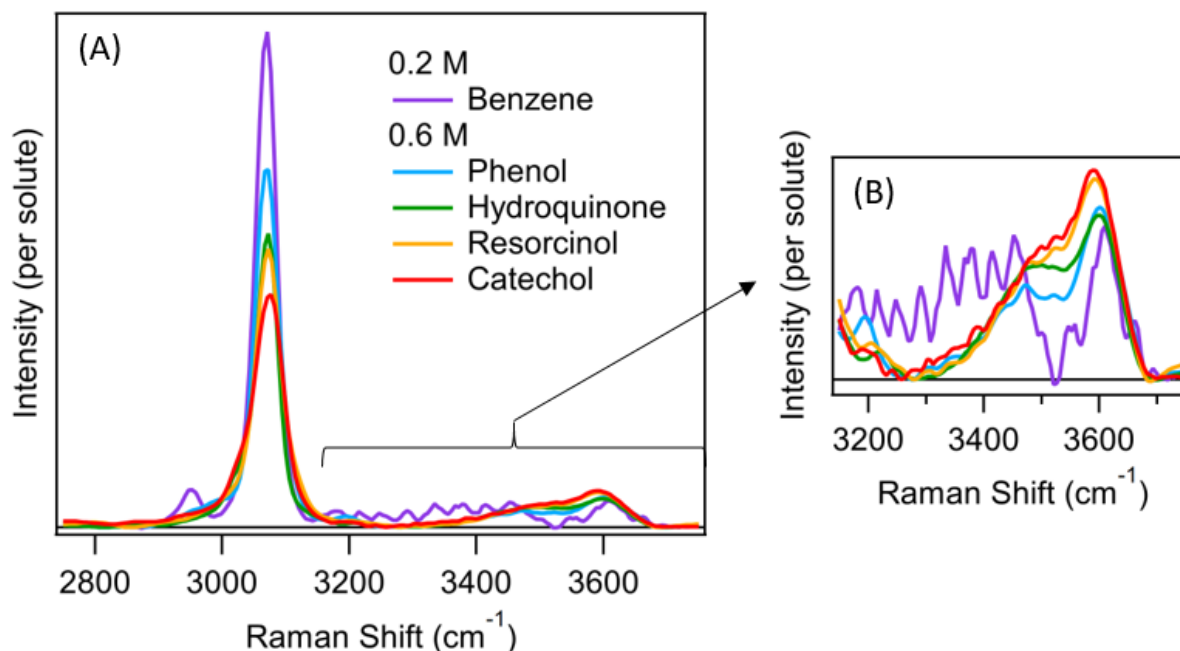


Figure 7.3 Hydration shell spectra for equimolar solutions of phenol, hydroquinone, resorcinol, and catechol. Benzene at 0.2 M is also shown. Spectra are normalized per solute.

7.5 Conclusions

Raman spectra were collected for aqueous solutions of benzene, phenol, hydroquinone, resorcinol, and catechol. Raman-MCR was used to analyze these spectra to produce hydration shell spectra. Unfortunately, very few differences were observed among the hydration shells of these molecules. There was some evidence (hydration shell intensity and position of the π -hydrogen bond peak) that catechol contains more and stronger π -hydrogen bonds than resorcinol and then hydroquinone. However, there is no other evidence for any distinguishing hydration shell features based on the position of hydroxyl groups in the three benzenediol solutes.

APPENDIX A. ADDITIONAL 2-BUTOXYETHANOL DATA

The temperature dependent hydration shell spectra and hydration shell depletion of BE are reported in this Appendix. Also, the concentration dependent BE hydration shell spectra collected with the 1200 grooves/mm monochromator grating with a resolution of $\sim 1 \text{ cm}^{-1}/\text{pixel}$ are shown.

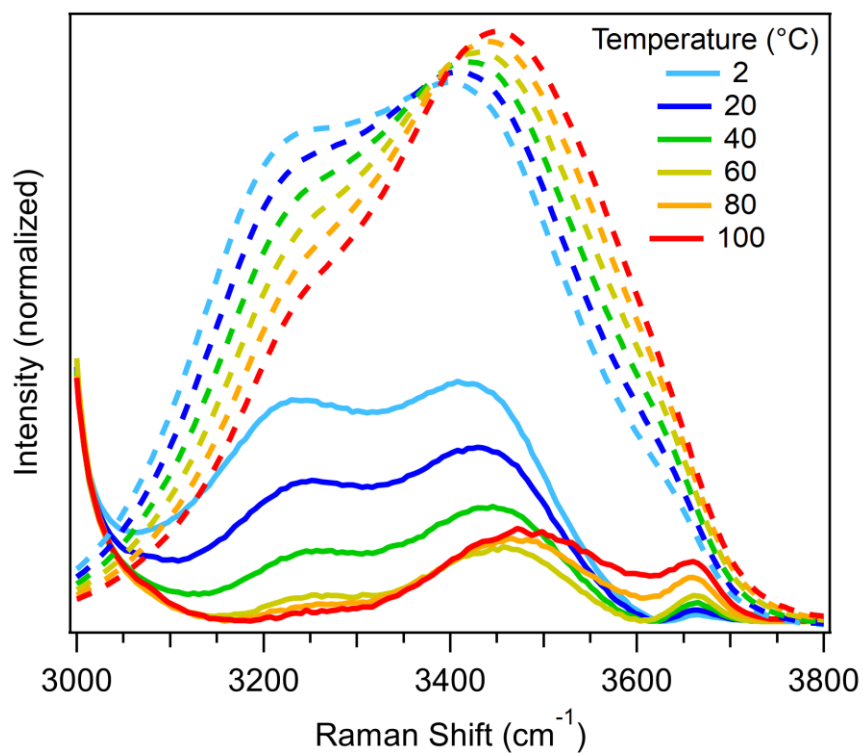


Figure A.1 Temperature dependent hydration shell spectra for aqueous 0.5 M BE.

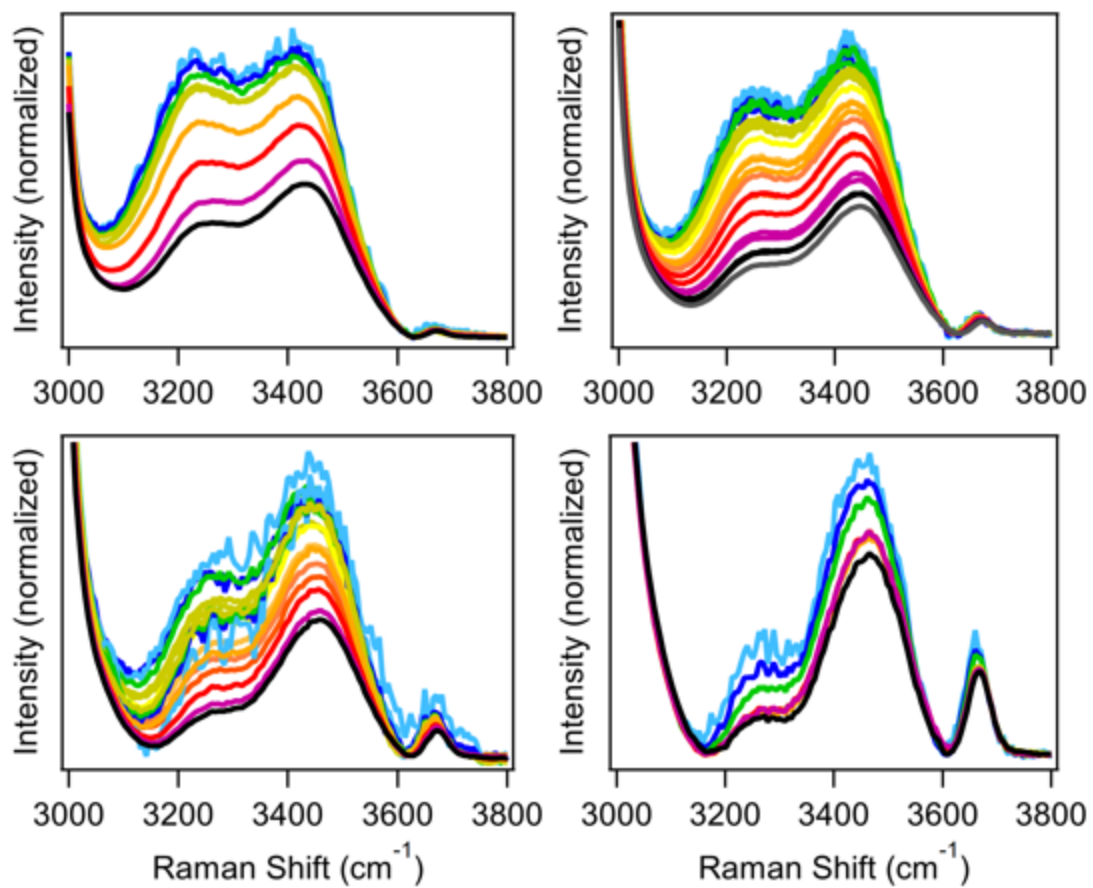


Figure A.2 Concentration dependent hydration shell spectra for BE at (A) 2°C, (B) 20°C, (C) 40°C, and (D) 60°C.

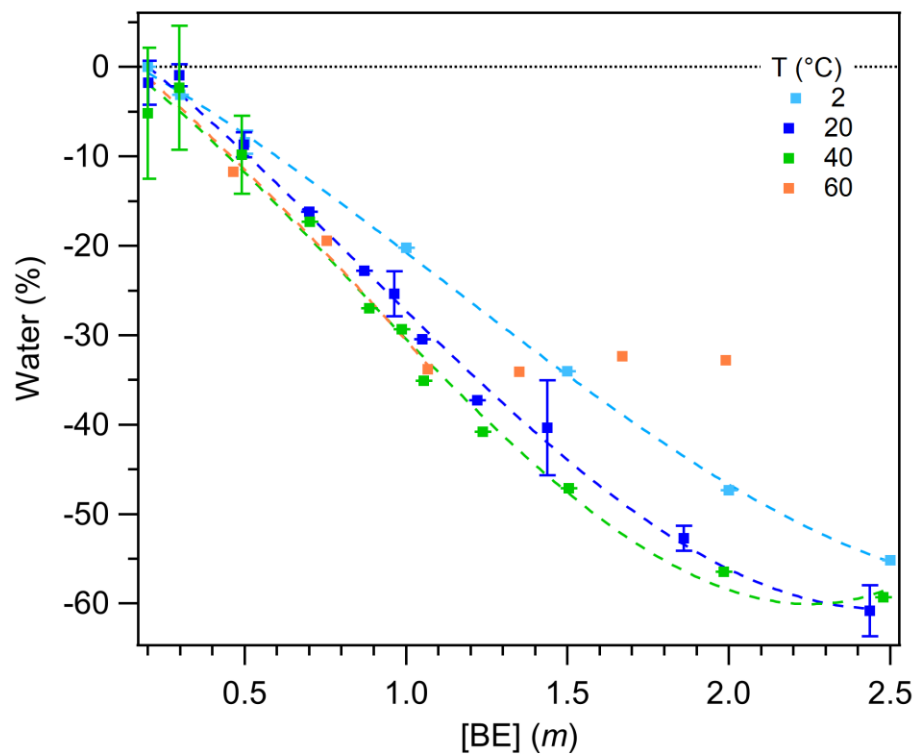


Figure A.3 Hydration shell depletion for BE with respect to concentration at 2°C, 20°C, 40°C, and 60°C. Dashed lines are fourth order polynomial fits to the data. The fit for the 60°C data was only done in the monophasic region (up to 1.0 m at 60°C) of the aqueous BE phase diagram.

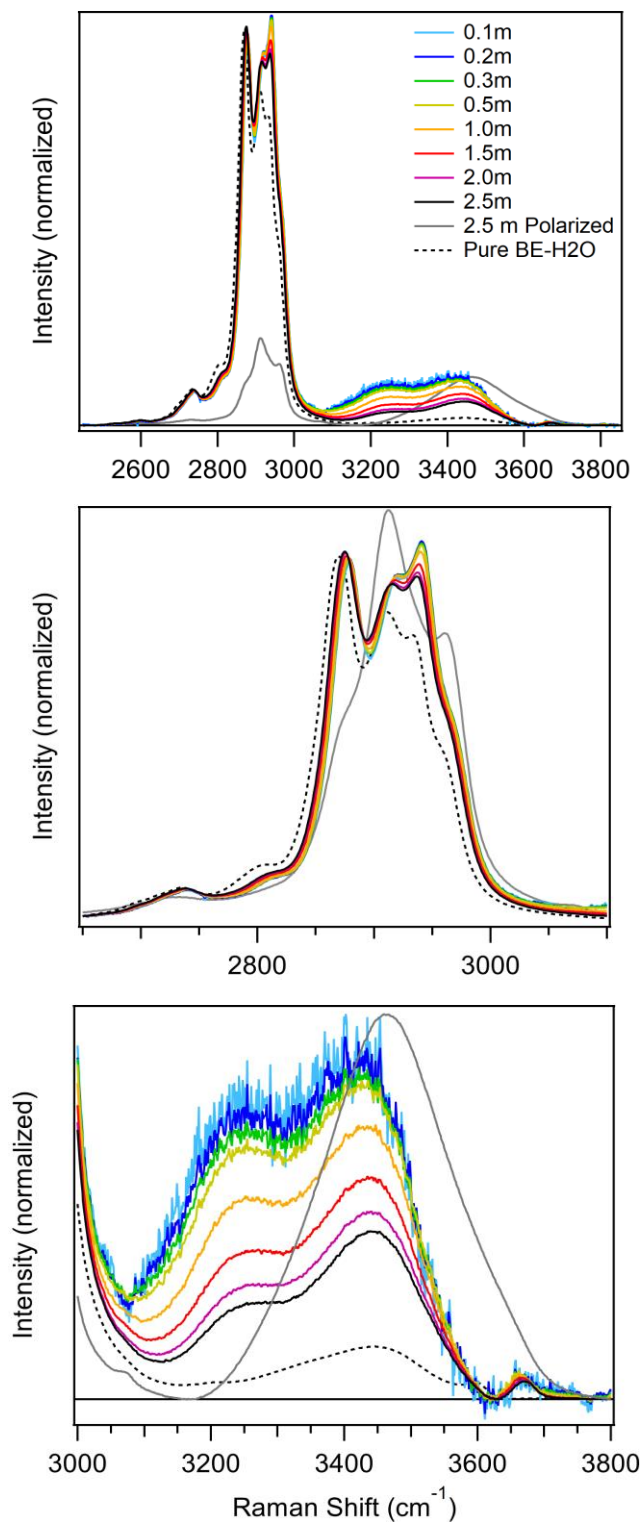


Figure A.4 Concentration dependent hydration shells spectra for BE taken with the 1200 grooves/mm monochromator grating.

APPENDIX B. ALKALI METAL HALIDE SPECTRA

All spectra shown here are solute-correlated spectra normalized by the molar solute concentration. More specifically, the following spectra are obtained by taking each solute-correlated baseline subtracted component (SCcompback) from SMCR and dividing by the molar concentration of the solute in the input solution.

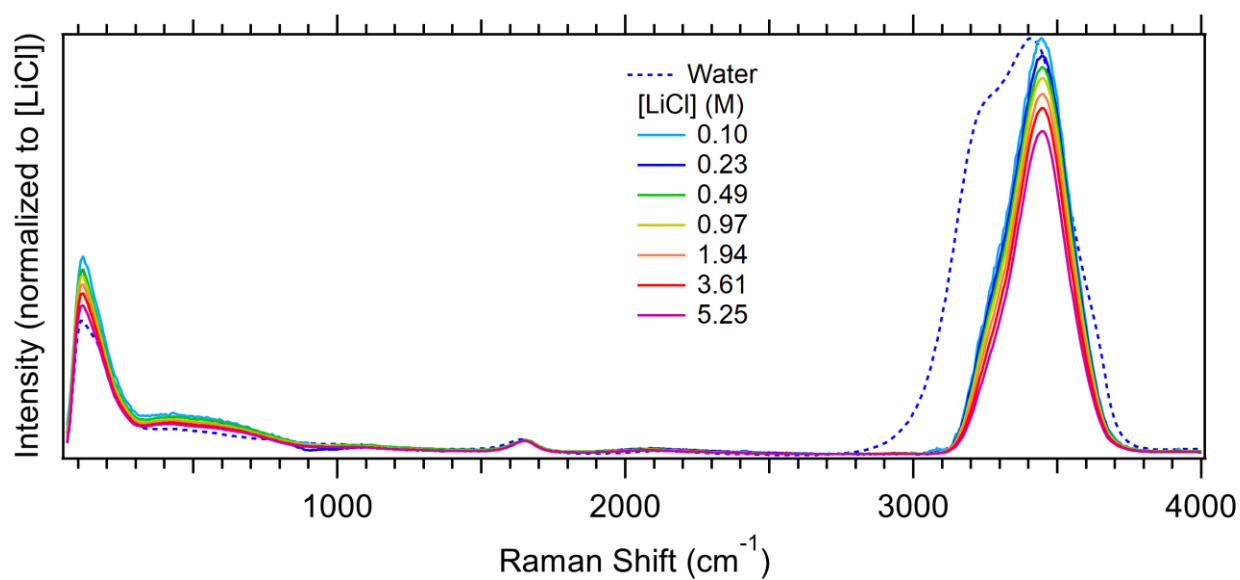


Figure B.1 Lithium chloride (LiCl) correlated spectra.

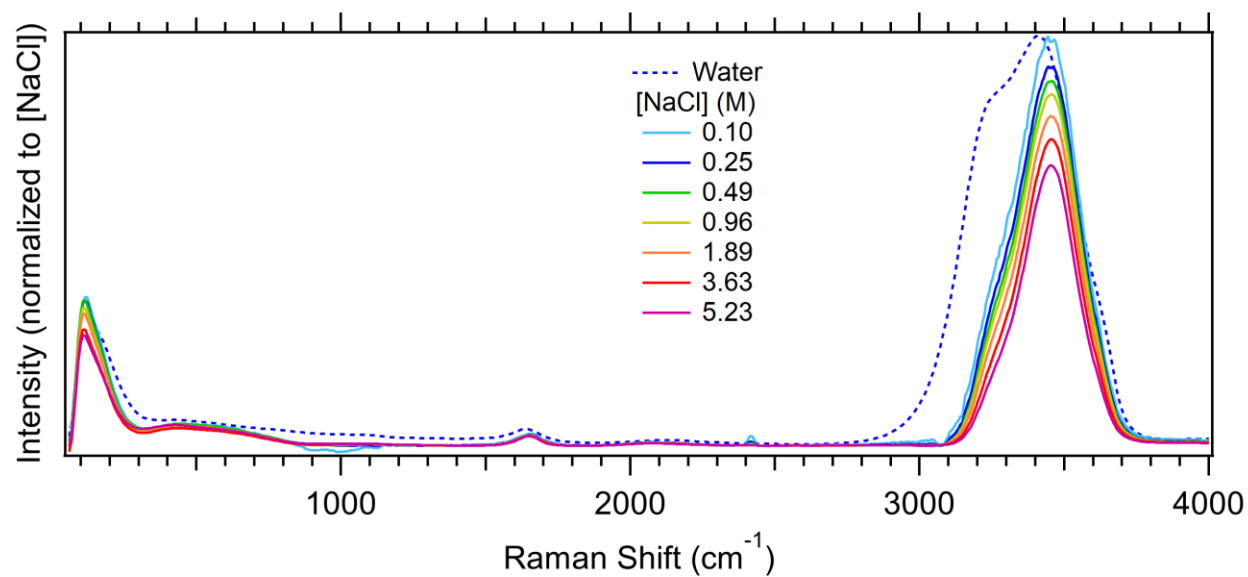


Figure B.2 Sodium chloride (NaCl) correlated spectra.

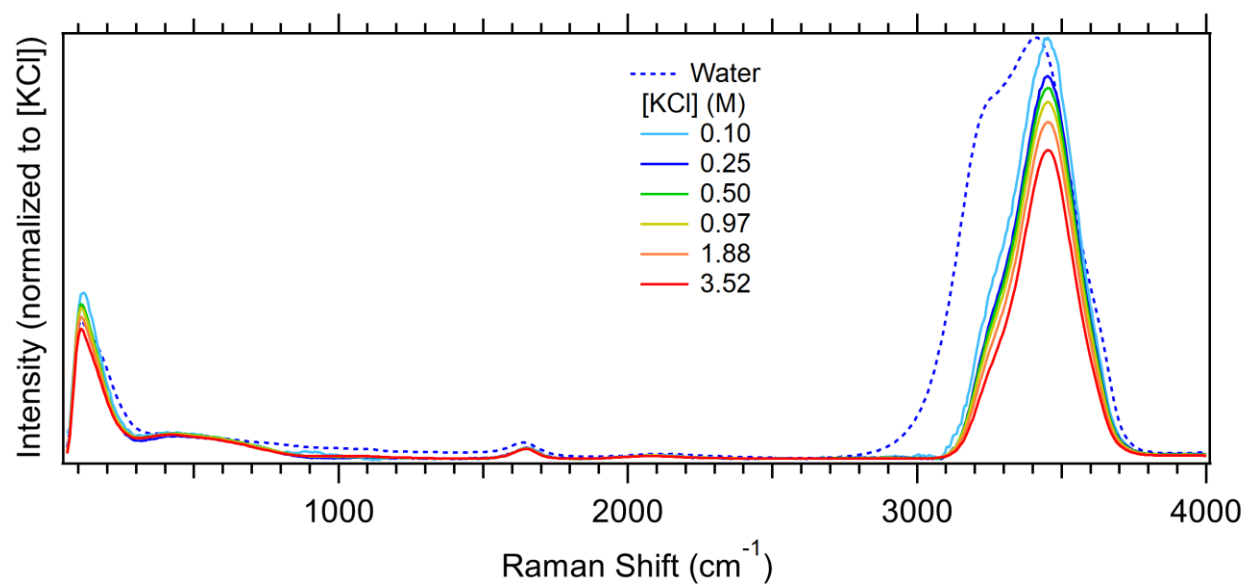


Figure B.3 Potassium chloride (KCl) correlated spectra.

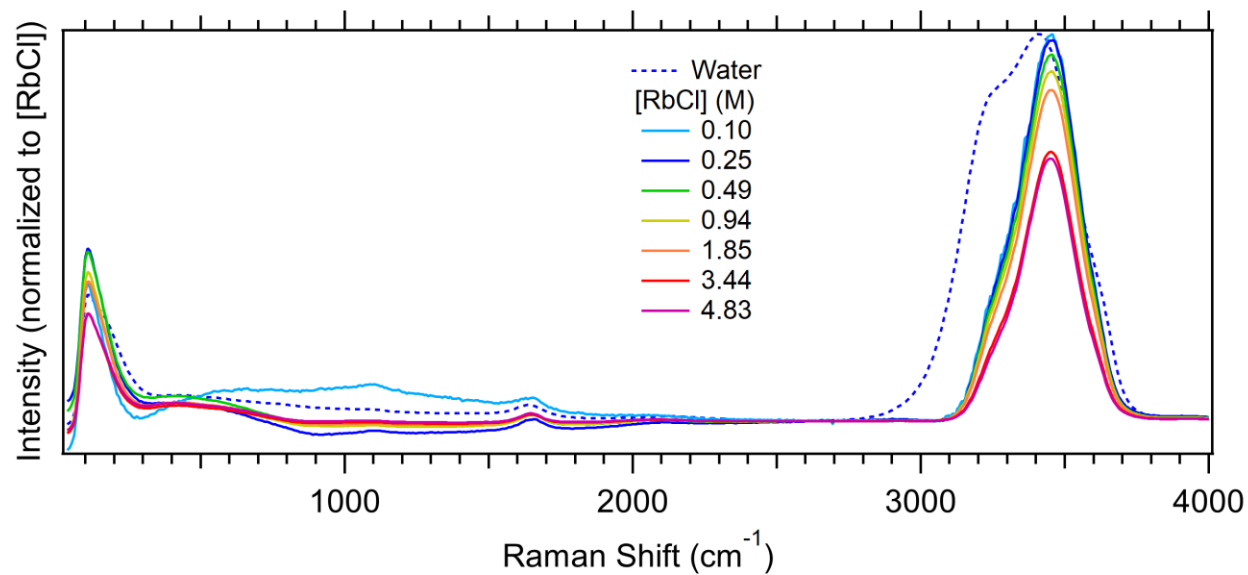


Figure B.4 Rubidium chloride (RbCl) correlated spectra.

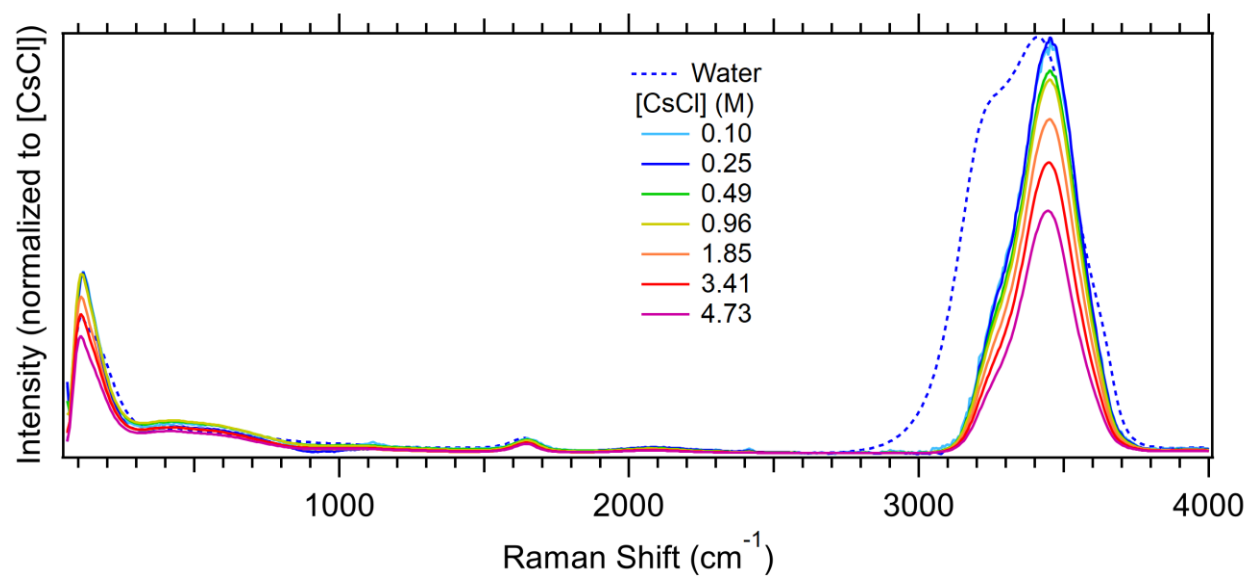


Figure B.5 Cesium chloride (CsCl) correlated spectra.

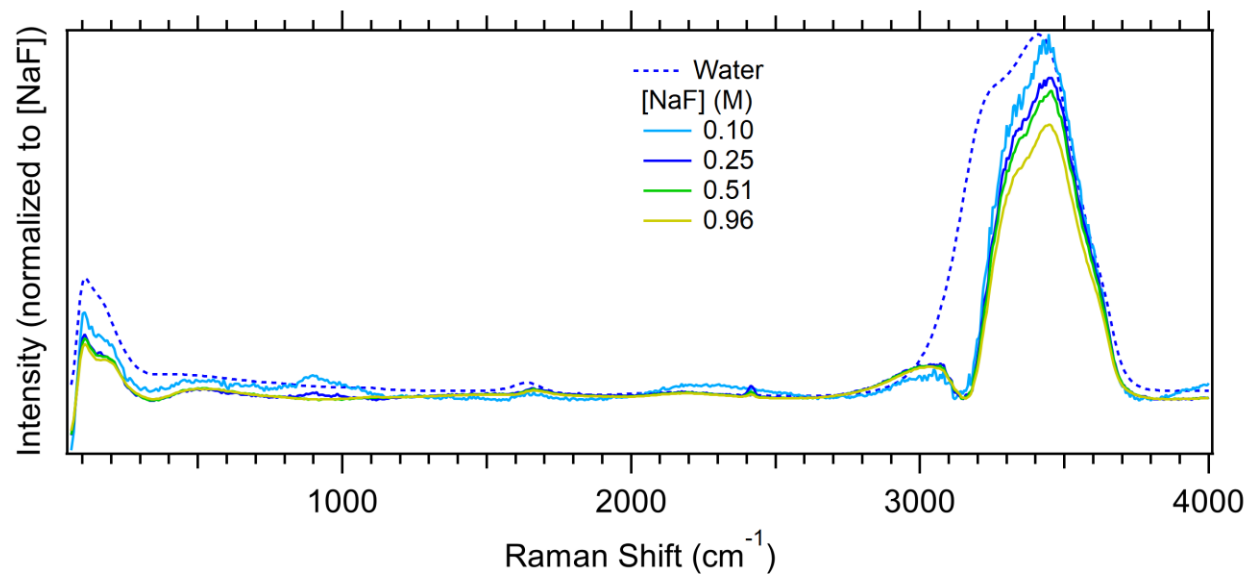


Figure B.6 Sodium fluoride (NaF) correlated spectra.

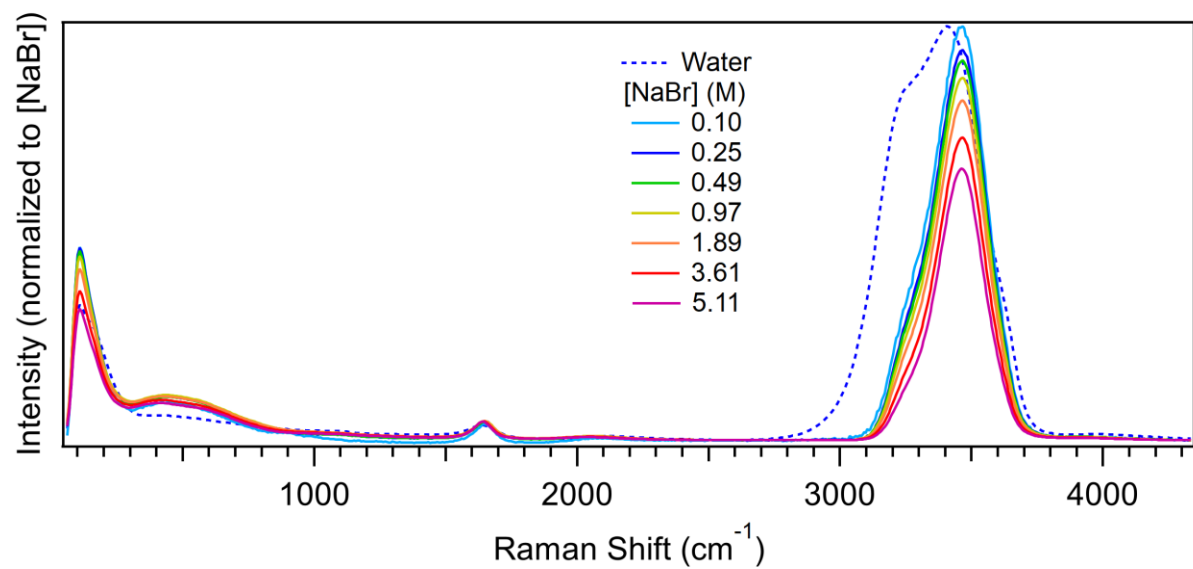


Figure B.7 Sodium bromide (NaBr) correlated spectra.

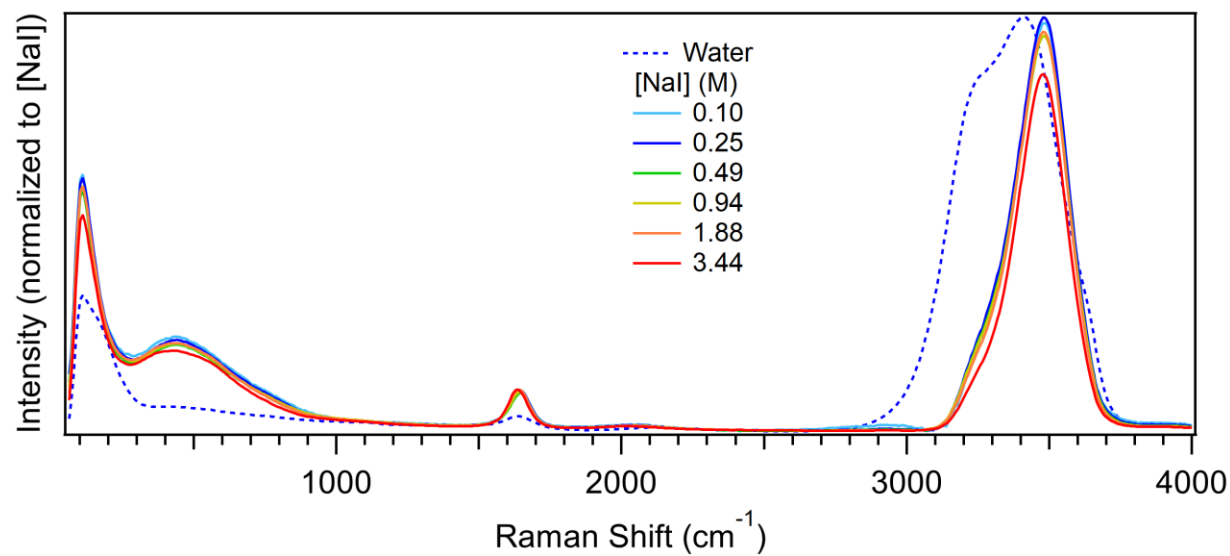


Figure B.8 Sodium iodide (NaI) correlated spectra.

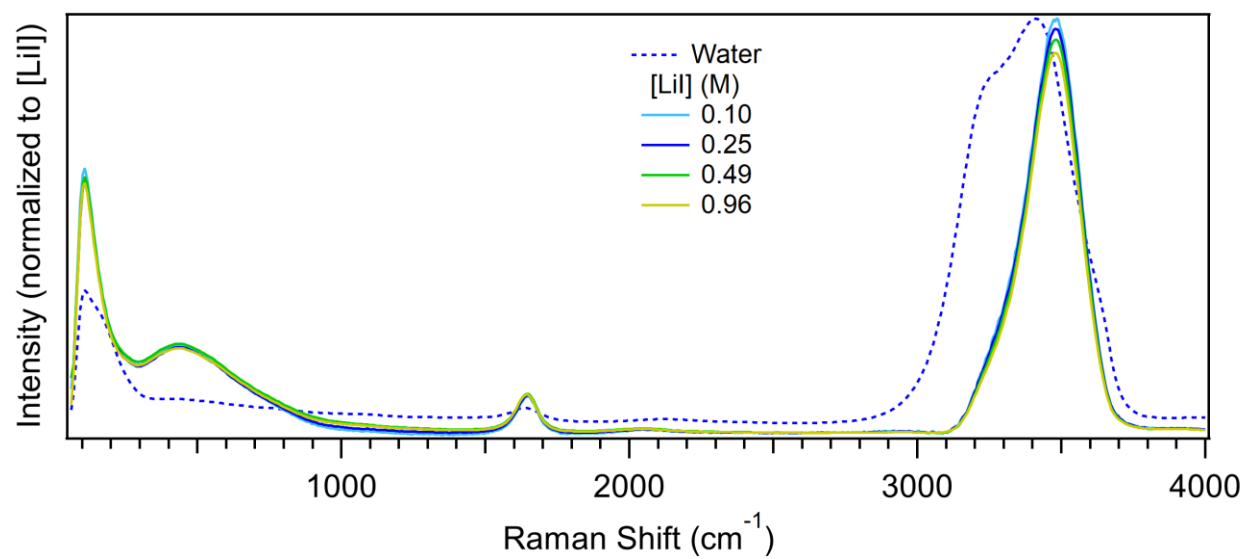


Figure B.9 Lithium iodide (LiI) correlated spectra.

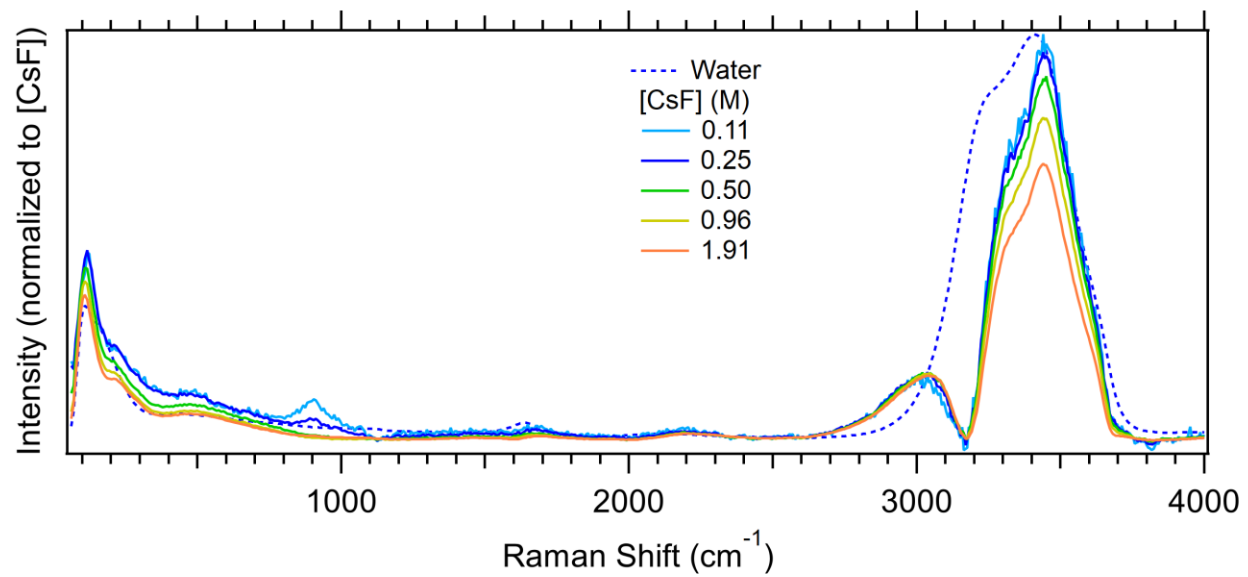


Figure B.10 Cesium fluoride (CsF) correlated spectra.

REFERENCES

1. LaPlant, F.; Ben-Amotz, D., Design and construction of a microscope-based Raman system. *Review of Scientific Instruments* **1995**, *66* (6), 3537-3544.
2. Gierszal, K. P.; Davis, J. G.; Hands, M. D.; Wilcox, D. S.; Slipchenko, L. V.; Ben-Amotz, D., π -Hydrogen Bonding in Liquid Water. *The Journal of Physical Chemistry Letters* **2011**, *2* (22), 2930-2933.
3. Davis, J. G.; Gierszal, K. P.; Wang, P.; Ben-Amotz, D., Water structural transformation at molecular hydrophobic interfaces. *Nature* **2012**, *491* (7425), 582-585.
4. Fega, K. R.; Wilcox, D. S.; Ben-Amotz, D., Application of Raman Multivariate Curve Resolution to Solvation-Shell Spectroscopy. *Applied Spectroscopy* **2012**, *66* (3), 282-288.
5. Ball, P., Water as an Active Constituent in Cell Biology. *Chemical Reviews* **2008**, *108* (1), 74-108.
6. Kauzmann, W., Some Factors in the Interpretation of Protein Denaturation¹. In *Advances in Protein Chemistry*, C.B. Anfinsen, M. L. A. K. B.; John, T. E., Eds. Academic Press: 1959; Vol. Volume 14, pp 1-63.
7. Rankin, B. M.; Ben-Amotz, D.; van der Post, S. T.; Bakker, H. J., Contacts Between Alcohols in Water Are Random Rather than Hydrophobic. *J. Phys. Chem. Lett.* **2015**, *6* (4), 688-692.
8. Ben-Amotz, D., Hydrophobic Ambivalence: Teetering on the Edge of Randomness. *J. Phys. Chem. Lett.* **2015**, *6* (9), 1696-1701.
9. Ben-Amotz, D., Water-Mediated Hydrophobic Interactions. *Annual Review of Physical Chemistry* **2016**, *67* (1), 617-638.
10. Indra, S.; Biswas, R., Heterogeneity in (2-butoxyethanol + water) mixtures: Hydrophobicity-induced aggregation or criticality-driven concentration fluctuations? *The Journal of Chemical Physics* **2015**, *142* (20), 204501.
11. Gupta, R.; Patey, G. N., Association and Microheterogeneity in Aqueous 2-Butoxyethanol Solutions. *The Journal of Physical Chemistry B* **2011**, *115* (51), 15323-15331.
12. Stillinger, F., Structure in aqueous solutions of nonpolar solutes from the standpoint of scaled-particle theory. *J Solution Chem* **1973**, *2* (2-3), 141-158.
13. Huang, D. M.; Chandler, D., Temperature and length scale dependence of hydrophobic effects and their possible implications for protein folding. *Proceedings of the National Academy of Sciences* **2000**, *97* (15), 8324-8327.
14. Chandler, D., Interfaces and the driving force of hydrophobic assembly. *Nature* **2005**, *437* (7059), 640-647.
15. Berne, B. J.; Weeks, J. D.; Zhou, R. H., Dewetting and Hydrophobic Interaction in Physical and Biological Systems. *Annual Review of Physical Chemistry* **2009**, *60*, 85-103.

16. Ashbaugh, H. S.; Pratt, L. R., Colloquium: Scaled particle theory and the length scales of hydrophobicity. *Rev. Mod. Phys.* **2006**, *78*, 159-178.
17. Garde, S.; Patel, A. J., Unraveling the hydrophobic effect, one molecule at a time. *Proc. Natl. Acad. Sci. U. S. A.* **2011**, *108* (40), 16491-16492.
18. Cerdeirina, C. A.; Debenedetti, P. G.; Rossky, P. J.; Giovambattista, N., Evaporation Length Scales of Confined Water and Some Common Organic Liquids. *J. Phys. Chem. Lett.* **2011**, *2* (9), 1000-1003.
19. Huang, N.; Schlesinger, D.; Nordlund, D.; Huang, C.; Tyliszczak, T.; Weiss, T. M.; Acremann, Y.; Pettersson, L. G. M.; Nilsson, A., Microscopic probing of the size dependence in hydrophobic solvation. *The Journal of Chemical Physics* **2012**, *136* (7), 074507.
20. Li, I. T. S.; Walker, G. C., Single Polymer Studies of Hydrophobic Hydration. *Accounts of Chemical Research* **2012**, *45* (11), 2011-2021.
21. Li, I. T. S.; Walker, G. C., Signature of hydrophobic hydration in a single polymer. *Proc. Natl. Acad. Sci. U. S. A.* **2011**, *108* (40), 16527-16532.
22. Bakker, H. J., PHYSICAL CHEMISTRY Water's response to the fear of water. *Nature* **2012**, *491* (7425), 533-535.
23. Makowski, M.; Czaplewski, C.; Liwo, A.; Scheraga, H. A., Potential of Mean Force of Association of Large Hydrophobic Particles: Toward the Nanoscale Limit. *J. Phys. Chem. B* **2010**, *114* (2), 993-1003.
24. Perera, P.; Wyche, M.; Loethen, Y.; Ben-Amotz, D., Solute-Induced Perturbations of Solvent-Shell Molecules Observed Using Multivariate Raman Curve Resolution. *Journal of the American Chemical Society* **2008**, *130* (14), 4576-4577.
25. Wilcox, D. S.; Rankin, B. M.; Ben-Amotz, D., Distinguishing aggregation from random mixing in aqueous t-butyl alcohol solutions. *Faraday Discussions* **2013**, *167* (0), 177-190.
26. Tauler, R.; Smilde, A.; Kowalski, B., SELECTIVITY, LOCAL RANK, 3-WAY DATA-ANALYSIS AND AMBIGUITY IN MULTIVARIATE CURVE RESOLUTION. *Journal of Chemometrics* **1995**, *9* (1), 31-58.
27. Rankin, B. M. Quantification of molecular aggregation equilibria using spectroscopic measurements and random mixing modeling. Purdue University, Ann Arbor, 2015.
28. Martin, M. G.; Siepmann, J. I., Transferable Potentials for Phase Equilibria. 1. United-Atom Description of n-Alkanes. *The Journal of Physical Chemistry B* **1998**, *102* (14), 2569-2577.
29. M.J. Abraham, D. v. d. S., E. Lindahl, B. Hess, and the GROMACS development team, GROMACS User Manual version 5.1.2. 2016.
30. Vorobyov, I.; Anisimov, V. M.; Greene, S.; Venable, R. M.; Moser, A.; Pastor, R. W.; MacKerell, A. D., Additive and Classical Drude Polarizable Force Fields for Linear and Cyclic Ethers. *Journal of Chemical Theory and Computation* **2007**, *3* (3), 1120-1133.

31. Vanommeslaeghe, K.; Hatcher, E.; Acharya, C.; Kundu, S.; Zhong, S.; Shim, J.; Darian, E.; Guvench, O.; Lopes, P.; Vorobyov, I.; Mackerell, A. D., CHARMM general force field: A force field for drug-like molecules compatible with the CHARMM all-atom additive biological force fields. *Journal of Computational Chemistry* **2010**, *31* (4), 671-690.
32. Yu, W.; He, X.; Vanommeslaeghe, K.; MacKerell, A. D., Extension of the CHARMM general force field to sulfonyl-containing compounds and its utility in biomolecular simulations. *Journal of Computational Chemistry* **2012**, *33* (31), 2451-2468.
33. Zoete, V.; Cuendet, M. A.; Grosdidier, A.; Michielin, O., SwissParam: a fast force field generation tool for small organic molecules. *Journal of computational chemistry* **2011**, *32* (11), 2359-2368.
34. Jorgensen, W. L.; Chandrasekhar, J.; Madura, J. D.; Impey, R. W.; Klein, M. L., Comparison of simple potential functions for simulating liquid water. *The Journal of chemical physics* **1983**, *79* (2), 926-935.
35. Abascal, J. L. F.; Vega, C., A general purpose model for the condensed phases of water: TIP4P/2005. *The Journal of Chemical Physics* **2005**, *123* (23), 234505.
36. Ashbaugh, H. S.; Liu, L.; Surampudi, L. N., Optimization of linear and branched alkane interactions with water to simulate hydrophobic hydration. *The Journal of Chemical Physics* **2011**, *135* (5), 054510.
37. Martin, M. G.; Siepmann, J. I., Novel Configurational-Bias Monte Carlo Method for Branched Molecules. Transferable Potentials for Phase Equilibria. 2. United-Atom Description of Branched Alkanes. *The Journal of Physical Chemistry B* **1999**, *103* (21), 4508-4517.
38. Chen, B.; Potoff, J. J.; Siepmann, J. I., Monte Carlo calculations for alcohols and their mixtures with alkanes. Transferable potentials for phase equilibria. 5. United-atom description of primary, secondary, and tertiary alcohols. *The Journal of Physical Chemistry B* **2001**, *105* (15), 3093-3104.
39. Stubbs, J. M.; Potoff, J. J.; Siepmann, J. I., Transferable potentials for phase equilibria. 6. United-atom description for ethers, glycols, ketones, and aldehydes. *The Journal of Physical Chemistry B* **2004**, *108* (45), 17596-17605.
40. Lawton, W. H.; Sylvestre, E. A., Self Modeling Curve Resolution. *Technometrics* **1971**, *13* (3), 617-633.
41. Davis, J. G. Spectroscopic investigations of water-mediated interactions. Purdue University, Ann Arbor, 2012.
42. Ben-Amotz, D.; Rankin, B. M.; Widom, B., Molecular Aggregation Equilibria. Comparison of Finite Lattice and Weighted Random Mixing Predictions. *The Journal of Physical Chemistry B* **2014**, *118* (28), 7878-7885.
43. Perera, P. N.; Fega, K. R.; Lawrence, C.; Sundstrom, E. J.; Tomlinson-Phillips, J.; Ben-Amotz, D., Observation of water dangling OH bonds around dissolved nonpolar groups. *Proceedings of the National Academy of Sciences* **2009**, *106* (30), 12230-12234.

44. Frank, H. S.; Evans, M. W., Free Volume and Entropy in Condensed Systems III. Entropy in Binary Liquid Mixtures; Partial Molal Entropy in Dilute Solutions; Structure and Thermodynamics in Aqueous Electrolytes. *The Journal of Chemical Physics* **1945**, *13* (11), 507-532.
45. Glew, D. N., AQUEOUS SOLUBILITY AND THE GAS-HYDRATES. THE METHANE-WATER SYSTEM¹. *The Journal of Physical Chemistry* **1962**, *66* (4), 605-609.
46. Galamba, N., Water's Structure around Hydrophobic Solutes and the Iceberg Model. *The Journal of Physical Chemistry B* **2013**, *117* (7), 2153-2159.
47. Rossky, P. J.; Zichi, D. A., Molecular librations and solvent orientational correlations in hydrophobic phenomena. *Faraday Symposia of the Chemical Society* **1982**, *17* (0), 69-78.
48. Raschke, T. M.; Levitt, M., Nonpolar solutes enhance water structure within hydration shells while reducing interactions between them. *Proc. Natl. Acad. Sci. U. S. A.* **2005**, *102* (19), 6777-6782.
49. Ashbaugh, H. S.; Barnett, J. W.; Saltzman, A.; Langrehr, M. E.; Houser, H., Communication: Stiffening of dilute alcohol and alkane mixtures with water. *The Journal of chemical physics* **2016**, *145* (20), 201102.
50. Meister, K.; Strazdaite, S.; DeVries, A. L.; Lotze, S.; Olijve, L. L. C.; Voets, I. K.; Bakker, H. J., Observation of ice-like water layers at an aqueous protein surface. *Proceedings of the National Academy of Sciences* **2014**, *111* (50), 17732-17736.
51. Dolenko, T. A.; Burikov, S. A.; Dolenko, S. A.; Efitorov, A. O.; Plastinin, I. V.; Yuzhakov, V. I.; Patsaeva, S. V., Raman Spectroscopy of Water–Ethanol Solutions: The Estimation of Hydrogen Bonding Energy and the Appearance of Clathrate-like Structures in Solutions. *The Journal of Physical Chemistry A* **2015**, *119* (44), 10806-10815.
52. Bakulin, A. A.; Liang, C.; la Cour Jansen, T.; Wiersma, D. A.; Bakker, H. J.; Pshenichnikov, M. S., Hydrophobic Solvation: A 2D IR Spectroscopic Inquest. *Accounts of Chemical Research* **2009**, *42* (9), 1229-1238.
53. Buchanan, P.; Aldiwan, N.; Soper, A. K.; Creek, J. L.; Koh, C. A., Decreased structure on dissolving methane in water. *Chemical Physics Letters* **2005**, *415* (1–3), 89-93.
54. Prasad, P. S. R.; Sowjanya, Y.; Shiva Prasad, K., Micro-Raman investigations of mixed gas hydrates. *Vibrational Spectroscopy* **2009**, *50* (2), 319-323.
55. Takasu, Y.; Nishio, I., New Analysis of Low Frequency Raman Spectra of THF Aqueous Solution and its Coexisting Phase with Clathrate Hydrate. *Journal of the Physical Society of Japan* **2003**, *72* (8), 2106-2109.
56. Takasu, Y.; Iwai, K.; Nishio, I., Low Frequency Raman Profile of Type II Clathrate Hydrate of THF and Its Application for Phase Identification. *Journal of the Physical Society of Japan* **2003**, *72* (5), 1287-1291.
57. Tulk, C. A.; Klug, D. D.; Ripmeester, J. A., Raman Spectroscopic Studies of THF Clathrate Hydrate. *The Journal of Physical Chemistry A* **1998**, *102* (45), 8734-8739.

58. Yang, M.; Skinner, J. L., Signatures of coherent vibrational energy transfer in IR and Raman line shapes for liquid water. *Physical Chemistry Chemical Physics* **2010**, *12* (4), 982-991.
59. Chau, P. L.; Hardwick, A. J., A new order parameter for tetrahedral configurations. *Molecular Physics* **1998**, *93* (3), 511-518.
60. Errington, J. R.; Debenedetti, P. G., Relationship between structural order and the anomalies of liquid water. *Nature* **2001**, *409* (6818), 318.
61. Collins, K. D., Ion hydration: Implications for cellular function, polyelectrolytes, and protein crystallization. *Biophysical Chemistry* **2006**, *119* (3), 271-281.
62. Irudayam, S. J.; Henchman, R. H., Prediction and interpretation of the hydration entropies of monovalent cations and anions. *Molecular Physics* **2010**, *109* (1), 37-48.
63. Whittingham, M. S., Lithium Batteries and Cathode Materials. *Chemical Reviews* **2004**, *104* (10), 4271-4302.
64. Abernethy, J. L., Franz Hofmeister - The impact of his life and research on chemistry. *Journal of Chemical Education* **1967**, *44* (3), 177.
65. Jagoda-Cwiklik, B.; Vácha, R.; Lund, M.; Srebro, M.; Jungwirth, P., Ion Pairing as a Possible Clue for Discriminating between Sodium and Potassium in Biological and Other Complex Environments. *The Journal of Physical Chemistry B* **2007**, *111* (51), 14077-14079.
66. Pluharova, E.; Mason, P. E.; Jungwirth, P., Ion Pairing in Aqueous Lithium Salt Solutions with Monovalent and Divalent Counter-Anions. *Journal of Physical Chemistry A* **2013**, *117* (46), 11766-11773.
67. Luo, Y.; Roux, B., Simulation of Osmotic Pressure in Concentrated Aqueous Salt Solutions. *The Journal of Physical Chemistry Letters* **2009**, *1* (1), 183-189.
68. Zhang, Z. G.; Duan, Z. H., Lithium chloride ionic association in dilute aqueous solution: a constrained molecular dynamics study. *Chem. Phys.* **2004**, *297* (1-3), 221-233.
69. Galamba, N., On the Effects of Temperature, Pressure, and Dissolved Salts on the Hydrogen-Bond Network of Water. *The Journal of Physical Chemistry B* **2012**, *117* (2), 589-601.
70. Kurisaki, I.; Takahashi, T., Assessment of dynamic properties of water around a monovalent ion: A classical molecular dynamics simulation study. *Computational and Theoretical Chemistry* **2011**, *966* (1-3), 26-30.
71. Kiriukhin, M. Y.; Collins, K. D., Dynamic hydration numbers for biologically important ions. *Biophysical Chemistry* **2002**, *99* (2), 155-168.
72. Collins, K. D., Ions from the Hofmeister series and osmolytes: effects on proteins in solution and in the crystallization process. *Methods* **2004**, *34* (3), 300-311.
73. Wachter, W.; Kunz, W.; Buchner, R.; Hefter, G., Is There an Anionic Hofmeister Effect on Water Dynamics? Dielectric Spectroscopy of Aqueous Solutions of NaBr, NaI, NaNO₃, NaClO₄, and NaSCN. *The Journal of Physical Chemistry A* **2005**, *109* (39), 8675-8683.

74. Tielrooij, K. J.; Garcia-Araez, N.; Bonn, M.; Bakker, H. J., Cooperativity in Ion Hydration. *Science* **2010**, *328* (5981), 1006-1009.
75. Heisler, I. A.; Mazur, K.; Meech, S. R., Low-Frequency Modes of Aqueous Alkali Halide Solutions: An Ultrafast Optical Kerr Effect Study. *The Journal of Physical Chemistry B* **2011**, *115* (8), 1863-1873.
76. Perera, P. N.; Browder, B.; Ben-Amotz, D., Perturbations of Water by Alkali Halide Ions Measured using Multivariate Raman Curve Resolution. *The Journal of Physical Chemistry B* **2009**, *113* (7), 1805-1809.
77. Collins, K. D.; Washabaugh, M. W., The Hofmeister effect and the behaviour of water at interfaces. *Quarterly Reviews of Biophysics* **1985**, *18* (04), 323-422.
78. Collins, K. D., Sticky Ions in Biological Systems. *Proc. Natl. Acad. Sci. U. S. A.* **1995**, *92* (12), 5553-5557.
79. Takamuku, T.; Tabata, M.; Yamaguchi, A.; Nishimoto, J.; Kumamoto, M.; Wakita, H.; Yamaguchi, T., Liquid structure of acetonitrile– water mixtures by X-ray diffraction and infrared spectroscopy. *The Journal of Physical Chemistry B* **1998**, *102* (44), 8880-8888.
80. Chen, J.; Sit, P. H.-L., Ab initio study of the structural properties of acetonitrile–water mixtures. *Chem. Phys.* **2015**, *457*, 87-97.
81. Venables, D.; Schmuttenmaer, C., Far-infrared spectra and associated dynamics in acetonitrile–water mixtures measured with femtosecond THz pulse spectroscopy. *The Journal of chemical physics* **1998**, *108* (12), 4935-4944.
82. Bertie, J. E.; Lan, Z., Liquid Water– Acetonitrile Mixtures at 25° C: The Hydrogen-Bonded Structure Studied through Infrared Absolute Integrated Absorption Intensities. *The Journal of Physical Chemistry B* **1997**, *101* (20), 4111-4119.
83. Jamroz, D.; Stangret, J.; Lindgren, J., An infrared spectroscopic study of the preferential solvation in water-acetonitrile mixtures. *Journal of the American Chemical Society* **1993**, *115* (14), 6165-6168.
84. Zukowski, S. R.; Mitev, P. D.; Hermansson, K.; Ben-Amotz, D., CO₂ Hydration Shell Structure and Transformation. *The Journal of Physical Chemistry Letters* **2017**, *8* (13), 2971-2975.
85. Davis, J. G.; Zukowski, S. R.; Rankin, B. M.; Ben-Amotz, D., Influence of a Neighboring Charged Group on Hydrophobic Hydration Shell Structure. *The Journal of Physical Chemistry B* **2014**.
86. Ben-Naim, A., Hydrophobic hydrophilic phenomena in biochemical processes. *Biophysical Chemistry* **2003**, *105* (2), 183-193.
87. Ben-Naim, A.; Wilf, J., A direct measurement of intramolecular hydrophobic interactions. *The Journal of Chemical Physics* **1979**, *70* (2), 771-777.
88. Ben-Naim, A., Statistical mechanical study of hydrophobic interaction. I. Interaction between two identical nonpolar solute particles. *The Journal of Chemical Physics* **1971**, *54* (3), 1387-1404.

VITA

Shannon R. Pattenauade was born on May 8, 1990 and grew up in Altamont, IL. She graduated as valedictorian from Altamont Community High School in 2008. She obtained her Associate of Science Degree in Chemistry from Lake Land College in Mattoon, IL in 2010 and her Bachelors of Science in Chemistry from Southern Illinois University in Carbondale, IL in 2012. In May 2018, she received a Doctor of Philosophy in Chemistry from Purdue University in West Lafayette, IN.

PUBLICATION



PCCP

PAPER



Cite this: *Phys. Chem. Chem. Phys.*,
2016, **18**, 24937

Received 22nd June 2016,
Accepted 16th August 2016

DOI: 10.1039/c6cp04379h

www.rsc.org/pccp

Water-mediated aggregation of 2-butoxyethanol†

Shannon R. Pattenaude,^a Blake M. Rankin,^{ab} Kenji Mochizuki^c and Dor Ben-Amotz^{*a}

Water plays an important role in mediating hydrophobic interactions, and yet open questions remain regarding the magnitude, and even the sign, of water-mediated contributions to the potential of mean force between a pair of oily molecules dissolved in water. Here, the water-mediated interaction between 2-butoxyethanol (BE) molecules dissolved in water is quantified using Raman multivariate curve resolution (Raman-MCR), molecular dynamics (MD) simulations, and random mixing (RM) predictions. Our results indicate that the number of contacts between BE molecules at concentrations between 0.2 M and 1 M exceeds RM predictions, but is less than some MD predictions. Moreover, the potential of mean force between BE molecules in water has a well depth that is shallower than the direct interaction between 1-ethoxybutane chains in the gas phase, and thus the water-mediated contribution to BE aggregation is repulsive, as it pulls BE molecules apart rather than pushing them together.

1. Introduction

Hydrophobic interactions are considered to play a key role in self-assembly processes ranging from micelle and membrane formation to protein folding and ligand binding.^{1,2} However, recent studies of aqueous solutions containing small alcohol molecules (ranging from methanol to butanol isomers) found that the number of hydrophobic contacts in such solutions is similar to that expected in a random mixture of non-interacting solute molecules,³ thus implying that hydrophobic interactions between small hydrophobic groups are too weak to compete with random thermal energy fluctuations (of magnitude $RT \sim 2.5 \text{ kJ mol}^{-1}$).³⁻⁵ Here, we investigate the aggregation of aqueous 2-butoxyethanol (BE, $n\text{-C}_4\text{H}_9\text{OC}_2\text{H}_4\text{OH}$)^{6,7} in an effort to establish the solute size at which hydrophobic interactions begin to exceed thermal fluctuations. Our results reveal that the magnitude of the BE contact free energy in water slightly exceeds RT , and thus is clearly more attractive than that for smaller alcohol solutes. However, our results also indicate that the contact free energy of BE is smaller (less attractive) than the direct van der Waals interaction energy between the corresponding oily tails, as modeled using the interaction of two isolated (gas phase) 1-ethoxybutane (EB) molecules. The latter results imply that

the water-mediated hydrophobic interaction between BE molecules is repulsive, thus favoring solvent-separated over direct contact configurations.

The notion that hydrophobicity may be influenced by a solute size dependent crossover was first proposed by Kauzmann,² who noted that while molecular hydrophobic hydration has a negative enthalpy and entropy (under ambient conditions), macroscopic oil-water interfacial tension implies that these thermodynamic signatures should change sign as solute size increases. The fact that purely repulsive (hard-sphere) hydrophobic solutes must undergo a size dependent crossover was first demonstrated by Stillinger,⁸ and motivated the subsequent development of Lum-Chandler-Weeks (LCW) theory.^{9,10} Although numerous simulations,¹¹⁻¹⁴ and some experiments,¹⁵⁻¹⁸ have obtained evidence of a size dependent crossover,^{13,19} some recent simulations²⁰ and experiments³ imply that solute attractive interactions can give rise to a competing crossover that weakens rather than strengthens hydrophobic interactions.^{4,5} In other words, while entropic depletion forces and the associated size dependent dewetting crossover give rise to strongly attractive water-mediated hydrophobic interactions, oil-water cohesive (van der Waals) interactions stabilize the hydrophobic hydration-shell around separated (non-contacting) oily molecules, and thus drive oily molecules apart. The present results confirm that BE is sufficiently large that its cohesive attraction to water overcomes the competing entropic depletion force, and thus BE is above the crossover at which oil-water cohesion dictates the positive (repulsive) sign of the associated water-mediated hydrophobic interactions.

Our experimental results are obtained using Raman multivariate curve resolution (Raman-MCR) spectroscopy,^{16,21,22} which we use to quantify aggregation induced changes in the hydration-shell spectra of BE. The inferred BE contact probabilities are

^a Department of Chemistry, Purdue University, West Lafayette, IN 47907, USA.
E-mail: bendor@purdue.edu

^b Air Force Research Laboratory, Wright-Patterson Air Force Base, Dayton, Ohio 45433, USA

^c Research Institute for Interdisciplinary Science, Okayama University, Okayama 700-8530, Japan

† Electronic supplementary information (ESI) available: BE density-based concentration unit conversions, vibrational CH frequency shifts, WRM and MD simulation details. See DOI: 10.1039/c6cp04379h

compared with random mixing (RM) simulation predictions to estimate the BE contact free energy in water, which is subsequently compared with molecular dynamics (MD) simulation predictions obtained using two different potential functions. The present results extend our recent Raman-MCR studies of the aggregation of *tert*-butyl alcohol (TBA)^{3,23} which quantified the depletion of the first hydration-shell water molecules resulting from hydrophobic contacts between TBA molecules. However, the mathematical “rotational ambiguity” associated with MCR spectral decomposition^{22–24} resulted in relatively large uncertainties in the concentrations of the monomeric (non-aggregated) and aggregated TBA molecules. This rotational ambiguity essentially amounts to an uncertainty regarding the number of water molecules that are removed from the first hydration shell of a solute as the result of solute–solute contacts. In our initial Raman-MCR studies of TBA²³ we assumed that bringing a pair of TBA molecules into direct contact produced an average depletion of 12.6%, while in our subsequent study, which combined Raman-MCR with femtosecond infrared (fs-IR) anisotropy measurements,³ it was concluded that TBA contacts produced between 25.5% and 71.3% depletion, thus leading to qualitatively similar, but quantitatively different conclusions regarding the concentration of monomeric and aggregated TBA molecules.

Here we describe an alternative analysis strategy that is more appropriate for quantifying contacts between flexible BE chains. This strategy quantifies the local hydration-shell depletion induced by contacts between CH groups on different BE molecules, each of which are estimated to produce a substantial ($\sim 65\% \pm 15\%$) local depletion in the number of water molecules in the first hydration-shell surrounding each individual contacted CH group. Moreover, we use MD simulations to correlate the probability of such CH contacts with the probability that a solute will have either no contacts (and so is classified as a monomer) or at least one contact (and so is classified as aggregated). The primary benefit of this new analysis strategy derives from the fact that each CH contact must necessarily produce a significant depletion in the local number of hydration-shell water molecules, while the total experimentally measured depletion arises from the sum of the individual contact depletions, and thus is expected to depend on solute concentration. Furthermore, we have used MD simulation results to correlate the number of CH contacts with BE aggregate concentrations, and thus obtain experimentally derived BE contact free energy.

The remainder of this manuscript is organized as follows. Section 2 describes the experimental and simulation methods used to obtain the present results. Section 3 quantifies experimentally-derived estimates of BE aggregate concentrations and the corresponding water-mediated contact free energy, as well as compares the experimental results with both MD and RM simulation predictions. The conclusions and the implications of our results are summarized in Section 4.

2. Methods

A. Experimental

Aqueous solutions of BE (ethylene glycol butyl ether $\geq 99.0\%$, Sigma-Aldrich) were prepared by weight using ultrapure water

(Milli-Q UF plus, Millipore), with an electrical resistance of 18.2 M Ω cm. The molar concentrations of BE solutions were determined from density measurements obtained using an Anton Paar DSA 5000 Density and Sound Velocity Analyzer (as described in ESI†). Moreover, we have previously shown that molar concentrations estimated using infinite dilution partial molar volumes are essentially the same as those obtained using density measurements (up to 4 M),³ and thus our concentrations are consistent with a BE partial molar volume of 0.12 M⁻¹ (in a dilute aqueous solution, $0 < [\text{BE}] < 1.1$ M, at 293 K). Duplicate Raman spectra were collected for each sample at 20 °C using an Ar-ion excitation laser ($\lambda = 514.5$ nm) with a power of ~ 15 mW at the sample, and an integration time of 5 minutes per spectrum. Other details pertaining to the home-built Raman spectrometer, and MCR analysis procedures, are the same as those previously reported,¹⁶ unless noted otherwise in Section 3A.

B. Random mixing

Random mixing simulations were performed by generating non-overlapping configurations of solute molecules with random orientations and conformations, and concentrations between 0.25 M and 1.0 M. More specifically, one thousand statistically independent configurations were generated by inserting 10 solute molecules at random positions with random orientations in cubic boxes of volumes ranging from 17 nm³ to 66 nm³, with periodic boundary conditions. For BE, 10 solute conformations were randomly selected from a database of conformations (generated from MD simulations of a single non-rigid solute molecule in water).⁷ Note, however, that over the selected concentration range (0.25–1.0 M), our RM results indicate that the number of solute–solute direct contacts are approximately independent of whether the RM simulations were performed using random conformations or all trans conformations.²⁵ In obtaining the RM configurations, we rejected all configurations that contained any core-overlaps between solute molecules, where a core-overlap is defined as one in which any of the heavy atoms on different molecules were separated by a distance of less than $r_1 = 3.74$ Å, which is consistent with the location of the leading edge in the carbon–carbon radial distribution function $g(r)$ obtained from MD simulations of aqueous solutions of BE⁷ and is approximately the same as the Lennard-Jones diameter of a methyl group (~ 3.73 Å).²⁶

A direct (as opposed to water-separated) hydrophobic contact was defined as a configuration for which any of the CH hydrogen atoms on any methyl or methylene group in a BE molecule is in contact with a CH group on a different BE molecule. Two different upper-bound H \cdots H distance cut-offs of either $r_2 = 2.4$ Å or $r_2 = 3.4$ Å were used to identify a contact. These two cut-off distances were obtained from the first maximum and first minimum in the BE hydrogen–hydrogen radial distribution function. The resulting number of direct hydrophobic contacts between BE molecules was then used to calculate the probability that a given BE has no contacts with any other BE (and thus is classified as a monomer). The RM monomer concentrations were obtained by multiplying each of the latter monomer probabilities by the total BE concentration. The concentration

of aggregated BE molecules (defined as BE molecules that are in contact with at least one other BE) is obtained by subtracting each of the monomer concentrations from the total solute concentration. Note that approximately the same results are obtained when a hydrophobic contact is defined in terms of the carbon-carbon rather than hydrogen-hydrogen separation, with a carbon-carbon contact (upper-bound) distance of 4.9 Å.³

C. Molecular dynamics simulations

In addition to performing new MD simulations (described below), Prof. Gren Patey provided configuration files obtained using large scale MD simulations of aqueous BE performed using CHARMM-AA/TIP3P,⁷ at solute mole fractions below 0.04 (<2 M). We analyzed these configurations to obtain the number of contacts between BE molecules using the same procedure used to identify contacts in the RM simulations (as described above, in Section 2B), and thus obtained MD predictions of the BE monomer and aggregate concentrations.

Additionally, new MD simulations were performed using GROMACS 5.1.2²⁷ to compute potentials of mean force (PMFs) between two BE molecules dissolved in water (as well as in the gas phase), using two different force fields: CHARMM-AA²⁸⁻³¹/TIP3P³² and TraPPE-UA/TIP4P-2005³³ with the HH-alkane model for the alkyl-water interactions.³⁴ Note that the TraPPE-UA/TIP4P-2005 force field is parameterized to accurately predict the phase diagrams of pure alkanes,^{26,35} as well as the solvation thermodynamics of alkanes.³⁴ The ether and hydroxyl groups were represented using TraPPE^{36,37} and their interactions with water were represented using the Lorentz-Berthelot combining rules implemented in GROMACS. See ESI† for further details.

3. Results and discussion

A. Raman-MCR hydration shell spectroscopy

Fig. 1 shows (A) raw Raman spectra and (B) Raman-MCR solute-correlated (SC) spectra obtained from aqueous BE solutions at 20 °C. More specifically, the minimum area SC spectra were obtained using self-modeling curve resolution (SMCR)³⁸ to analyze individual pairs of spectra, one obtained from pure water and the other from a BE solution.³⁸ The resulting SC spectra were each normalized to the BE CH stretch band area, so that the corresponding hydration-shell features pertain to the average hydration-shell of an individual BE molecule at a particular concentration. The resulting hydration-shell OH stretch features, between ~3000 and 3800 cm⁻¹ in Fig. 1B, arise primarily from water molecules whose OH stretch band is perturbed by BE, so it differs from that of bulk water. Previous comparisons of the Raman-MCR spectra of 1,2-hexanediol and 1-hexanol,³⁹ as well as phenol and benzene⁴⁰ have demonstrated that hydroxyl groups on solute molecules do not significantly contribute to Raman-MCR hydration-shell spectra.

Comparisons of Raman-MCR and fs-IR anisotropy measurements of aqueous TBA solutions have confirmed that the hydration-shell OH stretch band areas appearing in CH normalized SC spectra, such as those shown Fig. 1B, are proportional to the

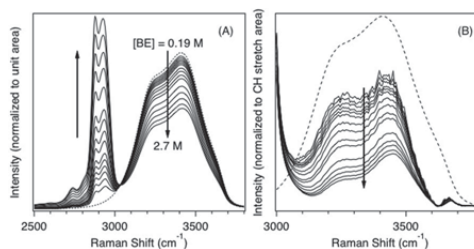


Fig. 1 (A) Raman spectra (normalized to unit area) of pure H₂O (dotted black) and aqueous BE solutions of different concentrations (0.19, 0.29, 0.38, 0.46, 0.55, 0.64, 0.80, 0.94, 1.1, 1.3, 1.6, 1.9, 2.2, 2.4, and 2.7 M). (B) Minimum area SC spectra of BE obtained from the spectra shown in (A), each normalized to the same total CH band area (only the high frequency edge of the CH band is shown in (B)).

average number of perturbed first hydration-shell water molecules around each solute.³ In other words, contacts between solute molecules lead to a reduction in the number of first hydration-shell water molecules, as quantified using the observed decrease in the Raman-MCR SC OH band area. Thus, we infer that the decrease in the hydration shell OH band area in Fig. 1B is proportional to the decrease in the number of perturbed water molecules in the hydration shell of each BE molecule, and that this decrease is proportional to the decrease in the total number of first hydration shell water molecules per BE. Note that the decrease in the number of hydration-shell water molecules must arise from BE aggregation since no such decrease would be expected if all BE molecules retained complete (non-overlapping) hydration-shells.

More specifically, we use the hydration shell depletion percentage $d\%$, defined as follows, to quantify the decrease in the SC (CH normalized) OH integrated band area I , relative to its area I_0 in a dilute (0.2 M BE) solution.

$$d\% = 100 \left(\frac{I - I_0}{I_0} \right) = 100 \left(\frac{n - n_0}{n_0} \right) \quad (1)$$

The second equality follows from our assumption that hydration-shell OH band area is proportional to the corresponding number of water molecules (n) in the first hydration shell of BE in a given solution compared to the number of water molecules (n_0) in the first hydration-shell of a fully hydrated BE molecule.

The solid points in Fig. 2A show how the resulting depletion percentages depend on molar concentration for BE, along with previously published results for methanol and TBA,³ and the open points correspond to MD predictions for aqueous BE (obtained using CHARMM-AA/TIP3P).⁷ Thus, in the dilute limit (*i.e.* ≤ 0.2 M) all of these solutes are essentially fully hydrated (as $d\% \sim 0$). The results in Fig. 2A show how the magnitude of the depletion percentage increases with increasing solute concentration, as well as with solute size. For example, at a solute concentrations of ~1 M, the hydration shell depletion of methanol, TBA, and BE are <2%, ~10%, and ~30%, respectively.

The MD simulation points in Fig. 2A were obtained using eqn (1), where n_0 and n were determined by counting the

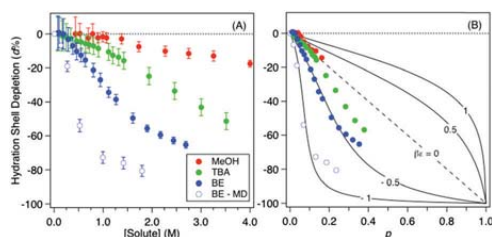


Fig. 2 Raman-MCR hydration shell depletion percentage for aqueous methanol (MeOH, red points), TBA (green points), and BE obtained either experimentally (solid blue points) or from CHARMM-AA/TIP3P MD simulations⁷ (open blue points), plotted as a function of solute molarity (A) or volume fraction ρ (B). The black curves are WRM predictions obtained assuming several different solute–solute contact energies, where $\beta\epsilon = 0$ pertains to an idealized random mixture.

number of water molecules within r_2 of any of the six carbon atoms of BE. The value of r_2 was taken to be equal to either the first ($r_2 = 3.8 \text{ \AA}$) or second ($r_2 = 4.9 \text{ \AA}$) maximum in the corresponding carbon–oxygen radial distribution function, and the error bars on the MD points reflect the range of $d\%$ values obtained when varying r_2 . Note that the MD percent depletion results are relatively insensitive to the precise r_2 cut-off value chosen for analysis, as well as to whether all the carbons or only the four outermost (butyl group) carbons are used to obtain n_0 and n . The magnitudes of the MD $d\%$ values are invariably larger than the experimental $d\%$ values, indicating that the MD simulations predict more aggregation than experimentally observed (as further described in Sections 3B and C).

As a first pass in interpreting the experimental results shown in Fig. 2A we have compared them with depletion predictions obtained using a finite-lattice weighted random mixing (WRM) model,⁴¹ which was used to produce the curves in Fig. 2B. The dashed line represents finite lattice random mixing (FL-RM) predictions and the solid curves represent WRM predictions obtained assuming various assumed values of the BE contact energy ϵ (with $\epsilon < 0$ pertaining to an attractive contact energy, and $\beta\epsilon = \epsilon/RT$, when ϵ is expressed in molar units). Thus, the fact that the methanol points are consistent with the $\beta\epsilon = 0$ predictions implies that methanol contacts are consistent with FL-RM predictions, while TBA contacts only deviate slightly from FL-RM predictions. On the other hand, the experimental and MD simulation results for BE are consistent with larger negative values of $\beta\epsilon$, indicating a more substantial net attractive interaction between BE molecules. Further details regarding how the WRM predictions were obtained are provided in the ESI.† The free energy associated with such contacts may be more accurately estimated as described in Section 3C.

B. Quantification of hydrophobic contacts

In order to obtain a quantitative estimate of the number of monomeric and aggregated solute molecules, a second round of SMCR was used to decompose the SC spectra shown in Fig. 1B into monomer and aggregate components.³ More specifically, the 0.2 M BE CH-normalized SC spectrum in Fig. 1B is attributed to

monomeric BE molecules (with essentially no solute–solute contacts). The latter assignment is supported by our observation that both the normalized SC OH area and the BE CH peak frequency of BE remain approximately constant below 0.2 M (shown in Fig. 2 and the ESI,† respectively). We performed a second round of SMCR to decompose the SC spectra shown in Fig. 1B into a linear combination of two spectra, one of which pertains to the BE monomer, and the other to the minimum area Raman-MCR component arising from contacting (aggregated) BE molecules.

Fig. 3A shows the resulting monomer (blue) and aggregate (red) spectral component spectra. These results indicate that the aggregate spectral component has an OH band area that is depleted by $\sim 65\%$ relative to the monomer spectral component. We attribute this to the local depletion of the hydration-shell in the immediate neighborhood of a contact between CH hydrogen atoms on two different BE molecules. The shaded region in Fig. 3A spans the upper and lower bound estimates of the minimum area aggregate component spectra obtained by performing the second round of SMCR either using SC spectra obtained from BE concentrations below 0.55 M or using all the SC spectra obtained from BE concentrations up to 2.7 M.

The solid points in the inset panel in Fig. 3A represent the fractional contribution (f_{CH}) of the monomer spectral component to each of the spectra shown in Fig. 1B. The monomer fractions were obtained from the ratio of the CH area of the monomer component to the total CH area (as obtained from the second round of SMCR decomposition), and the corresponding error bars indicate the range of results obtained when varying the assumed aggregate spectra from the upper to the lower bounds shown in Fig. 3A. The shaded region in Fig. 3 represent RM

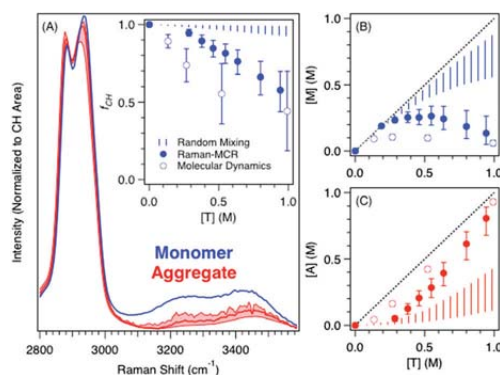


Fig. 3 (A) Monomer (blue) and aggregate (red) component spectra obtained from the second round of SMCR applied to the SC solution spectra in Fig. 1B. (A, inset) Relationship between non-contacting CH fraction f_{CH} and total BE concentration from Raman-MCR experiments (solid points), MD simulations (open points), and RM predictions (dashed regions). (B) Monomer concentrations and (C) aggregate concentrations obtained from Raman-MCR experiments (using the MD correlation between f_{CH} and the f_{M} , shown in Fig. 4), MD simulations, and RM predictions for BE. The black dashed line corresponds to the total solute concentration.

predictions (obtained as described in Section 2B). The results in Fig. 3A indicate that the non-aggregated CH fraction f_{CH} decreases approximately linearly with solute concentration. Furthermore, the MD simulation results for aqueous BE, which were obtained as described in Section 2C, predict that there are slightly fewer non-aggregated CH groups (and thus more aggregation) than obtained using from the Raman-MCR experimental results.

Fig. 3B compares the resulting experimental BE monomer concentration estimates (solid points) with the corresponding MD (open points) and RM (dashed region) predictions. The experimental monomer concentrations were obtained from the non-contacting CH fractions (f_{CH}) shown in Fig. 3A by using the MD results to infer the correlation between CH contacts and monomer concentration (as shown in Fig. 4, and further described below). Note that the latter correlation is expected to be relatively insensitive to variations in the simulation potential functions and the amount of aggregation in the simulations. The fact that the experiments predict fewer monomers (and thus more aggregates) than RM predictions implies that the aggregation potential of mean force has a favorable (attractive) contact free energy (as further discussed and quantified in the next sub-section).

Fig. 4 shows the correlations between the fraction of non-contacting CH groups f_{CH} and the fraction of non-aggregated monomers f_{M} , obtained from the aqueous BE solution MD simulations.⁷ The monomer concentration is obtained by multiplying the monomer fraction by the total concentration of BE, $[\text{monomer}] = [\text{total}]f_{\text{M}} \approx [\text{total}](f_{\text{CH}})^b$. Note that the exponent ($b = 3.54 \pm 0.91$) obtained from the MD simulations implies that there are between 2 and 5 uncorrelated contact domains in BE. In other words, any CH contact within one of these domains is highly correlated with other neighboring CH contacts. Interestingly, the RM simulation correlation (not shown) implies a larger number (~ 9) of uncorrelated domains. The difference between the MD and RM contact correlations presumably arises from the fact that the RM contacts pertain to randomly selected BE orientations and conformations, while the BE contacts in the MD simulations evidently involved pairs of BE molecules whose configurations (*i.e.* orientations and conformations) are correlated with each other, and thus are not

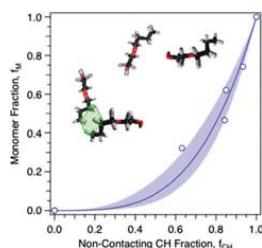


Fig. 4 Correlation between the number of non-aggregated monomer BE molecules and the number of non-contacting CH groups, obtained from MD simulations. The solid curve is a power-law fit. The inset image illustrates the relationship between f_{CH} and f_{M} for a particular configuration of four BE molecules, for which $f_{\text{CH}} = 44/52 = 0.85$ and $f_{\text{M}} = 2/4 = 0.5$.

the same as the RM configurations. In other words, this suggests that equilibrium BE contacts tend to occur between chains with a locally parallel alignment, so that a contact at one CH location is highly correlated with contacts at neighboring CH groups. Whereas, contacts between randomly selected and randomly oriented chains necessarily have no preference for parallel alignment of the contacting chains.

C. Water-mediated interaction energy

The results in Fig. 3, combined with the following procedure, were used to estimate the BE contact free energy (ΔG), in excess of a random mixture. More specifically, the experimentally obtained concentration of aggregated (non-monomeric) BE molecules can be expressed as $[A] = [T] - [M]$, where $[T]$ and $[M]$ are the total and monomer BE concentrations. The corresponding RM prediction for the concentration of aggregated BE molecules is $[A]_{\text{RM}}$. The ratio of the experimental and RM concentrations is used to estimate the free energy difference between the experimental and random contacts.

$$\Delta G \cong -RT \ln \left(\frac{[A]}{[A]_{\text{RM}}} \right) \quad (2)$$

In other words, this free energy reflects the excess probability of observing a contact in the experimental and randomly mixed system. Thus, this ΔG represents an experimental estimate of the minimum value of the potential of mean force associated with bringing two solute molecules into contact with each other.

To compute that latter contact free energy, we performed MD simulations (described in ESI†) to obtain the total $[w(\tau)]$ and direct $[u(\tau)]$ potentials of mean force using two different force fields: CHARMM-AA/TIP3P and TraPPE-UA/TIP4P-2005/HH-alkane.

$$w(\tau) = u(\tau) + \Delta w(\tau) \quad (3)$$

τ represents the distance between the center of mass of the two BE molecules.⁴ The water-mediated contribution $\Delta w(\tau)$ to the mean force potential between BE molecules in water is equivalent to the difference between $w(\tau)$ and $u(\tau)$.

Fig. 5 shows the resulting total, direct, and water-mediated interaction free energies for BE. The total $w(\tau)$ is calculated for two BE molecules in water while the direct interaction energy $u(\tau)$, which is equivalent to the potential of mean force between the two isolated BE molecules, is obtained from simulations containing two isolated (gas phase) EB molecules (representative of the hydrophobic part of BE). In other words, we assume that $w(\tau)$ is not significantly influenced by the hydroxyl group of BE (as the hydroxyl group is likely to be H-bonded to water in both the monomer and aggregate configurations). Thus the direct interaction between two BE molecules is expected to closely resemble the interaction between EB molecules in the gas phase.

The results shown in Fig. 5A and B demonstrate that there is a quite substantial difference between the potentials of mean force minima predictions obtained using the two classical force fields. More specifically, the predicted contact minima in solution (solid black curves) range from $w(\tau) = -3.5 \pm 0.2 \text{ kJ mol}^{-1}$ to $-1.3 \pm 0.3 \text{ kJ mol}^{-1}$, both of which are of the same magnitude as the

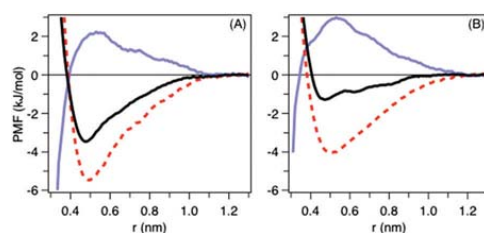


Fig. 5 Total potentials of mean force (solid black) between BE molecules are compared with the corresponding direct (dashed red) and water-mediated (solid blue) contributions calculated using two different force fields: (A) CHARMM-AA/TIP3P and (B) TraPPE/TIP4P-2005 with HH-alkane modifications.³⁴

experimentally obtained contact free energy of $\Delta G \approx -3.0 \pm 0.4$ kJ mol⁻¹ (eqn (2)). Additionally, the predicted contact minima in the gas phase (dashed red curves) range from $u(\tau) = -5.5$ kJ mol⁻¹ to -4.0 kJ mol⁻¹. Moreover, the two simulations agree in predicting a water-mediated contact free energy, of $\Delta w \approx +2.5 \pm 1$ kJ mol⁻¹. This predicted water-mediated contact free energy is remarkably close to the corresponding experimentally derived estimate of $\Delta w = +1.5 \pm 0.6$ kJ mol⁻¹, which was calculated by averaging the difference between the experimental contact free energy ($\Delta G \sim w(\tau)$) and the direct interaction energy obtained from both force fields.

4. Conclusions

We have used Raman-MCR, RM predictions, and MD simulations to quantify both the total and water-mediated free energy associated with bringing two BE molecules into contact with each other in water. Both our experimental results and MD predictions imply that Δw is positive, and thus water drives BE molecules apart, rather than pushing them together. However, the direct interaction energy u between the BE chains is sufficiently large and attractive that the net contact potential of mean force w remains slightly attractive, although less attractive than it would have been in the absence of water, and just barely large enough to effectively compete with thermal energy fluctuations of the order of $RT \sim 2.5$ kJ mol⁻¹.

Our experimentally estimated contact free energies are in reasonable agreement with the contact potentials of mean force obtained from using MD simulations (with two different force fields). However, the large scale aqueous BE simulations performed using the CHARMM-AA/TIP3P force field predict somewhat more BE aggregation than we observe experimentally. The TraPPE/TIP4P-2005 force field, on the other hand, predicts a smaller (less attractive) contact potential of mean force, and thus is expected to produce significantly less BE aggregation. Previous MD simulations of the potentials of mean force between alkanes, as well as fullerenes, dissolved in water predict a size dependent crossover in the sign of the water-mediated interaction free energy, as Δw is predicted to be negative for solutes smaller than neopentane (which has five carbons) and positive for solutes larger than neopentane.²⁰ Our BE results confirm that Δw is positive for BE (which has six carbons). However, previous

Raman-MCR results have implied that Δw is also positive for solutes as small as methanol. It is not yet clear whether experiments are consistent with the MD prediction that Δw becomes increasingly positive with increasing solute size.^{4,5}

Acknowledgements

This work was supported by the National Science Foundation (CHE-1464904). We would like to acknowledge Ryan Svetanoff and Jie Chen for assistance in collecting experimental results, as well as Gren Patey and Rini Gupta for sharing their BE MD simulation configurations and for useful discussions.

Notes and references

- 1 P. Ball, *Chem. Rev.*, 2008, **108**, 74–108.
- 2 W. Kauzmann, in *Adv. Protein Chem.*, ed. C. B. Anfinsen, M. L. Anson, K. Bailey and J. T. Edsall, Academic Press, 1959, vol. 14, pp. 1–63.
- 3 B. M. Rankin, D. Ben-Amotz, S. T. van der Post and H. J. Bakker, *J. Phys. Chem. Lett.*, 2015, **6**, 688–692.
- 4 D. Ben-Amotz, *J. Phys. Chem. Lett.*, 2015, **6**, 1696–1701.
- 5 D. Ben-Amotz, *Annu. Rev. Phys. Chem.*, 2016, **67**, 617–638.
- 6 S. Indra and R. Biswas, *J. Chem. Phys.*, 2015, **142**, 204501.
- 7 R. Gupta and G. N. Patey, *J. Phys. Chem. B*, 2011, **115**, 15323–15331.
- 8 F. Stillinger, *J. Solution Chem.*, 1973, **2**, 141–158.
- 9 D. M. Huang and D. Chandler, *Proc. Natl. Acad. Sci. U. S. A.*, 2000, **97**, 8324–8327.
- 10 D. Chandler, *Nature*, 2005, **437**, 640–647.
- 11 B. J. Berne, J. D. Weeks and R. H. Zhou, *Annu. Rev. Phys. Chem.*, 2009, **60**, 85–103.
- 12 H. S. Ashbaugh and L. R. Pratt, *Rev. Mod. Phys.*, 2006, **78**, 159–178.
- 13 S. Garde and A. J. Patel, *Proc. Natl. Acad. Sci. U. S. A.*, 2011, **108**, 16491–16492.
- 14 C. A. Cerdeirina, P. G. Debenedetti, P. J. Rossky and N. Giovambattista, *J. Phys. Chem. Lett.*, 2011, **2**, 1000–1003.
- 15 N. Huang, D. Schlesinger, D. Nordlund, C. Huang, T. Tyliczszak, T. M. Weiss, Y. Acremann, L. G. M. Pettersson and A. Nilsson, *J. Chem. Phys.*, 2012, **136**, 074507.
- 16 J. G. Davis, K. P. Gierszal, P. Wang and D. Ben-Amotz, *Nature*, 2012, **491**, 582–585.
- 17 I. T. S. Li and G. C. Walker, *Acc. Chem. Res.*, 2012, **45**, 2011–2021.
- 18 I. T. S. Li and G. C. Walker, *Proc. Natl. Acad. Sci. U. S. A.*, 2011, **108**, 16527–16532.
- 19 H. J. Bakker, *Nature*, 2012, **491**, 533–535.
- 20 M. Makowski, C. Czaplowski, A. Liwo and H. A. Scheraga, *J. Phys. Chem. B*, 2010, **114**, 993–1003.
- 21 P. Perera, M. Wyche, Y. Loethen and D. Ben-Amotz, *J. Am. Chem. Soc.*, 2008, **130**, 4576–4579.
- 22 K. R. Fega, D. S. Wilcox and D. Ben-Amotz, *Appl. Spectrosc.*, 2012, **66**, 282–288.
- 23 D. S. Wilcox, B. M. Rankin and D. Ben-Amotz, *Faraday Discuss.*, 2013, **167**, 177–190.

- 24 R. Tauler, A. Smilde and B. Kowalski, *J. Chemom.*, 1995, **9**, 31–58.
- 25 B. M. Rankin, Quantification of Molecular Aggregation Equilibria Using Spectroscopic Measurements and Random Mixing Modeling, PhD thesis, Purdue University, 2015.
- 26 M. G. Martin and J. I. Siepmann, *J. Phys. Chem. B*, 1998, **102**, 2569–2577.
- 27 M. J. Abraham, D. van der Spoel, E. Lindahl, B. Hess and the GROMACS development team, GROMACS User Manual version 5.1.2, 2016, www.gromacs.org.
- 28 I. Vorobyov, V. M. Anisimov, S. Greene, R. M. Venable, A. Moser, R. W. Pastor and A. D. MacKerell, *J. Chem. Theory Comput.*, 2007, **3**, 1120–1133.
- 29 K. Vanommeslaeghe, E. Hatcher, C. Acharya, S. Kundu, S. Zhong, J. Shim, E. Darian, O. Guvench, P. Lopes, I. Vorobyov and A. D. Mackerell, *J. Comput. Chem.*, 2010, **31**, 671–690.
- 30 W. Yu, X. He, K. Vanommeslaeghe and A. D. MacKerell, *J. Comput. Chem.*, 2012, **33**, 2451–2468.
- 31 V. Zoete, M. A. Cuendet, A. Grosdidier and O. Michielin, *J. Comput. Chem.*, 2011, **32**, 2359–2368.
- 32 W. L. Jorgensen, J. Chandrasekhar, J. D. Madura, R. W. Impey and M. L. Klein, *J. Chem. Phys.*, 1983, **79**, 926–935.
- 33 J. L. Abascal and C. Vega, *J. Chem. Phys.*, 2005, **123**, 234505.
- 34 H. S. Ashbaugh, L. Liu and L. N. Surampudi, *J. Chem. Phys.*, 2011, **135**, 054510.
- 35 M. G. Martin and J. I. Siepmann, *J. Phys. Chem. B*, 1999, **103**, 4508–4517.
- 36 B. Chen, J. J. Potoff and J. I. Siepmann, *J. Phys. Chem. B*, 2001, **105**, 3093–3104.
- 37 J. M. Stubbs, J. J. Potoff and J. I. Siepmann, *J. Phys. Chem. B*, 2004, **108**, 17596–17605.
- 38 W. H. Lawton and E. A. Sylvestre, *Technometrics*, 1971, **13**, 617–633.
- 39 J. G. Davis, Spectroscopic investigations of water-mediated interactions, PhD thesis, Purdue University, 2012.
- 40 K. P. Gierszal, J. G. Davis, M. D. Hands, D. S. Wilcox, L. V. Slipchenko and D. Ben-Amotz, *J. Phys. Chem. Lett.*, 2011, **2**, 2930–2933.
- 41 D. Ben-Amotz, B. M. Rankin and B. Widom, *J. Phys. Chem. B*, 2014, **118**, 7878–7885.